

# **Fabrication-Tolerant Integrable InGaAsP C-Band Polarization Rotator**

by

Vishal Shah  
Bachelor of Engineering  
Electronics and Communication Engineering

A thesis submitted to the  
Faculty of Graduate and Postdoctoral Affairs  
in partial fulfillment of the requirements for the degree of

Master of Applied Science  
in  
Electrical and Computer Engineering

Carleton University  
Ottawa, Ontario

© 2022  
Vishal Shah

## **Abstract**

Modern communications have reached unpredicted bit rates due to rapid and accelerating research carried out in the field of Photonics. A design and simulation of a polarization rotator using III-V materials (InP/InGaAsP) with a feasible fabrication process were performed. The polarization conversion efficiency of ~98% and polarization extinction ratio of ~17.3dB over 1530nm to 1570nm wavelength (C-band) was achieved. The study was used to select the etch stop layer, visualize the state of polarization at different lengths of the device, and predict the variability of the polarization rotator over different lengths. The selected device structure provides a significant fabrication tolerance enhancement factor which consists of a one-sided tapered ridge waveguide and a deeper-etch structure on the opposite side. This work offers a practical path toward the integration of a polarization rotator in a photonic integrated chip and would pave a way for future innovation.

## Acknowledgements

First and foremost, I would like to praise and thank the Almighty, who has granted me countless blessings, knowledge, and opportunity to be able to accomplish this thesis.

I would like to express my greatest appreciation to my supervisor Dr. Steven P. McGarry who made this thesis work possible. The completion of this study would not have been possible without his guidance and advice. His expertise, patience, motivation, and enthusiasm carried me through all the stages of this thesis work.

I am extremely grateful to Carleton University and the entire Department of Electronics, who provided me a chance to be able to reach this point in my academic career. My sincere thanks to Dr. Winnie Ye who agreed in providing me with the license for Ansys Lumerical simulation software. A debt of gratitude is also owed to Mr. Nagui Mikhail, the departmental administrator, Ms. Blazenka Power, and Ms. Valerie Daley for their tremendous support throughout the journey.

A special thanks to a very good friend, Dr. Ramon Maldonado-Basilio for continuous encouragement and guidance throughout this degree. I would also like to extend my sincere thanks to Mr. Harry Walters who impelled me to achieve this milestone.

My warmest thanks to my dearest, Moonisah Shaik, I could not have completed this thesis work without your support. You provided stimulating discussions as well as happy distractions to rest my mind outside of my research during a very harsh covid-19 phase. I am very much grateful for your unmatched support. I would like to thank my friend, Mutayyab Ahmed for believing in the efforts I committed for the completion of this study. Finally, I would like to thank my parents and my family members who braced me from the far end of the world-India to accomplish this thesis work.

## Table of Contents

<b>Abstract.....</b>	<b>ii</b>
<b>Acknowledgements .....</b>	<b>iii</b>
<b>List of Tables .....</b>	<b>viii</b>
<b>List of Figures.....</b>	<b>ix</b>
<b>Nomenclature .....</b>	<b>xiii</b>
<b>Chapter 1 Introduction .....</b>	<b>1</b>
<i>1.1 Optical communication .....</i>	<i>1</i>
<i>1.2 Photonics .....</i>	<i>3</i>
1.2.1 Silicon photonics.....	4
1.2.2 III-V compound semiconductor.....	5
<i>1.3 Motivation for integrated polarization rotator .....</i>	<i>6</i>
<i>1.4 Thesis objective .....</i>	<i>8</i>
<i>1.5 Statement of contribution .....</i>	<i>9</i>
<i>1.6 Thesis outline.....</i>	<i>10</i>
<b>Chapter 2 Theory of optical waveguides .....</b>	<b>11</b>

<i>2.1 Introduction to optical waveguides .....</i>	11
<i>2.2 Maxwell's equations.....</i>	12
2.2.1 Maxwell's first equation (Gauss's law) .....	13
2.2.2 Maxwell's second equation (Gauss law for magnetic field) .....	13
2.2.3 Maxwell's third equation (Faraday's law).....	13
2.2.4 Maxwell's fourth equation (Ampere's law).....	14
2.2.5 Wave equation.....	14
<i>2.3 Waveguide structures .....</i>	16
<i>2.4 Waveguide modes .....</i>	16
<i>2.5 Polarization .....</i>	17
2.5.1 Transverse Electric (TE) mode .....	17
2.5.2 Transverse Magnetic (TM) mode .....	17
2.5.3 Poynting vector .....	19
2.5.4 Birefringence.....	19
2.5.5 The illustration of waveguide modes .....	21
<i>2.6 Figures of merit .....</i>	24
2.6.1 Polarization extinction ratio (PER).....	24
2.6.2 Insertion loss ( <i>IL</i> ).....	25
2.6.3 Polarization-dependent loss ( <i>PDL</i> ).....	25

2.6.4 Coupling loss ( <i>CL</i> ) .....	25
<b>Chapter 3 State of the art.....</b>	<b>26</b>
<i>3.1 Poincare sphere.....</i>	26
<i>3.2 Polarization rotator.....</i>	28
3.2.1 Crystal based polarization rotator .....	28
3.2.2 The optical fiber-based polarization rotator .....	30
3.2.3 On-chip polarization rotator.....	31
3.2.4 Passive polarization rotator.....	33
<i>3.3 Conceptual preference .....</i>	38
<b>Chapter 4 Design and Simulation .....</b>	<b>41</b>
<i>4.1 Approach .....</i>	41
<i>4.2 Design of the Polarization Rotator .....</i>	42
4.2.1 Design principle .....	43
4.2.2 Design parameters.....	45
4.2.3 Introduction to Finite Difference Time Domain (FDTD) 3D Solver .	47
4.2.4 Structure geometry setup .....	51
4.2.5 The FDTD solver region and mesh settings .....	53
4.2.6 Input mode source and monitors setup .....	54

<b>Chapter 5 Results and Discussion .....</b>	<b>57</b>
<i>5.1 The analysis of the etch-stop layer (<math>R_{etch}</math>) .....</i>	<i>57</i>
<i>5.2 Polarization conversion efficiency (PCE).....</i>	<i>59</i>
5.2.1 Analyzing polarization conversion efficiency using a 3D-FDTD solver.....	59
5.2.2 Cross testing the results obtained using the EME solver.....	62
5.2.3 The State of polarization along the device length .....	66
5.2.4 Variational study of polarization rotator over the length .....	71
5.2.5 The Polarization extinction ratio (PER) .....	72
<b>Chapter 6 Fabrication Overview.....</b>	<b>75</b>
<i>6.1 Overview of the fabrication process.....</i>	<i>76</i>
<b>Chapter 7 Conclusions and Future work .....</b>	<b>79</b>
<i>7.1 Conclusions .....</i>	<i>79</i>
<i>7.2 Future work .....</i>	<i>82</i>
<b>References .....</b>	<b>83</b>

## List of Tables

Table 3.1 State of art-literature review .....	37
Table 4.1 The definition of the parameters .....	47
Table 5.1 Etch-stop layer as InP .....	58
Table 5.2 Etch-stop layer as InAlAs .....	58
Table 5.3 The study for analyzing Polarization Conversion Efficiency (PCE) against Polarization Converter ridge width ( $w_1, w_2$ ) and Polarization Converter Length ( $L$ ) .....	59
Table 5.4 The user S-parameter matrix .....	64
Table 5.5 The Polarization Extinction Ratio for wavelength 1550nm-1600nm .....	73

## List of Figures

Figure 1.1 The linear absorption in Si using Fourier transform infrared spectroscopy [13].....	4
Figure 1.2 The absorption spectrum of III-V semiconductor [18] .....	5
Figure 2.1 The refractive index profile of basic slab optical waveguide [21].....	12
Figure 2.2 Different structures of waveguide [23] .....	16
Figure 2.3 Fundamental TE mode of a rib-waveguide using Lumerical MODE solver.....	18
Figure 2.4 Fundamental TM mode of a rib-waveguide using Lumerical MODE solver.....	18
Figure 2.5 The structure of a ridge waveguide [ $W$ =width, $H$ =height] .....	21
Figure 2.6 The mode profiles of $TE_0$ , $TE_1$ , $TE_2$ , $TM_0$ , $TM_1$ , $TM_2$ of a ridge waveguide structure .....	22
Figure 2.7 The Lumerical analysis of two waveguides in proximity – light coupling. ....	23
Figure 3.1 The Polarization Ellipse [27].....	26
Figure 3.2 Poincare sphere elaborating the polarization states-[RCP – Right Circular Polarization, LCP – Left Circular polarization, LVP – Linear Vertical Polarization, LHP – Linear Horizontal Polarization, (L -45)-	

Right Elliptical Polarization, and (L +45)- Left Elliptical Polarization] [28].....	27
Figure 3.3 The bending of a crystal-based polarization rotator before the width is bent [29].....	29
Figure 3.4 The bending of a crystal-based polarization rotator after the width is bent [29].....	29
Figure 3.5 The block diagram of the polarization rotation system [29]. .....	29
Figure 3.6 The different crystal twisting angles of the polarization rotator [29]. ...	30
Figure 3.7 Linear correlation between the crystal twisting and polarization rotation angle [29]. .....	30
Figure 3.8 Polarization controlled fiber by squeezing fiber and angled waveplates [28].....	31
Figure 3.9 The electrically tunable polarization rotator [32].....	32
Figure 3.10 The Nematic Liquid Crystal (NLC) molecule's orientation at different bias states [32] .....	32
Figure 3.11 The mode evolution-based polarization rotator-splitter design via a simple fabrication process [36].....	34
Figure 3.12 The polarization rotator based on the mode coupling principle [37] ...	35
Figure 3.13 Polarization rotator based on mode hybridization [38] .....	36

Figure 4.1 The schematic of the designed polarization rotator using InP/InGaAsP	43
.....	.....
Figure 4.2 The cross-section view of the deeper-etch ridge waveguide .....	45
Figure 4.3 The detailed annotation of the polarization rotator .....	46
Figure 4.4 The Lumerical-FDTD solver window.....	48
Figure 4.5 The Rib waveguide structure for mesh and simulation region convergence test.....	49
Figure 4.6 Example of the performed Mesh region convergence test.....	50
Figure 4.7 Extracting sweep parameters for different ridge widths .....	50
Figure 4.8 Structure group of the designed polarization rotator.....	51
Figure 4.9 The illustration of geometry window for a structure layer .....	52
Figure 4.10 The FDTD solver region and Mesh region setup.....	53
Figure 4.11 Optical sources in 3D-FDTD solver.....	54
Figure 4.12 The monitors for recording the simulation data .....	55
Figure 4.13 Placement of the 78 monitors to obtain accurate data points .....	55
Figure 5.1 Influence of InP etch-stop .....	58
Figure 5.2 Influence of InAlAs etch-stop .....	58
Figure 5.3 The study for analyzing Polarization Conversion Efficiency (PCE) against polarization converter ridge width ( $w_1, w_2$ ) and polarization converter length ( $L$ ) .....	60

Figure 5.4 The EME solver setup window .....	62
Figure 5.5 Input and output ports setup .....	63
Figure 5.6 The electric field profile of the TE mode of the input ridge waveguide	63
Figure 5.7 The S-parameter matrix index mapping from the EME solver.....	64
Figure 5.8 The block diagram explaining the S-parameter matrix.....	64
Figure 5.9 The S-parameter matrix for polarization conversion efficiency from $TE_0$ to $TM_0$ .....	65
Figure 5.10 The S-parameter matrix for $TM_0$ to $TE_0$ .....	66
Figure 5.11 The polarization state of mode throughout the entire device length....	67
Figure 5.12 The polarization state of mode throughout the entire device length....	69
Figure 5.12 The electric field intensity profile of the polarization rotator- 2D Z- normal view .....	70
Figure 5.13 The Propagation EME Sweep versus Polarization Converter Length .	71
Figure 5.14 The Wavelength Dependency versus Polarization Conversion Efficiency for the entire C-band (1530nm to 1570nm) .....	73
Figure 6.1 The block diagram for the fabrication process.....	76

## Nomenclature

<b>Abbreviations</b>	<b>Full-Form</b>
<i>2D</i>	Two Dimensional
<i>3D</i>	Three Dimensional
<i>BIF</i>	Bend Insensitive Fiber
<i>C-band</i>	Conventional band
<i>CL</i>	Coupling Loss
<i>CSF</i>	Cut-Off Shifted Fiber
<i>DWDM</i>	Dense Wavelength Division Multiplexing
<i>EDFA</i>	Erbium-Doped Fiber Amplifier
<i>EME</i>	Eigen Mode Expansion
<i>ER</i>	Extinction Ratio
<i>FDE</i>	Finite Difference Eigenmode
<i>FDTD</i>	Finite Difference Time Domain
<i>FEEM</i>	Finite Element Eigenmode
<i>GaAs</i>	Gallium Arsenide
<i>GaN</i>	Gallium Nitride
<i>IL</i>	Insertion Loss
<i>InAlAs</i>	Indium Aluminum Arsenide
<i>InAs</i>	Indium Arsenide
<i>InGaAsP</i>	Indium Gallium Arsenide Phosphide
<i>InP</i>	Indium Phosphide

<i>InSb</i>	Indium Antimonide
<i>LED</i>	Light Emitting Diode
<i>MMF</i>	Multi-Mode Fiber
<i>MZI</i>	Mach-Zender Interferometer
<i>PBF</i>	Photonic Bandgap Fiber
<i>PCE</i>	Polarization Conversion Efficiency
<i>PDL</i>	Polarization Dependent Loss
<i>PER</i>	Polarization Extinction Ratio
<i>PIC</i>	Photonic Integrated Circuit
<i>PIN</i>	Positive Intrinsic Negative
<i>PR</i>	Polarization Rotator
<i>SiO<sub>2</sub></i>	Silicon Dioxide
<i>SOA</i>	Semiconductor Optical Amplifier
<i>SOI</i>	Silicon-On-Insulator
<i>SRH</i>	Shockley-Read Hall
<i>TE</i>	Transverse Electric
<i>TEM</i>	Transverse Electro-Magnetic
<i>TM</i>	Transverse Magnetic

# **Chapter 1 Introduction**

## **1.1 Optical communication**

The internet, with its innumerable applications, flourishing users, and an army of services is the fuel for today's modern communication and information society. A key development of modern civilization is said to be a product of research and development in the field of optical communication. Statistical research shows that an estimated 64.2 percent of the world population was connected to the internet in 2020 which shows incredible growth when compared to 2005 with only 15.7 percent [1] and the numbers are assumed to only grow higher.

The Covid-19 pandemic has brought a revolution regarding e-commerce platforms to shop online and has put e-commerce at the forefront of the retail industry. The approximated growth for online shopping was in slow gradual increase with a pace of only 4.5 percent a year globally before the hit of the major covid-19 outbreak. The implied impact of the pandemic also resulted in an imposed +15 percent peak traffic increase on global submarine network peak traffic usage [2]. The increase in the adaption of digital platforms also enlarged the consumption of communication channels and most internet services. The business that adapts to the changes with the digital platform will survive and thrive even during the harsh time of total lockdowns [3].

The increase in the traffic and the demand for faster communication speed and larger bandwidth by industry rulers like Amazon, Google, Facebook, Netflix, Alibaba, Shopify, Twitter, etc. have dramatically increased. Huge data is processed per minute and the statistical report from a leading market survey industry partner says, about 30+ billion sessions and 150+ billion page views have been noted by many big market leaders mentioned above [4]. So how do we manage

these huge demands in the current phase of modern communication growth? The answer is Photonics-the optical fiber-based global network.

Regardless of the depth of penetration, only a few people are aware that fiber optic communication is the backbone of modern communication architecture. Indeed, the Internet would not have been able to expand to the extent that it has without the use of extremely cost-effective and energy-efficient fiber-optic communication and switching technologies [5]. The reason behind using the optical fiber over traditional copper wires is because of its characteristics to serve the user like greater bandwidth, reliability of information transmission, security of data processing, minimal attenuation, durability, cost, and adaptability [6].

Optical fiber installations worldwide have surpassed four billion kilometers, implying that the resulting fibers could be wrapped around the globe one hundred thousand times. More than three exabits (one exabit =  $10^{18}$  bits) of traffic per second is transported through these fibers using infrared light between users, data centers, and computers, increasing user traffic [7]. Hardware developments on the network system levels such as Erbium-doped fiber amplifiers (EDFAs), Semiconductor Optical amplifiers (SOA), Dense wavelength division multiplexing (DWDM), Space-Division Multiplexing (SDM), Emerging fibers such as Single-mode, Bend-Insensitive Fibre (BIF), Cut-off-Shifted Fibre (CSF), Dispersion shifted fiber (DSF), Multi-mode fiber (MMF), Photonic bandgap fiber (PBF), Dual polarisation data transmission techniques, etc., [8]. With the help of those hardware developments, the maximum transmission distance that was limited to a hundred kms between two fiber-optic transponders has been increased to several thousand km, and even transoceanic links exceeding 10,000 km [9]. The Submarine network now carries over 99 percent of the world's intercontinental electronic communication traffic [9].

The continuous growth of research has evolved the field of photonics where each bit of communication data traffic must once pass through the fiber optics. How can our contemporary society evolve without the advancement of internet humming? It can easily be stated that electronics dominated the 20<sup>th</sup> century and photonics will begin to dominate the 21<sup>st</sup> century [10].

## 1.2 Photonics

Photonics is the field of science that studies the characteristics of light. The generation, emission, transmission, modulation, signal processing, switching, amplification, detection, and sensing of light are the aspects of photonics. There are different materials involved in the process of fabrication of devices using light as a medium of communication. The devices such as Lasers, SOA, Photonic Modulators, Photonic Integrated Circuits, Photonic Crystals, Photonic Components such as Ring Resonators, LED, Polarization Splitters, Polarization Rotators (PR), Directional Couplers, Sensors, and many more are designed by selecting an optical medium with appropriate material characteristics to obtain the optimum output. These materials are semiconductor materials. There are two kinds of semiconductor materials, one with direct bandgap, where the minimal-energy state in the conduction band and the maximum-energy state in the valence band are each characterized by a certain crystal momentum called as k-vector, if the k-vector is the same the electron can easily emit a photon. The second is indirect bandgap material, where the k-vector is different, and an electron cannot easily emit a photon as it must transit through an intermediate energy state to emit a photon by any recombination type such as Shockley-Read-Hall (SRH), Auger recombination, Radiative recombination [11]. The Si and (III-V) semiconductor material is the major used for the fabrication of photonic devices.

### 1.2.1 Silicon photonics

The study and application using silicon as an optical medium is called silicon photonics. The silicon semiconductor is an indirect bandgap material. Silicon has the lowest cost per unit area and is the best understood of all crystalline semiconductors. When used for waveguides, silicon offers strong optical confinement with high refractive index contrast between Si ( $n = 3.5$ ) and  $\text{SiO}_2$  ( $n = 1.45$ ). This helps in fabricating and scaling many optical components at the hundreds of nanometer level. Optical non-linear observations are possible due to the same index contrast between Si and  $\text{SiO}_2$ . The Raman effect and Kerr effects are the illustrations of this. Due to this, there has been much research done in the past decade including the demonstration of lasing, amplification, and wavelength conversion [12].

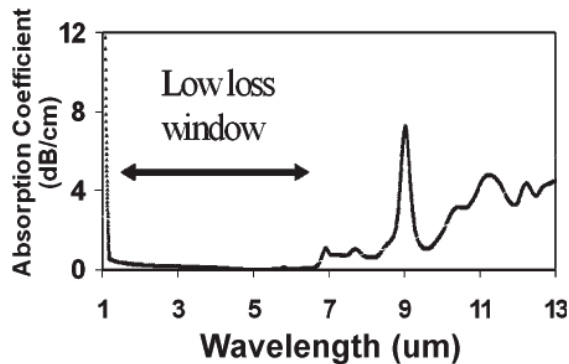


Figure 1.1 The linear absorption in Si using Fourier transform infrared spectroscopy [13]

The integration maturity level of silicon is higher and is fully adaptable to photonics circuits and CMOS technology [13] [14]. As shown in Figure 1.1 the low-loss transparent wavelength window extends from  $1.1 \mu\text{m}$  to  $\sim 7 \mu\text{m}$  and that proves to be excellent for Mid-IR spectrum and C-band wavelengths [13]. The low propagation losses in silicon material allow many passive devices to be grown on SOI-based wafers and are easily available. Many giant market leaders like Intel, IBM, CISCO, Ericson, TeraXion, and Ciena are highly invested in silicon photonics as the

electro-optic solution for their network architecture. The SOI platform facilitates a complete portfolio of photonic components like filters, (de)-multiplexers, rotators, splitters, modulators, Mach-Zender interferometric (MZI), ring-based modulators, and photodetectors with important applications in telecommunication and interconnects [14] [15]

### 1.2.2 III-V compound semiconductor

Group III-V semiconductor such as InP, InAs, GaAs, GaN, and InSb has demonstrated the ability to combine with the most reliable integration of active and passive both optoelectronic components operating at  $1.3\text{ }\mu\text{m}$  to  $1.7\text{ }\mu\text{m}$  telecom window. The properties such as direct bandgap, low exciton binding energy, and reliable optical characteristics have now a wide application range in high-performance optical devices [16] [17].

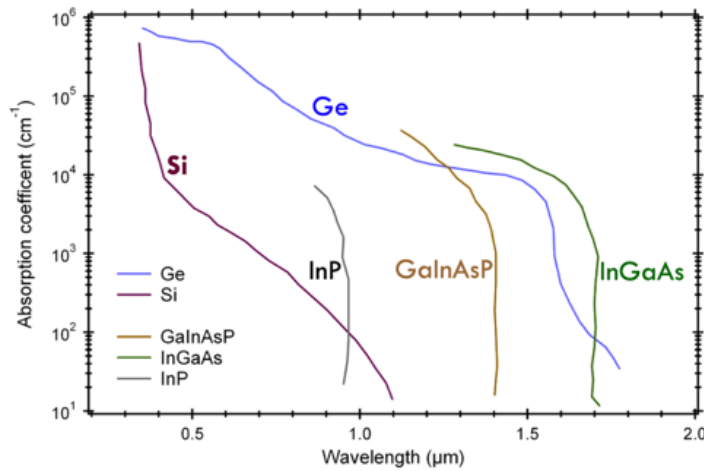


Figure 1.2 The absorption spectrum of III-V semiconductor [18]

The III-V semiconductor can integrate many different optical elements into a single device at sub-micro level fabrication. Using the combination of the III-V compound semiconductors high power efficiency, smaller system size, and high complexity integration can be achieved. Looking at the recent research and development carried out on these semiconductors, many different

achievements are seen, for example, uniformity in wafer production and reproducibility of the fabrication process. Manufacturing processes such as epitaxy, lithography, and etching can also be carried with remarkable tolerances [17].

A recent example is the direct integration of III-V materials on silicon was published by Imec and Ghent University in Belgium [19]. The advancement of the flip-chip technology is a key to integrating SiP and III-V material [20]. Therefore, the integration of different optical components into smaller packages and eliminating the use of bulk optics at the package level irrespective of the material platform is a key component to deriving the most powerful photonic technologies such as approaching 5G data communication speed.

### **1.3 Motivation for integrated polarization rotator**

The research and the push towards having optical modulators fabricated in III-V semiconductors are evident from big manufacturers like Infinera, Cisco, Acacia, Nokia, Ciena, Huawei, and others. But at some point, they integrate with silicon photonics to process the transmitted modulated signal into dual polarizations. These companies are heavily invested in terms of research related to integrating small components for cost-saving at the assembly level. As in the current phase of photonic integration, there can be both hybrid and monolithic integration. In hybrid integration, there can be multiple single-function optical components such as MMI, couplers, bulk optics such as splitter, and polarization rotator which can be assembled into a single package to achieve the desired outcome of any PIC at the packaging level. Moreover, the assembly process at this packaging level is highly complex. The tolerance specification needed for this kind of integration is constricted at the sub-micron level. The final output of this package is solely dependent on every individual component placed. The cumulative result of optical alignment of many discrete optical components placed using different die attach techniques and tools can result

in a high failure rate due to minor misalignments. Adding to the fact is that the different materials of multiple discrete optical components may require different mechanical and thermal requirements. For example, if two optical components are fabricated from two different materials having a different thermal coefficient of expansion, there may be many alignments related issues due to their variation in operating temperature characteristics. They may then require individual heaters or coolers depending on the nature of the errors. This also adds to the cost, complexity, and space budget at the packaging level. There are many photonic industry rivals (combination of III-V semiconductor and SiP) who still use the bulk optics with their photonic integrated modulator packages to create a 90-degree polarization rotation at the output to achieve data transmission of both TE and TM components.

On the other hand, the monolithic integration can accommodate many different optical components into one single wafer with identical semiconductor material. This integration will help in reducing the errors related to optical misalignment, the complexity of the packaging, testing-analyzing, burn-in, power efficiency, and manufacturing cost. During the fabrication of the wafers, a secondary component such as a ring resonator, polarization splitter, polarization rotator, and directional couplers can be added to the same material growth layout as per the requirement of the photonic circuit operation. During this integration, either of the primary components is prioritized during the wafer growth, and later in the process, the etching is done to integrate the secondary component growth on the same wafer. The final wafer when released then has a composite block consisting of the primary and secondary components together.

From the recent research and the motivation to integrate the miniature optical components in the same material platform, here we have proposed an approach towards a practical path by designing and simulation a fabrication-tolerant integration permitting polarization rotator based on

III-V compound semiconductor material over C-band. This will allow the flexibility to remove the optical rotator bulk optics used at the package level if the optical rotation is required after the single polarization modulated signal is transmitted from the output of the optical modulator. Many studies have been carried out previously where the proposed design of the polarization rotator is not fabrication friendly. This is due to their complex design, low fabrication yield, extreme tolerant sensitivity, optical component size, theoretical assumptions, and neglecting the real fabrication limitations. There is also limited study about the risk of integration with the primary optical components. The goal of this research study is to simulate the polarization rotator using an III-V semiconductor stack and derive the results by referencing the real fabrication limitations which are published and available. The results and the conclusion of this detailed study illustrate the viability of the integration of the polarization rotator with the optical modulator to transmit the data in both TE and TM components as per the polarization-dependent specification.

## **1.4 Thesis objective**

Primary objective: The Simulation Study of Fabrication-Tolerant Integrable InGaAsP C-Band Polarization Rotator. The intents are briefly discussed below.

- Simulate a fabrication robust polarization rotator using III-V semiconductor material.
- Determine the effect of different variations in geometry.
- Selection of the etch-stop layer.
- The study to observe the Polarization Conversion Efficiency (PCE) of the device over the C-band (1530nm-1570nm).
- Achieve high Polarization Extinction Ratio (PER) of the proposed polarization rotator.
- The assessment of high-level processes for future fabrication of the device.

## **1.5 Statement of contribution**

In the first stage, the literature review was conducted on the existing research and development state of art for polarization rotators in Si and InGaAsP material systems. Many designs have been found promising but did not meet the requirement of acceptable fabrication tolerance. This sensitivity to fabrication error hinders the possibility of the device being integrated with different optical components.

Interest in the III-V quaternary material system was mainly due to its valuable semiconductor and optoelectronic properties. The weak vertical confinement in InP/InGaAsP compound semiconductor was although a challenge due to the loss of refractive index contrast. For better optical confinement in the core, we have selected a thick InP cladding layer that may broaden the scope of integrating the studied design with other PIC elements such as SOA, MZ, etc.

The focus of this study was on achieving robust design against fabrication errors, compact, and integration permitting design. The primary contribution of this work is:

- The polarization conversion efficiency of the design was studied with different combinations of dimensions (i.e., length and width).
- Two different etch-stop materials were studied and simulated to maintain core thickness as precisely as possible during the future fabrication process.
- A variational study of the polarization rotator over the length (0  $\mu\text{m}$  to 1600  $\mu\text{m}$ ) was conducted on a simulation platform.
- The wavelength dependency of the polarization converter for the C-band (1530-1570nm) was studied.
- The polarization state (field profile) of mode conversion throughout the entire device length was extracted.

- Polarization conversion efficiency achieved was in the range of ~42% to ~98% for different dimensions of the device. We have cross-related the obtained results with another simulation solver tool.
- The simulation study to obtain the Polarization Extinction Ratio (PER) was performed and it ranges from ~13dB to ~17dB over C-band.
- The main advantages of this design over competing designs are:
  - a. Compact and simple design with no bi-level taper or slope structure.
  - b. Robust to variation in width and core geometry during fabrication.
  - c. Integrable design because of a widely used material stack and ridge waveguide structure.

## **1.6 Thesis outline**

The outline of the thesis is as follows: Chapter 1 highlights the background, material, motivation, and objective. Chapter 2 mainly focuses on the theory of optical waveguides. Chapter 3 describes the research study performed on the designs proposed and the experiments carried out by other researchers in past. Chapter 4 considers the proposed design of the polarization rotator, and simulation setup and justifies the direction of the approach. Chapter 5 focuses on simulation and results. Chapter 6 explains the high-level block diagram for the future fabrication of the polarization rotator. Chapter 7 contains a broad discussion of the fabrication-tolerant polarization rotator, its optimization, and future work on the proposed design. Finally, the thesis is concluded with the ending remark and references used for the study.

## Chapter 2 Theory of optical waveguides

To understand the working principle of the polarization rotator it is important to investigate some basic concepts of the waveguides and the perception behind the propagation of electromagnetic waves. Therefore, the elementary concept of the light that propagates through optical waveguides is explained in this chapter. The types of waveguide structures, light confinement, mode formation, understanding of TE and TM polarization and its importance, remarks on III-V compound semiconductor index contrast, Maxwell's equation, boundary conditions, and the pointing vector are some of the key points that are discussed briefly.

### 2.1 Introduction to optical waveguides

A waveguide is a structure or a medium for the light waves to travel from one point to another in which the transmission energy is limited to a single direction with very minimum distortion. These light waves can propagate only if the structure of the medium is larger than the lowest frequency propagating through it. There are many types of waveguide structures which are discussed later in the coming chapters.

The waveguides consist of the substrate ( $n_2$ ), core ( $n_1$ ), and cladding ( $n_0$ ). The material of these layers has a high refractive index ratio due to which the light only propagates through the core of the waveguide. The refractive index depends on the type of semiconductor material. The light waves traveling through a waveguide must obey a certain path for their propagation. If the refractive index of the core ( $n_1$ ) is higher than the refractive index of the cladding ( $n_0$ ) then the light gets confined in the core ( $n_1$ ) due to the phenomenon called total internal reflection (TIR). The condition for the TIR at the core-cladding interface is given below [21].

$$n_1 \sin(\pi/2 - \phi) \geq n_0 \quad (2.1)$$

The refractive index profile structure of the basic optical waveguide is shown in the figure below:

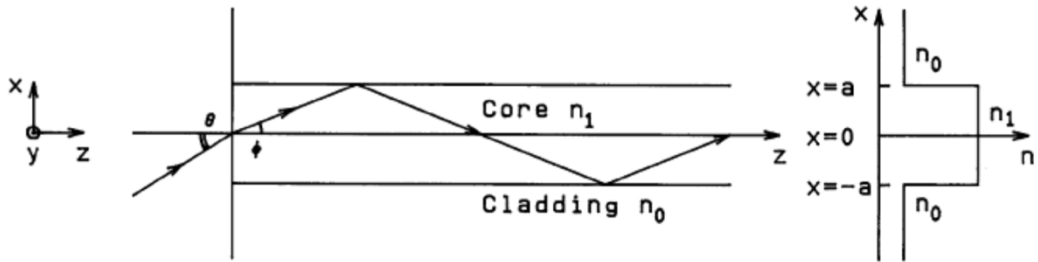


Figure 2.1 The refractive index profile of basic slab optical waveguide [21]

Any light that travels through an optical medium must obey a certain path which is derived using Maxwell's equation.

## 2.2 Maxwell's equations

A wave is an oscillation accompanied by a transfer of energy that travels through a medium. Waves transfer both energy and momentum. Electromagnetic (EM) radiation is the radiant energy released by varying EM fields in the form of EM waves. James Clerk Maxwell discovered that he could combine four simple equations, which had been previously discovered, along with a slight modification to describe self-propagating waves of oscillating electric and magnetic fields. These equations are a set of partial differential equations that form the foundation of classical electrodynamics. The modifications in the previously discovered equations (Gauss's law, Gauss's law of magnetism, Faraday's law of induction, Ampere's circuital law) [21] made the starting point for advanced courses in understanding the study of the electric and magnetic phenomenon of an electromagnetic wave (EM wave). Maxwell's equations represent one of the most elegant and concise ways to state the fundamentals of electricity and magnetism. Maxwell's equations explain

the connections between the electric field E (V/m), magnetic field H (A/m), charge density  $\rho$  (C/m<sup>3</sup>), and the current density J (A/cm<sup>2</sup>).

### 2.2.1 Maxwell's first equation (Gauss's law)

The net electric flux through any closed surface is equal to  $\frac{1}{\epsilon_m}$  times the charge density within the closed surface.

$$\nabla \cdot E = \frac{\rho}{\epsilon_m}, \quad (2.2)$$

Where,  $\epsilon_m$  is the permittivity of the medium, and the  $\nabla$  is given by

$$\nabla = \left( \frac{\partial i}{\partial x}, \frac{\partial j}{\partial y}, \frac{\partial k}{\partial z} \right) \quad (2.3)$$

Where,  $i, j$ , and  $k$  are the unit vectors in the  $x, y$  and  $z$  directions respectively.

### 2.2.2 Maxwell's second equation (Gauss law for magnetic field)

The net magnetic flux through a closed surface is always zero, which is the statement of the absence of the free magnetic monopoles.

$$\nabla \cdot H = 0 \quad (2.4)$$

### 2.2.3 Maxwell's third equation (Faraday's law)

The induced electric field around a closed path is equal to the negative of the time rate of change of magnetic flux enclosed by the path.

$$\nabla \times E = -\mu_m \frac{\partial H}{\partial t} \quad (2.5)$$

Where,  $\mu_m$  is the magnetic permeability of the medium.

## 2.2.4 Maxwell's fourth equation (Ampere's law)

The magnetic field can be generated in two ways either by applying electric current or by changing the electric field. It is the creation of an induced H field due to charge flow.

$$\nabla \times H = J + \epsilon_m \frac{\partial E}{\partial t} \quad (2.6)$$

Where,  $\epsilon_m$  is the electric permittivity of the medium. Note that the  $\epsilon_m$  is also a permittivity tensor quantity explained in section 2.5.4.

## 2.2.5 Wave equation

The above equations (2.3) - (2.6) can be combined to form the wave equation.

$$\nabla^2 E - \mu_m \epsilon_m \frac{\partial^2 E}{\partial t^2} = \mu_m \frac{\partial J}{\partial t} + \frac{\nabla \rho}{\epsilon_m} \quad (2.7)$$

From the equation (2.7), using curl's identity operation it can be given as below.

$$\nabla^2 E = \nabla(\nabla \cdot E) - \nabla \times (\nabla \times E) \quad (2.8)$$

Maxwell's equation in a homogenous and lossless dielectric medium is therefore written in terms of the electric field E and magnetic field H as [22]

$$\nabla \times E = 0, \quad \nabla \times E = -\frac{\partial H}{\partial t} \quad (2.9)$$

$$\nabla \times H = 0, \quad \nabla \times H = \mu_m \epsilon_m \frac{\partial E}{\partial t} \quad (2.10)$$

From equation (2.8) the standard forms of the wave equation (Helmholtz equation) can be derived as below.

$$\nabla^2 E = \mu_m \epsilon_m \frac{\partial^2 E}{\partial t^2} \quad (2.11)$$

$$\nabla^2 H = \mu_m \epsilon_m \frac{\partial^2 H}{\partial t^2} \quad (2.12)$$

The above equations help understand the profile of the signal that is possible to propagate through an optical medium. The simplest form of this signal is a fundamental mode of either TE or TM polarization state. There are different waveguide structures which are explained briefly in section 2.3.

The simulation software version used for this research study is Lumerical 2022 R1.4. The solver tool packages available in the Lumerical platform such as Finite-Difference-Time-Domain (FDTD) and Eigen Mode Expansion (EME) were used. The FDTD method is a state-of-art method for solving Maxwell's equations in complex geometry. It is a time and space solution with unique insights in useful quantities such as transmission/reflection of light and Poynting vector. Moreover, FDTD scales very well with parallelization and broadband results. It is also one of the most versatile and accurate methods for simulating light propagation in nanoscale components with complex geometry.

The EME method is a frequency domain method for solving Maxwell's equations. The EME method is well-known for simulating long-distance propagation in the waveguide as its algorithm is fully vectorial and bi-directional. The key advantage of this method is that the computational cost scales exceptionally well with the propagation distance. It is a very efficient method for extracting the full S-matrix of passive components. It divides the structure into continuously varying cross-sectional sub cells (CVCS) and computes the modes at the interface between adjacent cells. The benefit of this solver is that once in analysis mode, the user can perform a propagation sweep or frequency sweep without having to repeat the simulation. It is efficient in saving simulation time compared to the FDTD solver.

## 2.3 Waveguide structures

The structure of the waveguide is responsible for the optical confinement of the mode in the core. The fabrication complexity in terms of yield and tolerance varies with the type of structure. The schematic representation of some of the different structures of waveguides is shown below.

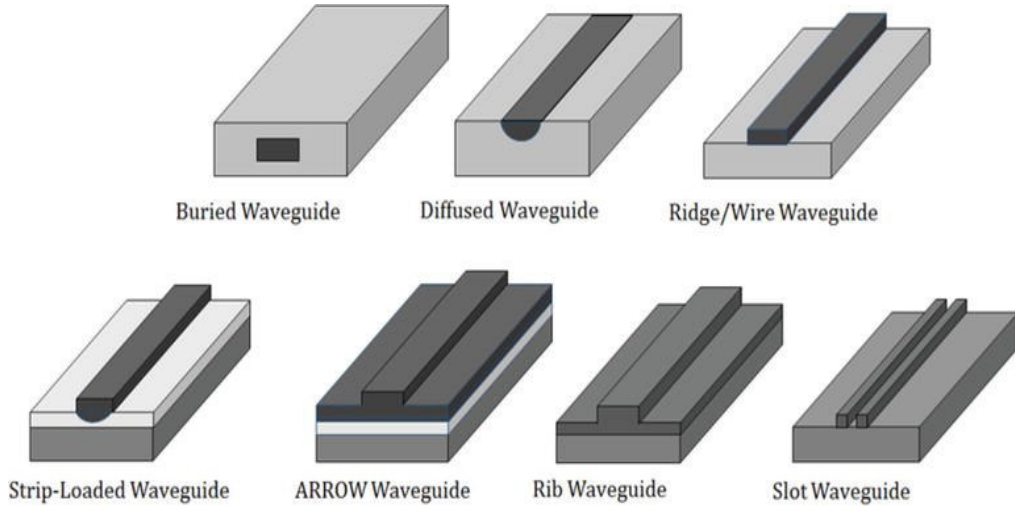


Figure 2.2 Different structures of waveguide [23]

## 2.4 Waveguide modes

A waveguide mode is a transverse field pattern whose amplitude and polarization profiles remain constant along the longitudinal z coordinate. Waveguide modes exist that are characteristic of a particular waveguide structure illustrated in 2.3. Therefore, the electric and magnetic fields of a mode can be written as shown in the equation (2.13) and (2.14).

$$E_v(r, t) = E_v(x, y) \exp(i(\beta_v z - \omega t)) \quad (2.13)$$

$$H_v(r, t) = H_v(x, y) \exp(i(\beta_v z - \omega t)) \quad (2.14)$$

Where  $v$  is the mode index,  $E_v(x, y)$  and  $H_v(x, y)$  is the mode field profiles, and  $\beta_v$  is the propagation constant of the mode.

## 2.5 Polarization

Polarization is a geometrical property applying to transverse electromagnetic waves which propagate inside the waveguide and is represented by the geometrical orientation of the electric and magnetic field oscillations associated with the propagating wave. The light wave propagating inside the dielectric optical medium can be polarized which means it can have transverse electric (TE) mode or transverse magnetic (TM) mode.

### 2.5.1 Transverse Electric (TE) mode

In this mode, the electric field is transverse to the direction of wave propagation and the magnetic field is not. The magnetic field has both transverse and longitudinal components where  $H_z \neq 0, E_z = 0$ . TE mode is also known as H mode where only a magnetic field exists in direction of propagation. TE mode in a waveguide is represented as  $\text{TE}_{mn}$ .

### 2.5.2 Transverse Magnetic (TM) mode

In this mode, the magnetic field is transverse to the direction of wave propagation (z-axis) and the electric field is not. The magnetic field has both transverse and longitudinal components where  $H_z = 0, E_z \neq 0$ . TM mode is also known as E mode where only an electric field exists in direction of propagation. TM mode in a waveguide is represented as  $\text{TM}_{mn}$ .

Figure 2.3 and Figure 2.4 are obtained from a rib-waveguide structure using the same simulation software used for this study. The FDTD has an integrated MODE solver and is one of the tools used to plot the field profile of TE and TM fundamental mode respectively. In Figure 2.3 the dominant component of the electric field is in the  $E_x$ -direction, so the mode is called fundamental TE mode. Here the color bar represents the field intensity of the mode.

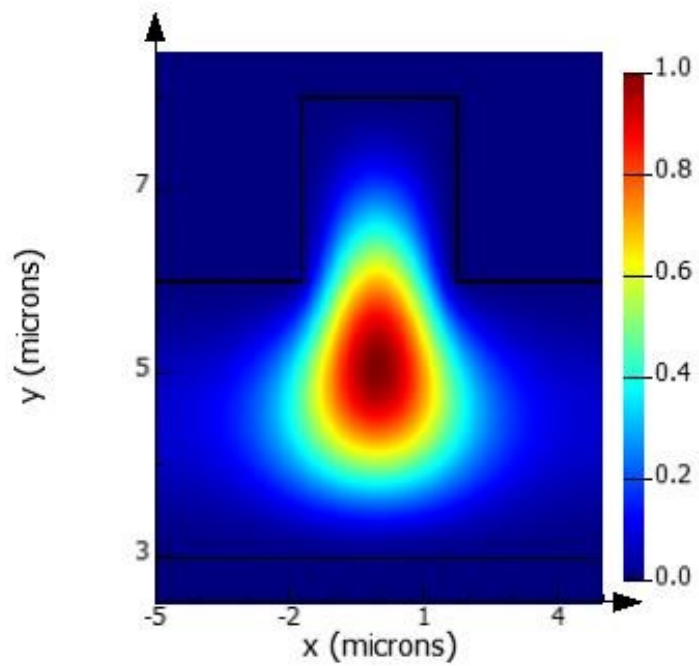


Figure 2.3 Fundamental TE mode of a rib-waveguide using Lumerical MODE solver

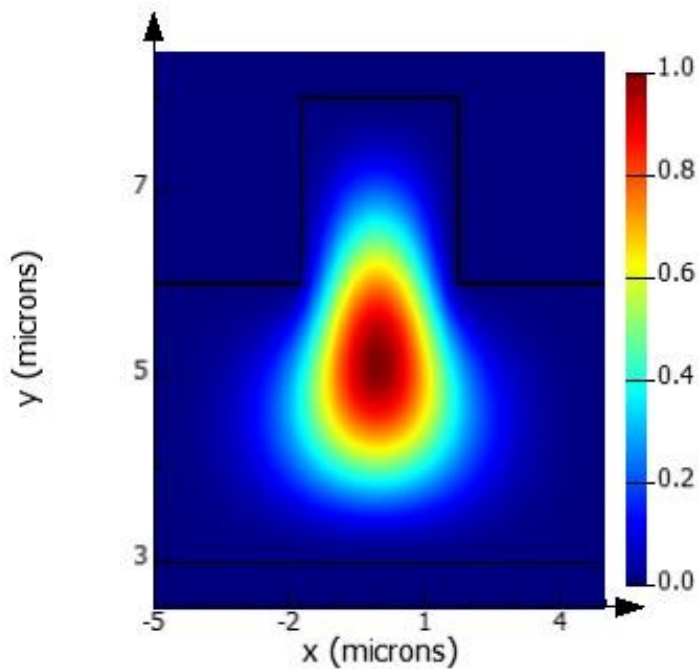


Figure 2.4 Fundamental TM mode of a rib-waveguide using Lumerical MODE solver

Similarly, in Figure 2.4 the dominant component of the electric field is in the  $E_y$  direction, so the mode is called as fundamental TM mode. Here the color bar represents the field intensity of the mode. The field profile of both TE and TM is the propagating power confinement of the mode. The power has a Poynting vector in the direction of the propagation.

### 2.5.3 Poynting vector

The Poynting vector was named after John Henry Poynting. It is the result of the vector product of the electric and magnetic field components. It is used to reflect the energy flux density of the electromagnetic field [22]. The numerical representation of the Poynting vector is given as equation (2.15).

$$S = E \times H = \sqrt{\frac{\epsilon_m}{\mu_m}} E^2 \quad (2.15)$$

Where,  $\epsilon_m$  is the permittivity of the medium and the  $\mu_m$  is the permeability of the medium.

### 2.5.4 Birefringence

In the general case of loss-less medium,  $\epsilon_r(R)$  is a function of the spatial coordinates and can be expressed (in a cartesian coordinates system) as a real, second rank tensor in the form

$$\epsilon_r(R) = \begin{bmatrix} \epsilon_{xx} & \epsilon_{xy} & \epsilon_{xz} \\ \epsilon_{yx} & \epsilon_{yy} & \epsilon_{yz} \\ \epsilon_{zx} & \epsilon_{zy} & \epsilon_{zz} \end{bmatrix} \quad (2.16)$$

This symmetric ( $\epsilon_{ij} = \epsilon_{ji}$ ) matrix [3,3] is a special case of a Hermitian matrix (a complex square matrix that is equal to its conjugate transpose), resulting in pure eigenvalues and eigenvectors and therefore consists of a total six elements. The magnitude of each tensor component  $\epsilon_{ij}$  depends on the relative orientation of the

x, y, and z-axis to the propagation axis of the medium. It is always possible to choose the orientation of the coordinate system in a way that the axis is parallel to the eigenvectors. In this case, the permittivity tensor reduces to diagonal form.

$$\epsilon_r(R) = \begin{bmatrix} \epsilon_{xx} & 0 & 0 \\ 0 & \epsilon_{yy} & 0 \\ 0 & 0 & \epsilon_{zz} \end{bmatrix} \quad (2.17)$$

If we replace  $\epsilon_{xx}, \epsilon_{yy}, \epsilon_{zz}$  with  $\epsilon_x, \epsilon_y, \epsilon_z$  respectively we can get the effective dielectric permittivity along with the set of the three-axis which is called the principle dielectric axis of the medium.

$$\epsilon_r(R) = \begin{bmatrix} \epsilon_x & 0 & 0 \\ 0 & \epsilon_y & 0 \\ 0 & 0 & \epsilon_z \end{bmatrix} \quad (2.18)$$

The dielectric response of the anisotropic material using the electric permeability tensor can therefore be defined as

$$D_x = \epsilon_0 \epsilon_x E_x \quad (2.19)$$

$$D_y = \epsilon_0 \epsilon_y E_y \quad (2.20)$$

$$D_z = \epsilon_0 \epsilon_z E_z \quad (2.21)$$

Where,  $\epsilon_r (\epsilon_x, \epsilon_y, \epsilon_z)$  is the relative permittivity of the medium and  $\epsilon_0$  is the permittivity of free space. The principal axis imposes a different value of the effective permittivity and therefore a different phase velocity. In general, at a given direction of propagation in the medium, there exist two independently orthogonal linearly polarized eigenwaves with associated phase velocities and direction of polarization. Now, when a wave propagates in the z-direction and its linearly polarized field has an equal component in both the x-axis and y-axis, it will split into two components

linearly polarized in the x-axis and y-axis. These two directions impose two different refractive indices with two components propagating at different phase velocities according to their polarization state which is known as birefringence.

### 2.5.5 The illustration of waveguide modes

The waveguide mode is defined as the propagation mode confined inside a waveguide at a given wavelength and a stable shape in which the wave propagates. The waveguide modes are wavelength dependent and are always determined by the cross-sectional geometry and the refractive index contrast of the waveguide. The highest confinement of light within the core is defined as the guided modes.

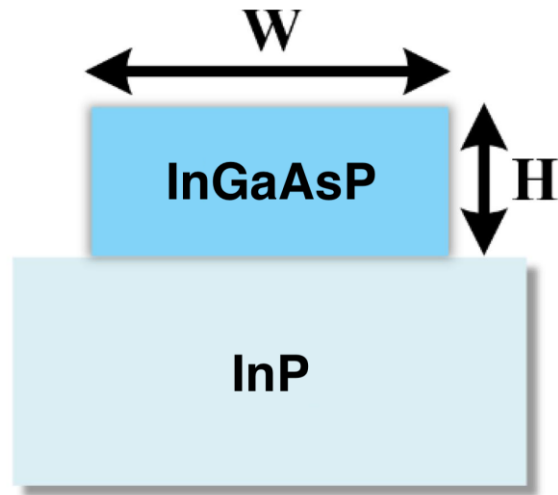


Figure 2.5 The structure of a ridge waveguide [ $W$ =width,  $H$ =height]

Figure 2.5 is a structure of a waveguide in an III-V material system. The purpose is to illustrate the fundamental  $TE_0$  and  $TM_0$  mode profiles and also the first two higher-order mode profiles (i.e.,  $TE_1$ ,  $TE_2$ ,  $TM_1$ ,  $TM_2$ ).

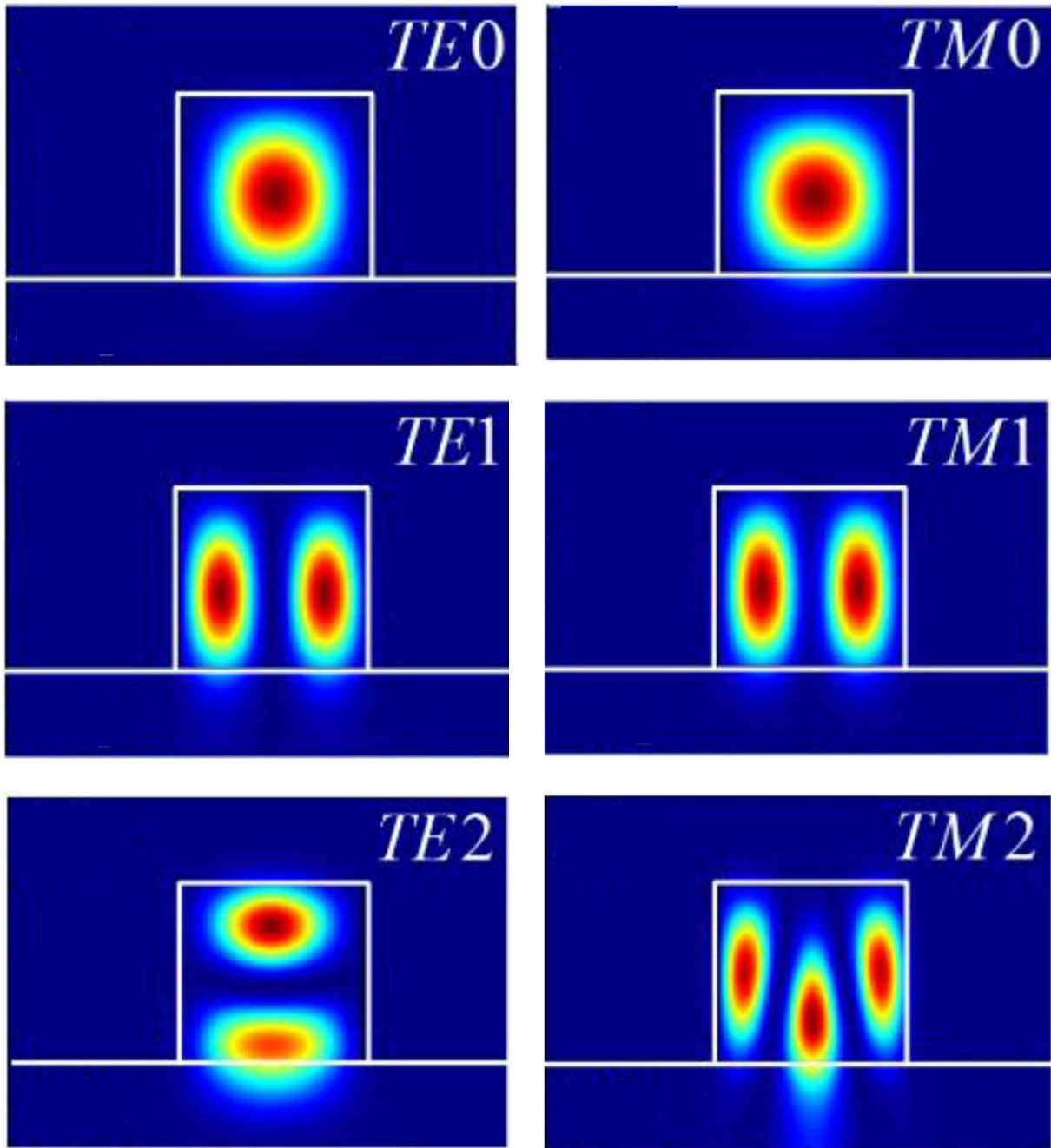


Figure 2.6 The mode profiles of  $TE_0$ ,  $TE_1$ ,  $TE_2$ ,  $TM_0$ ,  $TM_1$ ,  $TM_2$  of a ridge waveguide structure

In the test system of any photonic device, there may be a polarizer, crystals, or a wave plate introduced to achieve desired polarization of light. This polarized light can be represented by using Jones's calculus [24]. When the light propagates from an optical medium the resulting polarization of the emerging light can be derived by solving the product of the Jones matrix and the Jones

vector of the incident light. Moreover, the Jones calculus is only useful for the light which is fully polarized [24].

Various kinds of methods like Eigen Mode Expansion (EME), Finite Difference Time Domain (FDTD), Finite Difference Eigenmode (FDE), and Finite Element Eigenmode (FEEM) are developed to understand the nature of propagation for these guided modes [25]. The theoretical analysis of these guided modes can be solved using different methods such as the effective index method or coupled-mode theory. When two waveguides are in proximity, they become coupled and exchange power as a function of  $z$ . Very often, this leads to a periodic exchange of power between the waveguides. When the proximity between the two waveguides is increased or decreased the guided modes are coupled or de-coupled depending on the scenario. The coupling strength between the two modes depends on a dimensionless ratio (per unit length) between the coupling coefficients. The coupling coefficients and the phase mismatch are the important factors for the power exchange between different modes.

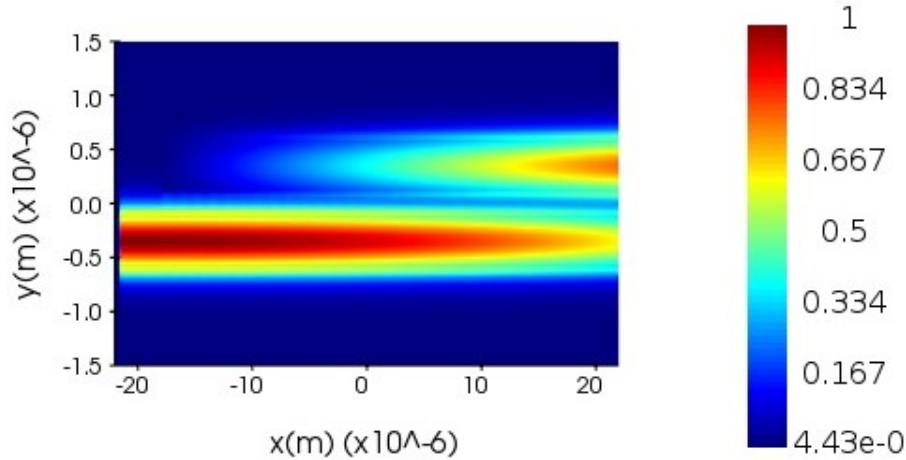


Figure 2.7 The Lumerical analysis of two waveguides in proximity – light coupling.

The field profile in Figure 2.7 is obtained from FDTD analysis using Lumerical simulation software of two slab waveguides of  $\sim 90 \mu\text{m}$  length acting as a directional coupler at 1550nm

wavelength. The material used here is InP as a substrate and InGaAsP for the core. There is a cladding layer of InP to achieve better vertical confinement. The graphical representation of two slab waveguides reflects the coupling of light when the waveguides are visibly in proximity. The coupling of light is calculated using the coupling coefficient which is defined as the ratio in dB of the incident power fed into the input port of one waveguide, to the coupled power of the second waveguide acting as an output port. Here, the color bar represents the magnitude of field intensity for each waveguide. The minimum coupling length ( $L$ ) and the minimum distance ( $d$ ) between two waveguides are two major important terms. One of the slab waveguides on the bottom is excited with an input source and due to phase-matching conditions, the light travels from one waveguide to another.

## 2.6 Figures of merit

The important quantity used to characterize the performance of a polarization rotator is discussed here. The important terms such as polarization extinction ratio (PER), insertion loss (IL), polarization-dependent loss (PDL), and coupling loss (CL) are reasonably defined.

### 2.6.1 Polarization extinction ratio (PER)

The polarization extinction ratio (PER) is the ratio of the optical powers of TE and TM polarizations. The PER is used to characterize the degree of polarization in a polarization rotator. The unit of PER is decibels (dB). The PER can mathematically be defined as equations (2.22) and (2.23).

$$PER_{TE-TM} = 10 \log_{10} \frac{P_{TM}}{P_{TE}} \quad (2.22)$$

$$PER_{TM-TE} = 10 \log_{10} \frac{P_{TE}}{P_{TM}} \quad (2.23)$$

## 2.6.2 Insertion loss (*IL*)

The insertion loss is the loss of signal power resulting from the insertion of a device in a transmission line. The unit of *IL* is decibels (dB). The insertion loss (*IL*) can mathematically be defined as equation (2.24).

$$IL = 10 \log_{10} \frac{P_{in}}{P_{out}} \quad (2.24)$$

where  $P_{in}$  is the power transmitted to the device before insertion and  $P_{out}$  is the power received by the device after insertion.

## 2.6.3 Polarization-dependent loss (*PDL*)

The polarization-dependent loss is a measurement of the peak-to-peak difference in the transmission of an optical component or system for all possible states of polarization. It is the ratio of the maximum and the minimum transmission of an optical device for all polarization states. The unit of *PDL* is decibels (dB). The polarization-dependent loss (*PDL*) can mathematically be defined as equation (2.25) [26].

$$PDL = 10 \log \frac{P_{max}}{P_{min}} \quad (2.25)$$

## 2.6.4 Coupling loss (*CL*)

The coupling loss is defined as the power loss that occurs when the coupling light is from one optical device or medium to another. The unit of *CL* is decibels (dB).

$$CL = 10 \log \left( 1 - \left( \frac{P_{max}}{P_{min}} \right) \right) \quad (2.26)$$

## Chapter 3 State of the art

The research and development carried out in recent years in terms of polarization rotators are briefly described in this chapter. The polarization rotator is classified into many different types. Some of the main examples are crystal, fiber-based, wave plate, and on-chip, polarization rotators. There are many promising designs developed and analyzed by researchers with their trade-offs in specification, workability, and fabrication level. Before entering the state of art, it is highly recommended to understand the conventional way of describing the polarization. We will therefore review the state of polarization of a propagating electromagnetic wave given by the Poincare sphere briefly. The active and passive polarization rotators available are also reviewed in this chapter.

### 3.1 Poincare sphere

The polarization ellipse theory by Fresnel describes the sinusoidal oscillation in the  $x$ - $z$  and the  $y$ - $z$  planes [27]. Unfortunately, the equations from the ellipse theory are not informative. Additionally, it is near impossible to state the orientation and the ellipticity angles viewing the polarization ellipse as shown in Figure 3.1.

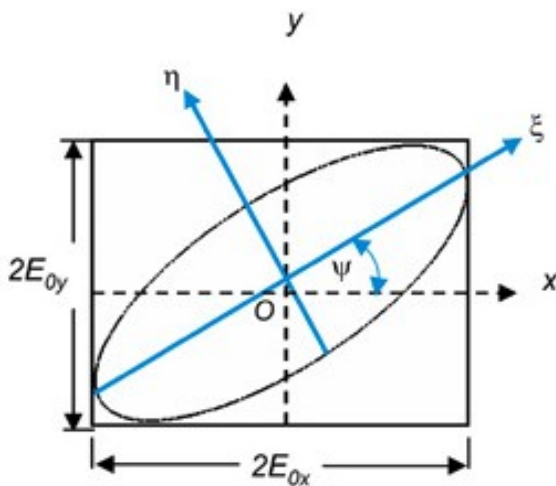


Figure 3.1 The Polarization Ellipse [27].

Therefore, Poincare (1892) suggested the Poincare sphere which is a graphical tool to visualize the propagating electromagnetic wave in three-dimensional space. Figure 3.2 provides the basic information on how the polarization changes and its cartesian coordinate system.

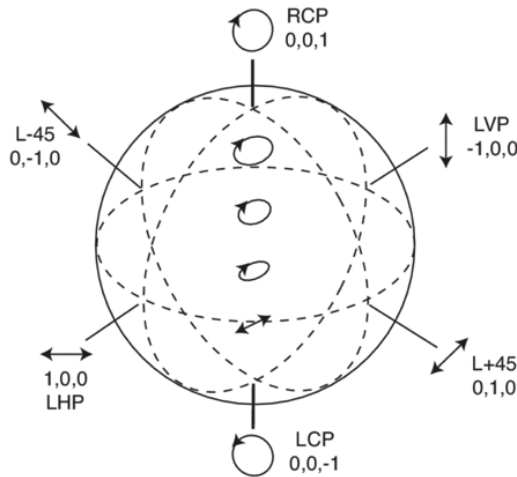


Figure 3.2 Poincare sphere elaborating the polarization states-[RCP – Right Circular Polarization, LCP – Left Circular polarization, LVP – Linear Vertical Polarization, LHP – Linear Horizontal Polarization, (L -45)- Right Elliptical Polarization, and (L +45)- Left Elliptical Polarization ] [28].

The linear, circular, and elliptical polarized light is represented by a point on the surface of the Poincare sphere. As seen in Figure 3.2, any given polarization state always corresponds to a unique point within the volume of the Poincare sphere.

- The circular polarization states are located at the poles, with intermediate elliptical states continuously distributed between the equator and the poles [i.e., RCP – Right Circular Polarization and LCP – Left Circular polarization].
- The linear polarization states are stated at the equator [i.e., LVP – Linear Vertical Polarization and LHP – Linear Horizontal Polarization].
- The right elliptical polarization (L -45) occupies the northern hemisphere.

- The left elliptical polarization (L +45) occupies the southern hemisphere.

These coordinates pairs are the representation of the polarization state of any propagating electromagnetic wave and are always represented in pairs as in equation (3.1) [24].

$$(2\Psi, 2X) \quad (3.1)$$

The degree of the polarization state (*DOP*) is stated in equation (3.2).

$$DOP = \frac{I_{pol}}{(I_{pol} + I_{unp})} \quad (3.2)$$

Where the *DOP* is the degree of polarization,  $I_{pol}$  is the intensity of the polarized light and  $I_{unp}$  is the intensity of the unpolarized light [28]. The value of *DOP* is 0 and 1 when the light is unpolarized and polarized respectively.

### 3.2 Polarization rotator

The polarization rotator is the device that allows the input polarization states to rotate into another state of polarization in a controlled path, i.e., from TE to TM or TM to TE. There are devices where the input state of polarization has both TE and TM polarization where it depends on the desired output polarization. Then either polarization is suppressed to achieve the desired state of polarization. The best example of this kind of device is the one with four ports. These devices can either make use of crystals, an optical fiber-based design, or dielectric waveguides.

#### 3.2.1 Crystal based polarization rotator

The crystal-based polarization rotators use multiple internal reflections to rotate the light into the desired polarization. The crystal-based polarization rotator has gained much interest in recent years. Due to the advancement in organic material technology, there are numerous innovations carried out where the plasticity of the material is used to carry out an active or passive polarization

rotation depending on the nature of the application [29] [30] [31]. Figure 3.3 and Figure 3.4 shows one of the recent advancements where the plasticity of the crystal is used as a path to rotate the polarization of the light.

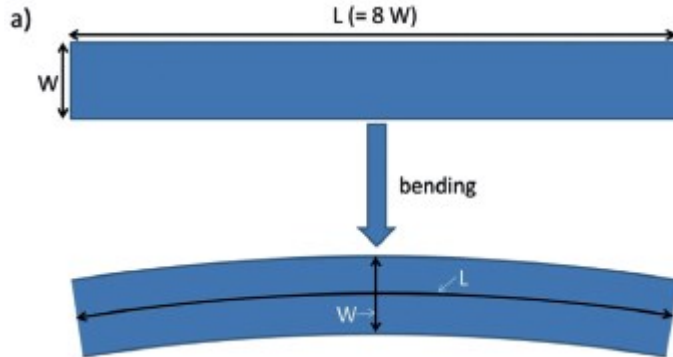


Figure 3.3 The bending of a crystal-based polarization rotator before the width is bent [29].

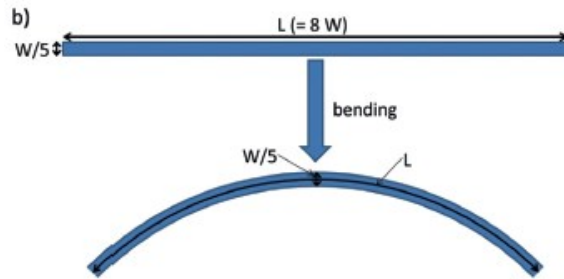


Figure 3.4 The bending of a crystal-based polarization rotator after the width is bent [29].

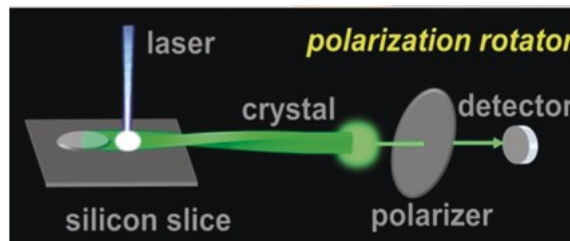


Figure 3.5 The block diagram of the polarization rotation system [29].

As seen in Figure 3.5, the left side of the crystal was fixed on a silicon slice with the wider face of the crystal being horizontal. A polarization analyzer was set between the right end of the crystal and a spectrometer to obtain the results. Figure 3.6 shows different twisting angles of the device

which acts as a polarization rotator. Here, the polarization rotation is controlled by the twisting angle.

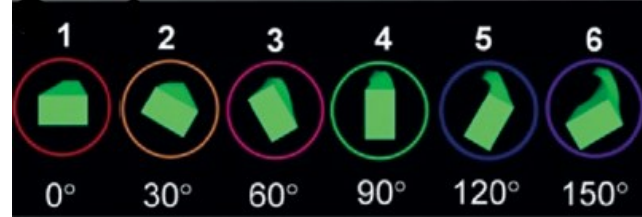


Figure 3.6 The different crystal twisting angles of the polarization rotator [29].

Figure 3.7 shows the correlation between the twisting angle against the polarization rotation angle after the experiment was performed for each twisting angle. Here, polarized light was used as an input source.

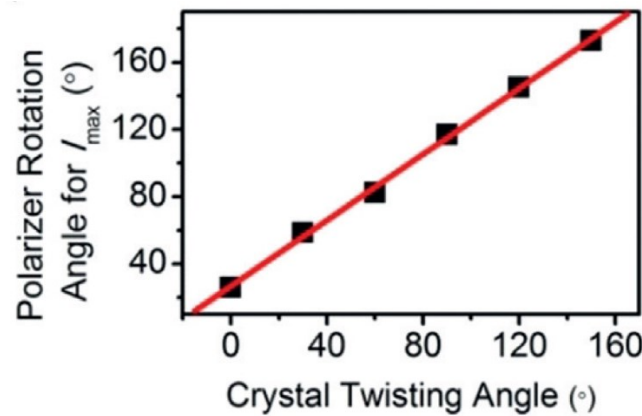


Figure 3.7 Linear correlation between the crystal twisting and polarization rotation angle [29].

### 3.2.2 The optical fiber-based polarization rotator

In an optical fiber polarization rotator, there is an intentional birefringence introduced at a definite length of the fiber which is called the beat length and is represented by  $L_b$ . The birefringence can be introduced by a twist at an angle or a bend that changes the uniformity of the optical fiber. When this kind of fiber is intentionally fabricated, they act to maintain certain polarization for an optical system. The structure of the fiber (bend, twist, etc.) if changed the

coupling coefficient of the fiber changes accordingly. This coupling coefficient will define the polarization modes to propagate with a phase velocity similar if there are two polarization modes.

There are many optical fiber polarization controllers available in the field which consist of multiple free space waveplates oriented at  $45^\circ$  from each other. The illustration shown in Figure 3.8 is the polarization-dependent fiber with several waveplates squeezed at different positions on the fiber to maintain a defined polarization state for an optical system or a device [28]. A fiber with a similar operating principle would reduce the insertion loss ( $IL$ ) and the cost of manufacturing the tunable polarizer compared to various available devices [28] [31].

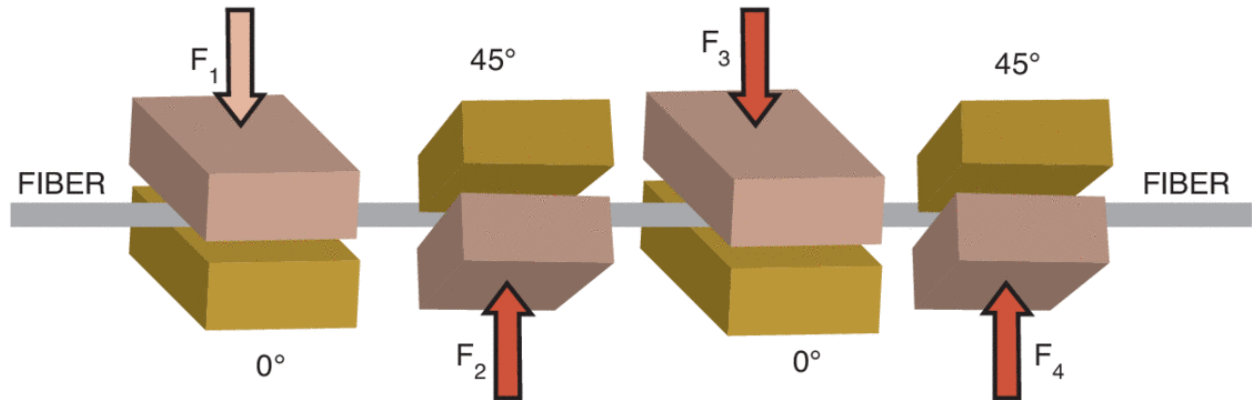


Figure 3.8 Polarization controlled fiber by squeezing fiber and angled waveplates [28].

### 3.2.3 On-chip polarization rotator

An on-chip polarization rotator advances photonics integrated circuits (PICs) and their applications as the polarization management is extremely important where geometrical anisotropy and fabrication inaccuracies play a critical role. The On-chip polarization rotator can be distinguished into two different forms namely active polarization rotator and passive polarization rotator.

### 3.2.3.1 Active polarization rotator

The active polarization rotation can be achieved by using the thermo-optic tuning and MEMS tuning which can effectively change the refractive index of the semiconductor material as well as the mode propagating through the optical path or waveguide by applying a constant or a variable voltage. The voltage applied during the tuning process acts as an external source to manage the desired polarization state on the active modulation of light in III-V based modulator or silicon on insulator-based optoelectronics. Figure 3.9 is a novel design of a highly tunable compact polarization rotator based on silicon on an insulator platform that was published in the year 2019.

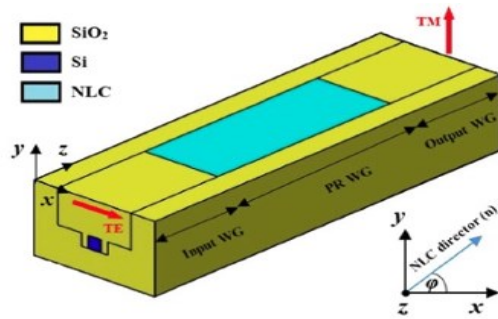


Figure 3.9 The electrically tunable polarization rotator [32]

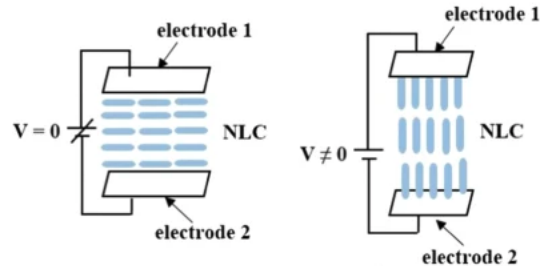


Figure 3.10 The Nematic Liquid Crystal (NLC) molecule's orientation at different bias states [32]

The polarization conversion ratio was tuned by controlling the rotation angle of the nematic liquid crystal molecules via an external electric field as shown in Figure 3.10 [32]. Here, a silicon wire is inserted inside a groove in the  $\text{SiO}_2$  substrate. The silicon wire is surrounded from three

sides by NLC. The NLC chemical structure has a suitable operating temperature of about  $\sim$ 60°C. The anisotropic property of the liquid crystal material leads to hybrid modes and results in power exchange between two orthogonal polarized modes. Although, this design is studied regarding the tolerance error and to achieve a high ER and less IL it doesn't promise the compatibility in the co-packaged modulators where there are multiple output waveguides in proximity. The drawback of the polarization rotators using the thermo-optic effect is that the control of the temperature using an external electrical signal on the waveguides close is a challenge. This may induce some polarization errors due to crosstalk where the design of the device must be traded off with performance. The similar concept of mechanical tuning-based polarization rotators uses phase three-dimension bend cavities to create a two-dimension momentum space where the bends act and follows the principle of a ring resonator. This ring resonator structure is bandwidth limited due to its band spectral features [33].

### **3.2.4 Passive polarization rotator**

The transformation of TE to TM or vice versa without any use of an external electrical field is called passive polarization rotation. The three main important concepts in polarization rotations are mode evolution, mode coupling, and mode hybridization [34]- [35].

#### **3.2.4.1 Mode evolution and structures**

The mode evolution mechanism is basically to convert a fundamental TM mode into the second-order TE mode without changing the polarization of the fundamental TE mode or vice versa. The mode evolution structures are wavelength dependent and are fabrication tolerant. They operate at a broad wavelength range and can be robust to dimensional changes.

Devices such as a polarization splitter are the prototypical example of the mode evolution principle. Figure 3.11 shows the basic concept proposed by the researcher with a high fabrication

tolerance ratio and yield compared to the mode coupling structures. The structure illustrated in Figure 3.11 is based on the InP/InGaAsP material system. It consists of a bi-level taper pre-converter and a width taper.

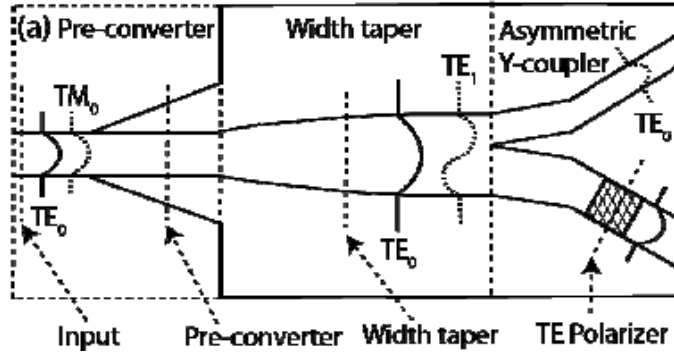


Figure 3.11 The mode evolution-based polarization rotator-splitter design via a simple fabrication process [36].

In the pre-converter section, the propagating modes are  $TE_0$  and  $TM_0$ . As soon as the  $TM_0$  mode reaches the width taper, the polarization conversion occurs due to the bi-level taper structure inducing the change in the mode profile of the propagating mode. The bi-level structure adds the refractive index change along the propagation direction. The transformation is from  $TM_0$  mode to  $TE_1$  without changing the  $TE_0$  mode. This  $TE_1$  mode when reaches the Y-coupler, splits the fundamental and the second-order TE mode into fundamental TE mode.

The rotation of the polarization is  $90^\circ$  and the approximate rotation efficiency is 95% [36]. Due to the high fabrication tolerance ratio, high *ER*, and low *IL*, this is one of the most likely candidates to be able to integrate inside a commercial photonic chip.

### 3.2.4.2 Mode coupling and structures

The mode coupling mechanism is based on transferring the power of propagating mode from one waveguide to another waveguide when placed close. Here two conditions are to be achieved

to have higher coupling and conversion efficiency. If waveguide  $A$  and waveguide  $B$  are two waveguides, then the below two conditions have to be achieved.

- Significant index mismatch [i.e.,  $n_{eff}^B(TE) < n_{eff}^A(TM)$ ]
- Phase matching condition [i.e.,  $n_{eff}^B(TE) \cong n_{eff}^A(TM)$ ]

The mode coupling structures are dedicated to the principle of phase matching and these structures use finely tuned coupling [34]- [35]. A device such as a directional coupler is the prototypical example of this theory. Mode coupling structures require precise placement of the material stack/geometrical modifications causing manufacturing yield decreases, and the cost of fabrication increases gradually. Figure 3.12 shows an example of a polarization rotator based on SiO<sub>2</sub> working on the principle of mode coupling.

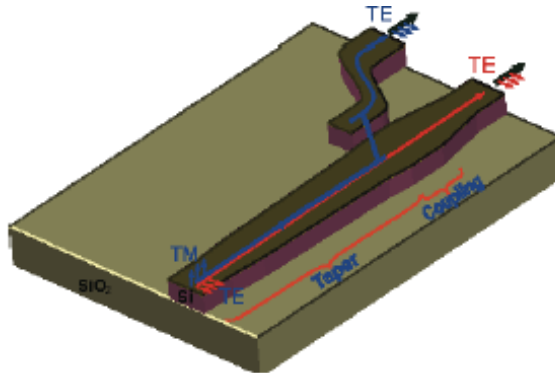


Figure 3.12 The polarization rotator based on the mode coupling principle [37]

The TE and TM mode (light) propagates inside the taper input waveguide. When this mode reaches the length where the second waveguide with different width is placed in proximity, the light gets coupled to the second waveguide. Due to significant index mismatch and phase matching conditions, the TM mode gets converted into TE mode and gets through two output ports.

The polarization splitter-rotator has shown in Figure 3.12 consists of a taper and an asymmetrical directional coupler. Here the taper structure plays an important part to convert the input TM fundamental mode to the higher-order TE mode. The conversion occurs when the light

propagates along a width-varying taper section. The working principle is mode coupling caused due to high-index contrast waveguide with an asymmetrical cross-section.

### 3.2.4.3 Mode hybridization

By breaking the symmetric structure of the waveguide, the propagation modes are hybridized in which the optical power is transferred periodically between two desired polarization states [38]. Rotation is enabled through the interference of the two hybridized modes where the cladding of the waveguides needs to be asymmetric. These require sharp edges and narrow trenches that are very difficult to etch at the nano level. The fabrication yield of these structures is very low and needs some extra fabrication steps and an insulating material mask layer while going through the process. Figure 3.13 [38] shows the example of the mode hybridization-based Si polarization rotator proposed in 2015 where double stair waveguides are being used as an asymmetric structure. Although the narrow trenches ( $\sim 10\text{nm}$ ) required for mode hybridization are difficult to pattern and etch with the controllable profiles, the double stair waveguides offer good results, but they exhibit wavelength-dependent loss because the working principle relies on interference.

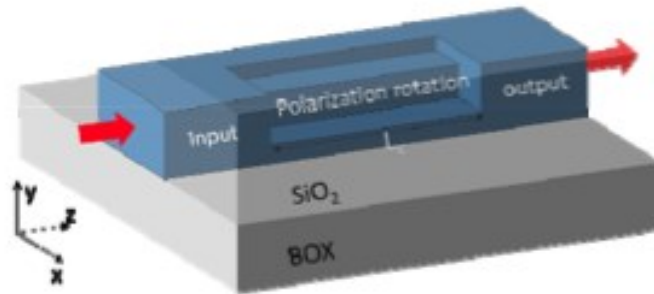


Figure 3.13 Polarization rotator based on mode hybridization [38]

Some of the structures reviewed in the literature study have set the state of the art. The importance of performing this literature review was to assess the ideas of the past proposed devices and apply modifications to be able to develop a new polarization rotator based on the mode

evolution principle using the group III-V material system, which is analyzed in terms of fabrication tolerant, insertion loss, extinction ratio.

Sr no.	Author	Art of proposal	Year	Material	Wavelength	Polarisation conversion	Conversion Length of device	General Losses / Gains
1	Velko P. Tzolov et al. [39]	Numerical	1995	InP/InGaAsP	N/A	92-93%	250 $\mu\text{m}$	Coupling Loss = 2.5 dB
2	J. Z. Huang et al. [40]	Experimental	2000	GaAs/AlGaAs	1.55 $\mu\text{m}$	96%	720 $\mu\text{m}$	The propagation loss for the input symmetric waveguides = 0.65 dB/mm The polarization converter section loss = 1.25 dB/mm
3	B. M. A. Rahman et al. [41]	Numerical	2001	GaAs/AlGaAs	1.55 $\mu\text{m}$	More than 99%	320 $\mu\text{m}$	$IL = 0.4 \text{ dB}$
4	S . S . A. O B A Y Y A et al. [42] [43]	Numerical	2003	InP/InGaAsP	1.55 $\mu\text{m}$	99.8%	403 $\mu\text{m}$	$IL = 0.64 \text{ dB}$
5	Hatem El-Refaei et al. [44]	Theoretical (C-band)	2003	InP/InGaAsP	1.53 $\mu\text{m}$ - 1.57 $\mu\text{m}$	99.68%	~226 $\mu\text{m}$	$Er = -25 \text{ dB}$
6	Hatem El-Refaei et al. [44]	Experimental (C-band)	2004	InP/InGaAsP	1.53 $\mu\text{m}$ - 1.57 $\mu\text{m}$	97.5%	330 $\mu\text{m}$	$Er = < -20 \text{ dB}$ Excess loss = 0.02 dB
7	M Nikoufard et al. [45]	Theoretical (Air trenches)	2005	InP/InGaAsP	1.55 $\mu\text{m}$	98%	1.5 $\mu\text{m}$	$IL = 0.2 \text{ dB to } 0.3 \text{ dB}$ $Er = 14 \text{ dB to } 36 \text{ dB}$
8	Maria V Kotlyar et al. [46]	Experimental (Air trenches)	2005	InP/InGaAsP	1.17 $\mu\text{m}$ – 1.37 $\mu\text{m}$	96%	1.5 $\mu\text{m}$	$Er = 14 \text{ dB}$
9	L.M. Augustin et al. [47]	Experimental	2007	InP/InGaAsP	1.55 $\mu\text{m}$	97%	131 $\mu\text{m}$	Excess loss = $2.4 \pm 0.3 \text{ dB}$ for TE and $2.6 \pm 0.3 \text{ dB}$ for TM
10	Zhechao Wang et al. [48]	Theoretical	2008	Si	1.49 $\mu\text{m}$ – 1.6 $\mu\text{m}$	99.95%	~22.1 $\mu\text{m}$	Mode mismatch loss = 0.22 dB
11	Hiroshi Fukuda et al. [49]	Theoretical	2008	SiO <sub>2</sub> /Si	1.55 $\mu\text{m}$	N/A	35 $\mu\text{m}$	$Er = 11 \text{ dB}$ Excess loss = 1 dB
12	C. Alonso-Ramos [50]	Theoretical	2012	InP	1.55 $\mu\text{m}$	N/A	804 $\mu\text{m}$	$Er = 40 \text{ dB}$ $IL = 0.04 \text{ dB}$ $Er = 20 \text{ dB}$ [C-Band]
13	Masaru Zaitsu et al. [51]	Experimental	2013	InP/InGaAsP	1.51 $\mu\text{m}$ – 1.57 $\mu\text{m}$	96%	150 $\mu\text{m}$	On-chip loss = Less than 0.1 dB
14	Yule Xlong, Winnie N. Ye et al. [52]	Theoretical	2014	SiO <sub>2</sub> /Si	1.53 $\mu\text{m}$ - 1.57 $\mu\text{m}$	99 % - 99.5%	17 $\mu\text{m}$ - 27 $\mu\text{m}$	$Er = 17 \text{ dB}$ $IL = -0.3 \text{ dB}$
15	Chyong-Hua Chen et al. [53]	Theoretical	2017	SOI	1.53 $\mu\text{m}$ - 1.57 $\mu\text{m}$	N/A	25.3 $\mu\text{m}$	$IL = -0.51 \text{ dB}$ $Er = 32.27 \text{ dB}$
16	Zheng-Yong Song [54]	Theoretical	2018	Meta surface Material	Microwave frequency	71%		N/A
17	Zhi-Shan Hou et al. [55]	Experimental (Twisted WG)	2019	SU-8/Si	1.55 $\mu\text{m}$	More than 90%	150 $\mu\text{m}$	N/A
18	Abdulaziz E. Elfiqi et al. [56]	Experimental	2020	InP/InGaAsP	1.55 $\mu\text{m}$	More than 95%	150 $\mu\text{m}$	Tolerance $\pm 16\%$ On-chip loss = 4-6dB

Table 3.1 State of art-literature review

Table 3.1 below compares some recent designs from the literature in terms of different figures of merit and the relevancy of the design. All the designs have been published and have been important in the evolution of the concept and design of a polarization rotator. These design references range from 1995 to 2020. The work described includes designs based on either numerically, theoretically, or experimental basis with different material systems such as III-V, Si, and Meta surface.

### **3.3 Conceptual preference**

The state of art devices presented in Table 3.1 are illustrations based on all the three-polarization rotation mechanisms i.e., mode coupling, mode evolution, and mode hybridization. The trade-offs relative to fabrication yield, tolerances, device length, figures of merit, material system, and polarization conversion efficiency are some of the major concerns when choosing a device to be fabricated and integrated with the photonic system at the commercial stage. The foremost motivation when budgeting this kind of integration is to reduce the mass production cost, reduced package size, and complexity, and achieve high yield. These key motivations are directly related to the reliability of the device and the improved testability of the integrated device [57]. The variability effect works on different scales such as intra-die (geometry of die), intra-wafer (die-die), and wafer to wafer (lot-to-lot) [57]. The variability at different levels of fabrication can be listed as:

- Process conditions
- Device geometry
- System performance
- Optical base properties
- Circuit properties

Practically two approaches were found to be commonly used when studying the details obtained from the major market leaders, conferences, and research articles. The flow can be stated as:

- Design → fabricate → test → simulate-optimize → mass production
- Design → simulate-optimize → fabricate (small batch) → test → optimize → mass production

Both the above flows have their unique significance when it comes to studying the tolerance of the device. The first approach is to design the device without considering any fabrication tolerance data that might be known or necessary to be included (dimension, accuracy, etc.). Thereafter few devices are fabricated and tested on a test station. This helps to understand the characteristics of the designed device at an experimental level. Afterward, the simulation of the design is carried out and experimental results are compared to evaluate the changes needed for developing an optimum design. At this step, the fabrication error and tolerance values are known, and the simulation design is optimized accordingly followed by the mass production. This may lead to higher loss (cost and time) in a scenario of design failure after the mass production.

The second approach is to design the device and gather the simulation data including any fabrication tolerance data that might be known (dimension, accuracy, etc.). The obtained simulation result is then analyzed, and the design is optimized relying on the simulation output data. Thereafter, a small batch of devices is fabricated and tested at the test station. This helps to understand the characteristics of the designed device at an experimental level. At this step, any additional fabrication error and tolerance values are known (if present) and the simulation design is optimized accordingly followed by the mass production. The second approach may cover all the important details of fabrication and treat the failure considerably better with cost and time.

Many designs have been proposed in the past and may have not claimed a second approach. The academic level of experiments is conclusive but at a higher fabrication quantity, they may not have essential data gathered for studying the tolerance of the device due to minimal samples available for their study. The thesis work proposed here is the partial completion of the second approach where state of the art will be designed and simulated using the Lumerical software platform and will be optimized at a certain level keeping all the available tolerances in consideration from the past research studies where the smaller batch of the devices can feasibly be fabricated in the foundry while the continuation of this research. This small batch of wafers or die will add and provide some practical tolerance errors that can only be traced at the foundry level and after the testing of the devices. Few of the variability factors are already mentioned in section 3.3. The next chapter covers the state-of-art design of this research study.

## **Chapter 4 Design and Simulation**

Polarization rotation can be achieved in different ways, as discussed in section 3.2.4. In this research study, the goal is to achieve polarization rotation using combined methods. The lower refractive index contrast in InP/InGaAsP material induces weak vertical modal confinement in the core and higher polarization conversion efficiency can be challenging. The use of the mode coupling method in which two waveguides are placed close reaches phase matching condition to achieve desired polarization state is proved efficient in Si-based material. Moreover, this concept is difficult to achieve using InP/InGaAsP material system. The tolerances concerning width, height, and coupling gap are highly sensitive to affecting the efficiency of the device.

Moreover, from the previous research claims, few published designs support both simulated and fabricated results for InP/InGaAsP. Mode evolution and mode hybridization are the two methods where most of the polarization rotation study for group III-V material has been carried out. However, the goal here is to design a polarization rotator using the possible combined method at the simulation level. The software version used for this research study is Lumerical 2022 R1.4. The configuration of the computer system used was Intel® Xeon® CPU E5-2637 v4 @3.50GHz. The solver tool packages available in the Lumerical platform such as Finite-Difference-Time-Domain (FDTD) and Eigen Mode Expansion (EME) were used.

### **4.1 Approach**

The design of the polarization rotator can be approached as a combination of mode evolution and mode hybridization methods. Here the design is simulated and studied with different lengths ( $L$ ), width ( $w$ ), and thickness ( $d$ ) of the core. The  $TE_0$  (or  $TM_0$ ) mode source when injected into the input port of the polarization rotator, first transforms it to hybrid modes and then to  $TM_0$  (or  $TE_0$ ). The simulation is carried out using the Lumerical 3D-FDTD solver. This allows us to

propagate and record several different parameters at a certain length such as source selectivity and profile, mode field intensity, polarization fraction (%), polarization conversion efficiency (PCE), mode expansion results (s-parameter), transmission power ( $P$ ), Eigenmodes ( $n$ ), loss, effective refractive index ( $n_{eff}$ ) and many more for the waveguide cross-section. The mode expansion monitors act as a polarization analyzer for this study which provides a detailed overview of the conversion from TE $\rightarrow$ TM or vice versa.

## 4.2 Design of the Polarization Rotator

The design of the polarization rotator is based on past studies carried out that aimed at the same outcome [51] [56]. Several designs published in Table 3.1 showcased complicated structures (slopes, twists bends, stacked taper, etc.) where the fabrication process would not result in a better yield. These structures are difficult to integrate with the PIC elements due to the limitation of device dimensions. The deeper-etch ridge structure used in the previous studies [51] [56] lacked fabrication tolerance where controlling the width and the thickness of the waveguide were major concerns. The polarization conversion efficiency would not be uniform for devices with varying waveguide dimensions.

Observations from the performed literature review, the design studied in this work is resistant to the fabrication error. If the width ( $w_1, w_2$ ) obtained after the fabrication is not precise compared to the selected dimensions, the rotation of the polarization state will still occur but at a different position on rotator length. The conversion efficiency of the device would still be acceptable, and the range of polarization conversion efficiency values obtained for different widths will further be explained in Table 5.3. The broad range of width ( $0.75\mu m \sim 1.35\mu m$ ), single waveguide structure with foundry compatible waveguide dimensions, and the inserted etch-stop layer to control the thickness of the ridge waveguide make this design compact and robust.

The optimization of the design is done using the capabilities of the design and simulation software mainly the Lumerical solver tools in this case. The design study is carried out on three rotator lengths ( $150\mu\text{m}$ ,  $200\mu\text{m}$ ,  $250\mu\text{m}$ ), a combination of various widths ( $0.75\mu\text{m}$ ,  $0.85\mu\text{m}$ ,  $0.95\mu\text{m}$ ,  $1.15\mu\text{m}$ ,  $1.25\mu\text{m}$   $1.35\mu\text{m}$ ) and the wavelength dependency for C-band ( $1.53\mu\text{m}$ - $1.565\mu\text{m}$ ).

#### 4.2.1 Design principle

To design a polarization rotator at the micrometer scale, precision is a key factor. The meshing of the geometry, cladding dimensions, and its material composition and selection, the frequency range of the solvers, boundary conditions, volume of the simulated area chosen, a cross-section of the monitors to measure the parameters and more are the key things to watch for in designing the simulation in the Lumerical Finite Difference Time Domain (FDTD) solver software. The schematic of the simulated polarization rotator with a deeper-etch ridge waveguide structure on the left side and a one-sided tapered waveguide structure on the right side is shown in Figure 4.1.

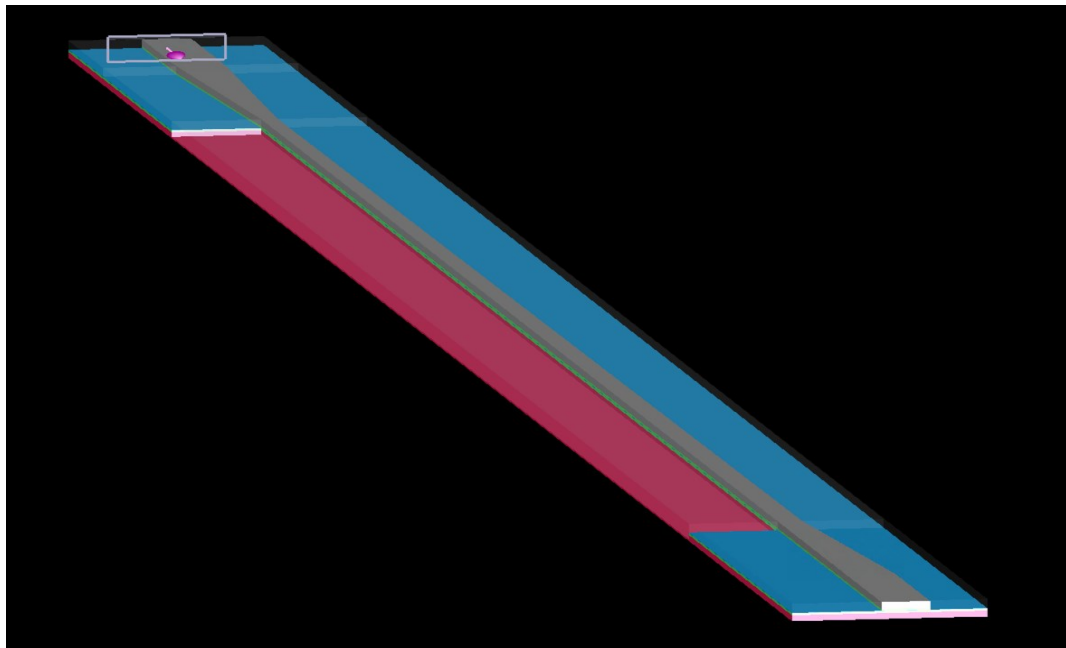


Figure 4.1 The schematic of the designed polarization rotator using InP/InGaAsP

The simulation technique here is to evolve the  $TE_0$  or ( $TM_0$ ) mode at the input port of the ridge waveguide with higher propagation constant. As shown in Figure 4.3 at the start of the rotator length ( $L$ ), the width of the waveguide ( $w_1$ ) is narrow and linearly increased on one side of the structure, the one-sided-tapered structure ( $w_2$ ). The polarization state of the propagating modes is then tilted concerning the length by introducing the asymmetry to the ridge waveguide via a deeper-etch structure on the opposite side of the tapered. The straight deeper-etch ridge structure is present throughout the polarization converter length which helps to tilt the polarization state to about  $45^\circ$ .

These tilted modes present along the converter length are hybridized modes neither pure  $TE_0$  nor  $TM_0$  which get converted to pure  $TE_0$  ( $TM_0$ ) at the output of the polarization rotator as will be explained in the section 5.2.3. The input and the output port of this polarization rotator are based on the standard ridge waveguide dimensions supporting the fundamental TE and TM mode as defined at the foundries and reference material [58]. Designing the single-mode input and output waveguide will allow us to limit the unwanted higher-order modes propagating through the ports. The straight deeper-etch structure is preferred to achieve fabrication simplicity.

Due to the weak vertical confinement which occurs because of the minimal refractive index contrast in InP/InGaAsP material, the upper cladding selected is double the thickness of the core to achieve low-loss optical coupling. Also, an etch-stop layer is included and is a crucial part of the design where the core thickness is protected while fabricating the design. The etch stop layer thickness can be selected to be from  $0.02\mu\text{m}$  to  $0.03\mu\text{m}$  [58]. The selected etch stop layer material has been studied from the recently published research. Although, InP can be used as an etch stop layer [58] [59] [60] [61] [62] simulation study undertaken to select InP or InAlAs for etch stop layer is presented in section 5.1.

#### 4.2.2 Design parameters

Below in Figure 4.2, Figure 4.3 and Table 3.1, the annotations, definition, dimensions, material layer characteristics, and parameters of the deeper-etch ridge waveguide are explained at the cross-section of about half the rotator length. The cross-section figure is derived from the refractive index monitors placed at the half-length of the polarization rotator.

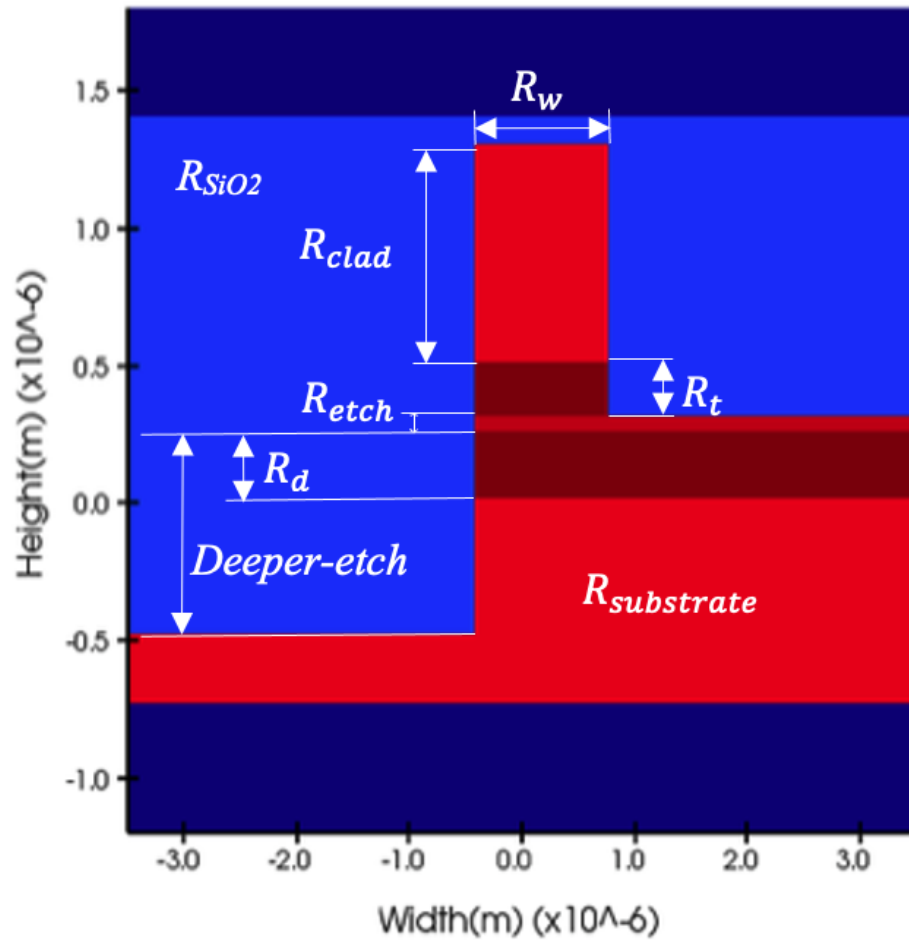


Figure 4.2 The cross-section view of the deeper-etch ridge waveguide

In this thesis work, various combinations of the parameters are studied, and the results are explained in 0.

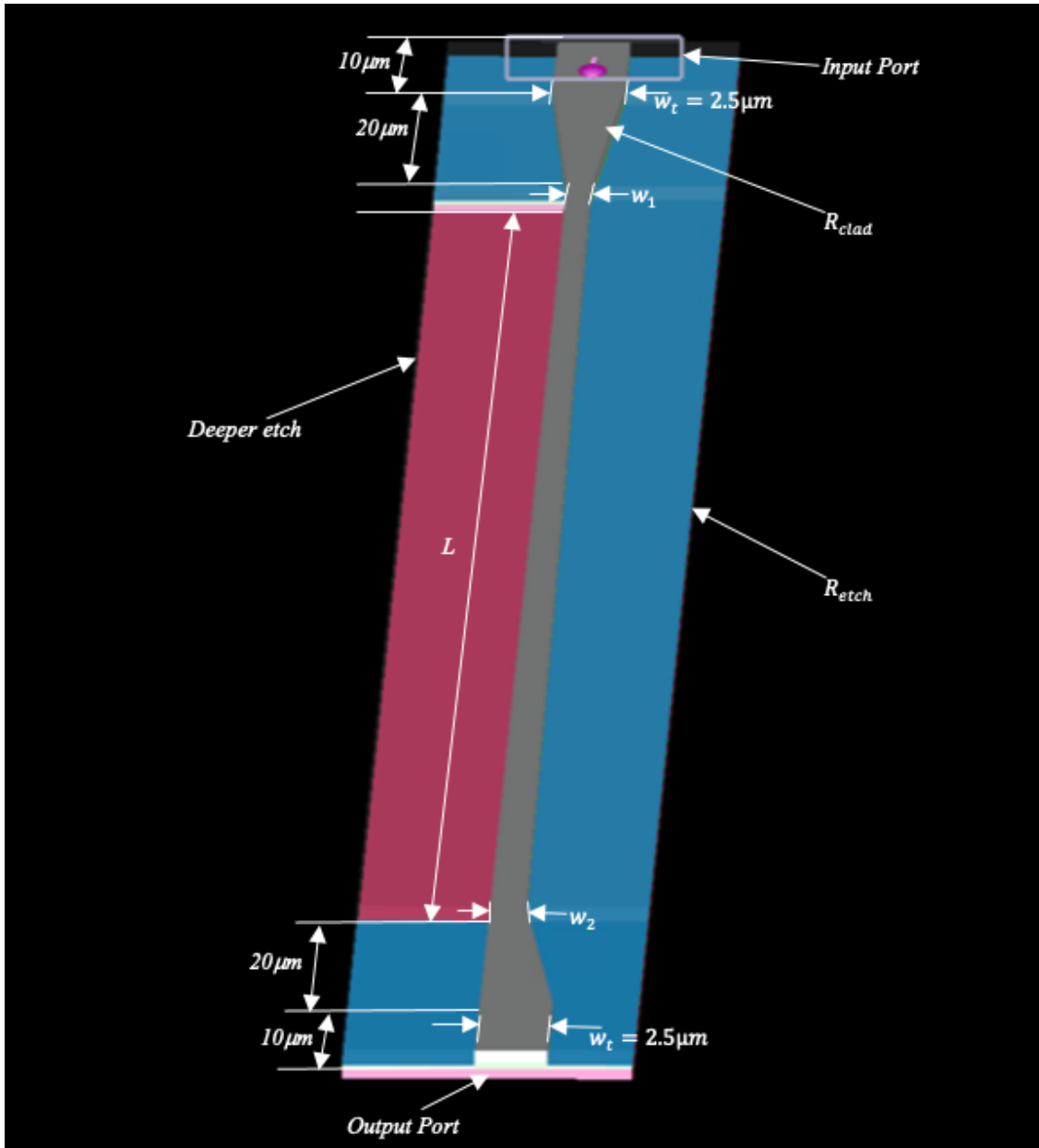


Figure 4.3 The detailed annotation of the polarization rotator

As seen in Figure 4.3 the input and the output port have  $10\mu m$  long ridge waveguides and a tapered interface of  $20\mu m$  long for smooth coupling for the input and output port. These waveguide ports can be designed as a single-mode waveguide as per the application and integration with any optical chip such as SOA, MZ, etc. A layer of  $\text{SiO}_2$  is used to cover the entire polarization rotator for passivation purposes only. The opacity for the  $\text{SiO}_2$  layer in the simulation design is set at 10%

for simplicity. Note that the  $w_2$  is tapered at the non-etched side of the device. The material and layer definitions are outlined in Table 4.1.

Material	Layer	Annotation	Refractive index at 1550nm
InP	Substrate	$R_{substrate}$	3.16
InP	Upper clad	$R_{clad}$	3.16
InGaAsP	Core	$R_d$	3.40
InGaAsP	Ridge	$R_w$ = Ridge width ( $w_1, w_2$ ) $R_t$ = Ridge thickness	3.40
InAlAs	Etch-stop layer	$R_{etch}$	3.25
SiO <sub>2</sub>	Over-all cover (passivation)	$R_{SiO_2}$	1.45

Table 4.1 The definition of the parameters

Table 4.1 explains the annotations that are used for the simulated polarization rotator throughout the study. Here the selected parameters are  $w_1=0.85\mu\text{m}$ ,  $w_2=1.15\mu\text{m}$ ,  $w_t=2.5\mu\text{m}$ ,  $R_{substrate}=0.7\mu\text{m}$ ,  $R_d=0.26\mu\text{m}$ ,  $R_{etch}=0.03\mu\text{m}$ ,  $R_t=0.21\mu\text{m}$ ,  $R_{clad}=0.85\mu\text{m}$ ,  $deeper-etch=0.5\mu\text{m}$ ,  $L=200\mu\text{m}$ .

#### 4.2.3 Introduction to Finite Difference Time Domain (FDTD) 3D Solver

FDTD stands for the finite-difference time-domain method. The modeling of the polarization rotator is performed using the Finite Difference Time Domain (FDTD). The reason behind choosing the FDTD solver is because of its capability of solving Maxwell's equation in complex geometries. The solver allows the user to simulate the device in 2D and 3D geometries. The solver

acts as a virtual test bench for solving all types of problems in electromagnetics and photonics. Moreover, the software helped this thesis work in numerous ways by providing a wide range of results calculated such as effective index ( $n_{eff}$ ), transmission ( $T$ ), reflection of light ( $R$ ), mode field profile, and Eigenmode calculations at different wavelengths and conversion efficiency ( $CE$ ). The features such as polarized light source, plotting of graphs and mode profile, etc., were beneficial to support the propagation of a mode and to study the behavior of the polarization conversion at the output.

This solver is useful but is also time-consuming when simulating large device geometries such as the simulation of the device studied in this thesis. The accuracy of the solver is acceptable compared to the other solver such as Eigen Mode Expansion (EME) solver or Var-FDTD solver where the 3D geometry is collapsed into the 2D geometry. The results are verified by re-simulating with the EME-solver as well. Figure 4.4 is a glimpse of the FDTD solver window.

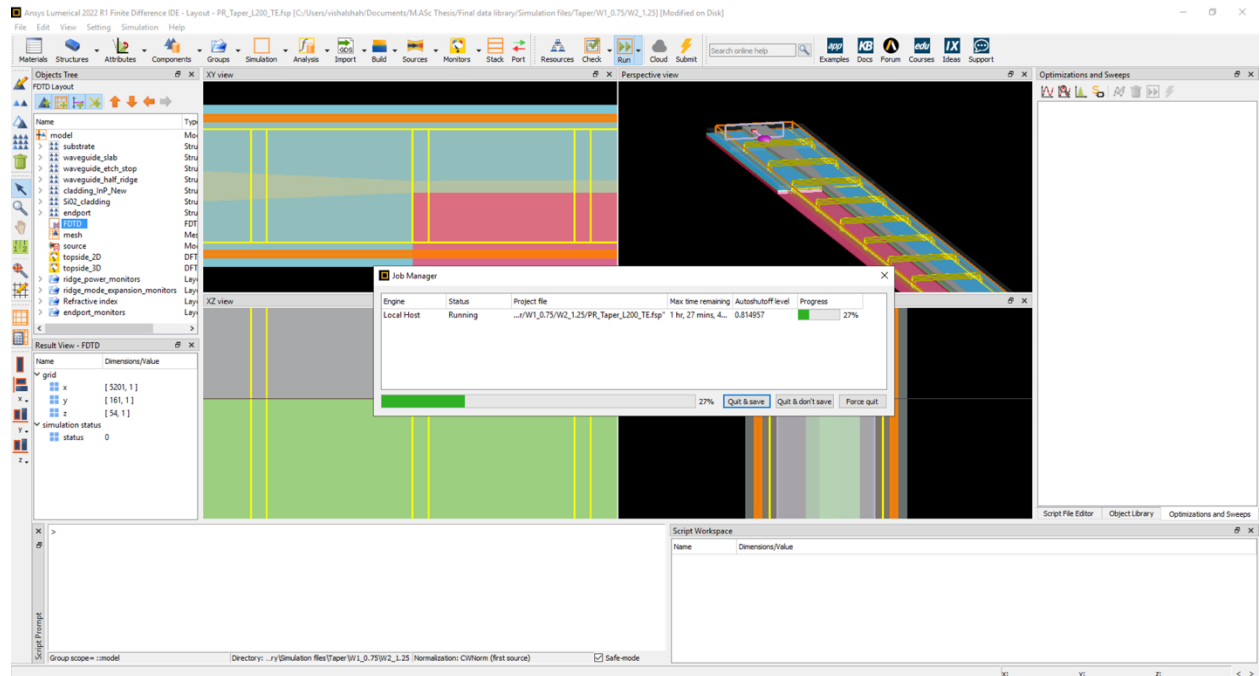


Figure 4.4 The Lumerical-FDTD solver window

To simulate and design the device for this thesis study, there were some basic experimental simulations carried out to understand the operations and the functions of the software. As the geometry of the designed and simulated device is complex and some of the parameter extraction is challenging, the basic learning and tutorials were carefully performed. The tutorials from Lumerical university were highly informative to achieve and extract those simulated results. Below is one of the examples of the elementary simulations shown in Figure 4.5, Figure 4.6 and Figure 4.7 to achieve confidence in extracted results.

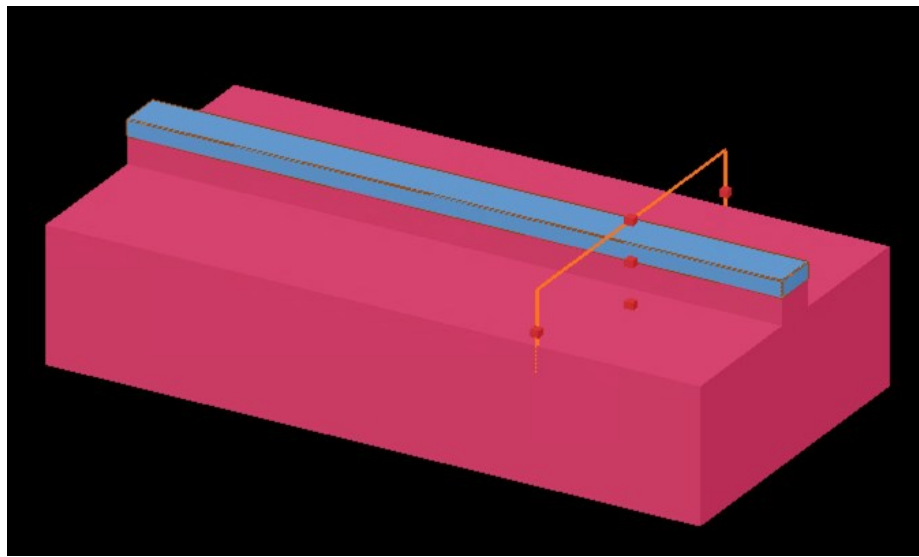


Figure 4.5 The Rib waveguide structure for mesh and simulation region convergence test

Figure 4.5 is a rib waveguide structure simulated to obtain the effective refractive index ( $n_{eff}$ ) of the fundamental TE mode. Here the main goal is to calibrate and standardize the simulation platform to avoid any variation in output. The mesh setting and the solver region play an important factor in the repeatability of the simulation results. The convergence test should be performed for the mesh setting so that if the mesh size is changed furthermore the output of the device remains unchanged. As noticed in Figure 4.6, the sweep of mesh size is carried out to understand the effect on the  $n_{eff}$  of the fundamental TE mode.

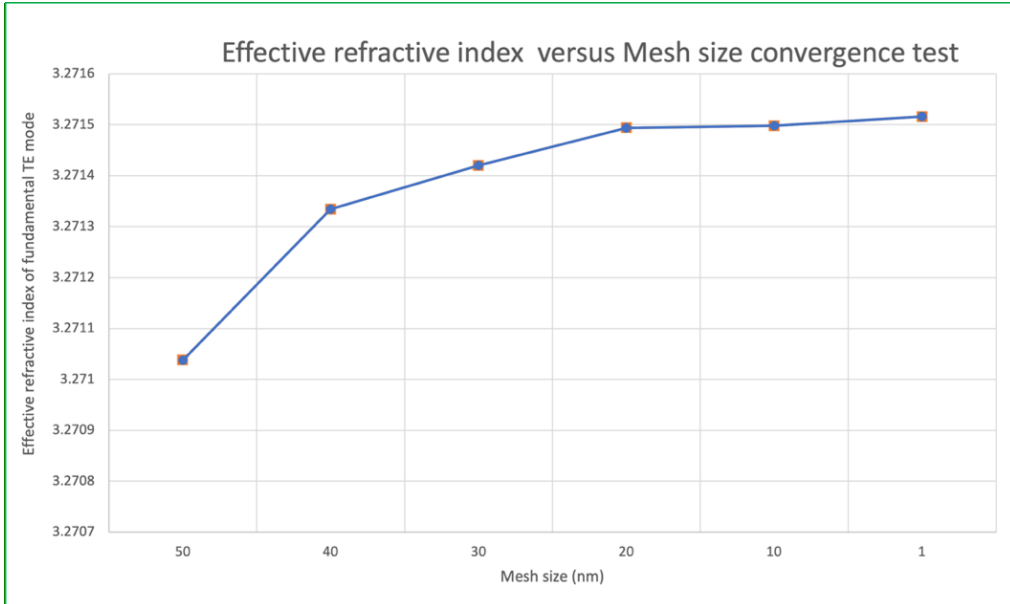


Figure 4.6 Example of the performed Mesh region convergence test

When the mesh size is 50nm the  $n_{eff}$  is  $\sim 3.271$  and when the mesh size is reduced to 20nm the  $n_{eff}$  changes to  $\sim 3.2715$ . Furthermore, reducing the mesh size keeps the resulted value to be  $\sim 3.2715$ . This explains the importance of the convergence test and the platform calibration for obtaining reliable results.

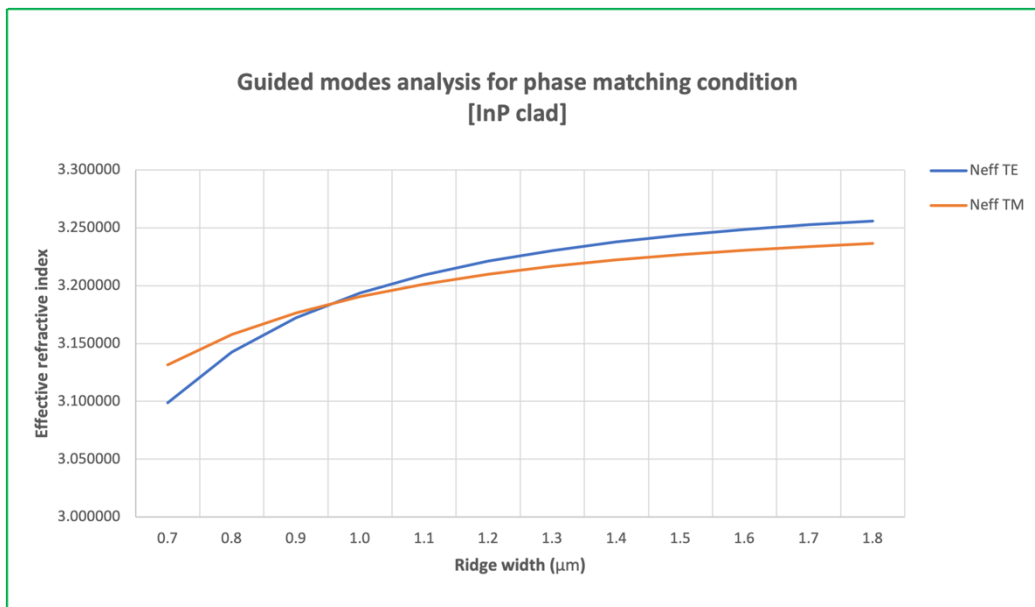


Figure 4.7 Extracting sweep parameters for different ridge widths

These experiments are carried out to commission the software setup to avoid any misleading results as the 3D simulation of the designed polarization rotator requires tremendous time and system memory.

#### 4.2.4 Structure geometry setup

The structure is created in the FDTD solver, where each layer of the device is grouped into a separate structure group for the ease of changing the parameter if needed.

Objects Tree	
FDTD Analysis	
Name	Type
model	Model
substrate	Structure Group
substrate_slab	Rectangle
substrate_input	Rectangle
substrate_etch	Rectangle
waveguide_slab	Structure Group
waveguide_input	Rectangle
waveguide_etch	Rectangle
waveguide_etch_stop	Structure Group
waveguide_input	Rectangle
waveguide_etch	Rectangle
waveguide_half_ridge	Structure Group
waveguide_input	Rectangle
taper_input	Polygon
waveguide_etch_oneside_taper	Polygon
cladding_InP_New	Structure Group
cladding_input	Rectangle
cladding_taper_input	Polygon
waveguide_etch_oneside_taper	Polygon
SiO2_cladding	Structure Group
cladding_input_right	Rectangle
cladding_input_left	Rectangle
cladding_taper_left	Polygon
cladding_taper_right	Polygon
cladding_etch_oneside_taper_Left	Polygon
cladding_etch_below	Rectangle
cladding_top	Rectangle
endpoint	Structure Group
substrate_output	Rectangle
waveguide_output	Rectangle
etch_Layer_waveguide_output	Rectangle
taper_output	Polygon
waveguide_output	Rectangle
cladding_taper_output1.25_2.5	Polygon
cladding_waveguide_output	Rectangle
cladding_output_right_SiO2	Rectangle
cladding_output_left_SiO2	Rectangle
cladding_output_taper_left	Polygon
cladding_output_taper_right	Polygon

Figure 4.8 Structure group of the designed polarization rotator

Here both script and GUI interface has been used as per the requirement of the simulation and data extraction requirements. The group tree window of the designed device is shown in Figure 4.8. The naming of the layers is for simplicity purposes and to remember when optimizing the device. Each layer is created using several different available structure shapes and assigning the geometries accordingly as per the details in section 4.2.2. The material properties are assigned from the in-built material library at the same time when creating the geometries for each layer. Some material compositions aren't available in the in-built material library, so the refractive index is sourced from the available books and online resources [58] [63]. In this case, the material library for InGaAsP was created for a design wavelength of  $1.55\mu\text{m}$ . Note that the refractive index library should be created for different wavelengths according to the interest in the frequency sweep results for some parameters such as polarization conversion efficiency (PCE) over C-band.

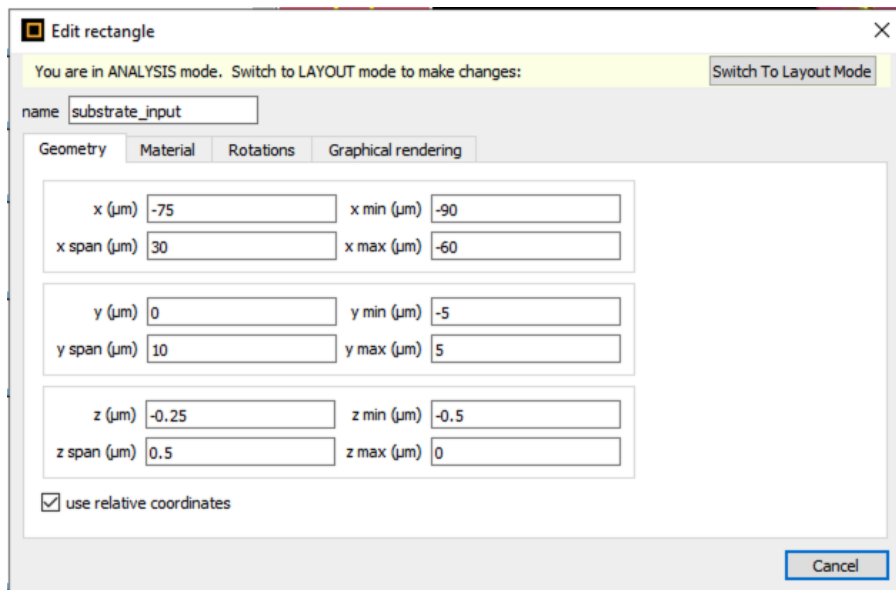


Figure 4.9 The illustration of geometry window for a structure layer

Figure 4.9 is an illustration of the geometry window of the layer structure where the dimensions are assigned as per the structure definition. In this simulation, since the study is carried out using different dimensions, the entire structure is divided into separate modules. It helps in optimizing

the device in terms of length, width, thickness, rotation, etc. This does not compromise the integrity of the design.

#### 4.2.5 The FDTD solver region and mesh settings

The FDTD simulation region is where the simulation geometry, simulation time, mesh settings, and boundary conditions are specified. Any objects that are not inside the simulation region will not be included in the simulation. Mesh override regions can also be added. They are used to specify a finer mesh in regions where a higher resolution is needed, for example, to resolve small geometric features. The solver region shown in Figure 4.10 is convergence tested and covers the entire interested simulation region. The mesh is set up in the waveguide and deeper-etch section which covers the entire device length for higher accuracy of the extracted results. This is the example of the solver region and mesh setup highlighted in orange.

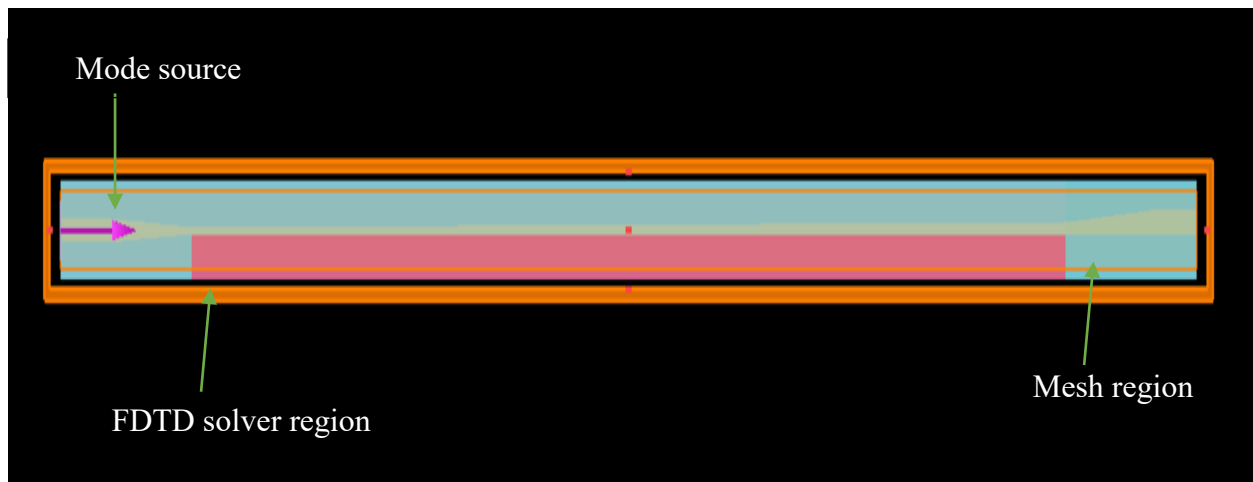


Figure 4.10 The FDTD solver region and Mesh region setup

As the device length ranges from  $150\mu\text{m}$  to  $250\mu\text{m}$ , the simulation time required for this device is comparatively higher than the devices with a smaller footprint (for example a directional coupler of length  $\sim 50\mu\text{m}-70\mu\text{m}$ ) as the propagation of the mode is calculated using 3D geometry. The

mesh size for this region is selected to be  $0.01\mu\text{m}$  with the confidence obtained from the mesh convergence testing in 4.2.3.

#### 4.2.6 Input mode source and monitors setup

The sources are used to inject light into the simulation region. Several sources are available such as Dipole, Gaussian, Plane-wave, Total-field scattered-field, and Mode sources to inject different field profiles as shown in Figure 4.11. The user can also import a custom spatial field profile with a specific dataset format if needed. The main interest of this study is to convert the polarization state from fundamental TE to fundamental TM or vice-versa. Therefore, a mode source is used to inject either the fundamental TE or fundamental TM mode. For this study, the source is placed at the forward X-axis near the input port of the device highlighted in magenta color as shown in Figure 4.10. The placement of the source is not necessarily to be at the forward X-axis but can also be placed at the output port in a backward X-axis direction depending on the application.

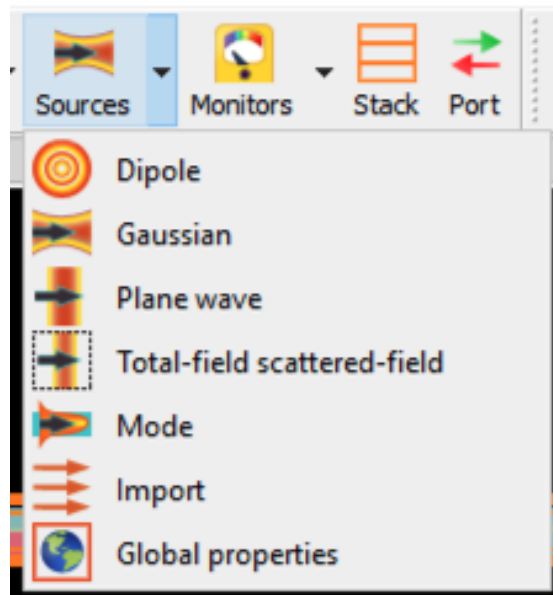


Figure 4.11 Optical sources in 3D-FDTD solver

The monitors play a key role in the simulation of any device and are used to record simulation results. The list of available monitors to record the data is shown in Figure 4.12.

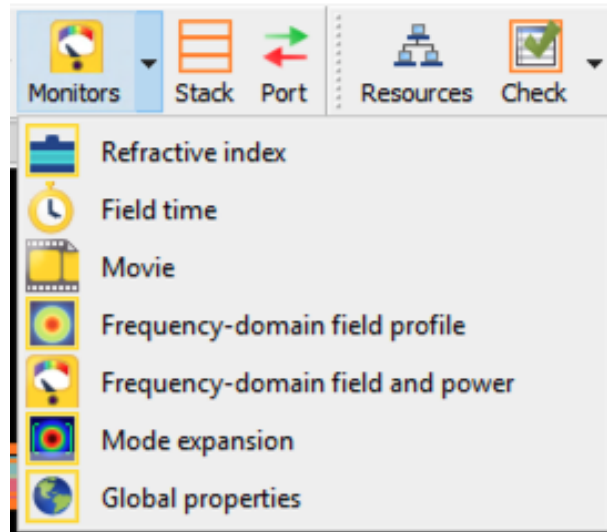


Figure 4.12 The monitors for recording the simulation data

The monitors mainly used in this simulation study are the index monitor; which returns the refractive index profile over space, the frequency domain power and profile monitors; which return the steady-state transmission spectrum and spatial field profiles, and the mode expansion monitor and ports are used to analyze the amount of power traveling in a specific model of a waveguide or fiber. The polarization conversion efficiency calculation is highly dependent on the mode expansion calculated by the frequency domain power monitor.

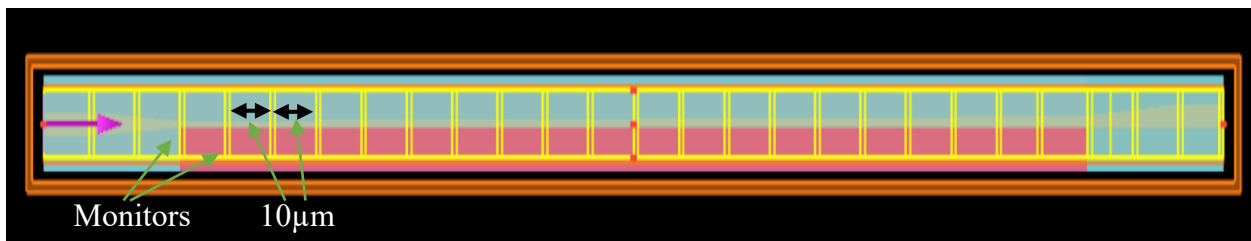


Figure 4.13 Placement of the 78 monitors to obtain accurate data points

In Figure 4.13, the monitors are highlighted in Yellow with double vertical lines. The frequency-domain field monitors, the mode expansion monitors, and the refractive index monitors are placed at the interval of  $10\mu\text{m}$  from the input port throughout the device until the output port. The mode expansion monitors, and the refractive index monitors overlap to keep the data point, accurate relative, to the position. The mode expansion monitors must be placed before the frequency domain field monitors as the calculation of transmission power ( $T$ ) is sampled between the position of both the monitors. Here, the placement of the mode expansion monitor is staggered by a  $1\mu\text{m}$  difference relative to the position of the frequency domain field monitor. The monitors are placed as 2D X-normal which is the cross-section of the device. The placement of the monitors at short intervals provides supplementary data points for extracting results. The more data points provide accurate simulation results.

## Chapter 5 Results and Discussion

To analyze the design various simulation tests were performed. All the simulations are based on the settings used when the convergence test of the software was completed for a basic setup. This includes mesh size setting, boundary condition, simulation time, mode source, solver region, power monitors, mode expansion monitors, and refractive index monitors. As the structure of the device is deeper etch and is asymmetric on both input and output regions, the geometry setup is a challenge while studying the device for various lengths ( $L$ ). The commissioning of the software settings discussed in 4.2.4 assures us that the variation in results on each simulation test was minimal.

### 5.1 The analysis of the etch-stop layer ( $R_{etch}$ )

This study was to investigate the selection for the etch-stop layer for the InGaAsP core ( $R_d$ ). If the core ( $R_d$ ) can be achieved to be as close to the desired thickness of  $0.26\mu\text{m}$  after the etching of the ridge waveguide, the mode confinement factor would not be disturbed. If the core thickness ( $R_d$ ) changes, the output result of polarization conversion efficiency is subject to change. The literature study that was conducted for this section helped narrow down the option for the  $R_{etch}$  layer to select from two-material compositions for the InGaAsP core [58] [64]. The two material options investigated for this design were InP and InAlAs with similar thickness  $R_{etch} = 0.03\mu\text{m}$ . The reactive-ion-etching (RIE) process is selected to etch the deeper-etch section on the ridge waveguide for any selected etch-stop layer if the device is to be fabricated in a future study. It has been suggested in previous research studies carried out by other researchers that increasing the selectivity of the InGaAsP layers relative to InP can be achieved by increasing the As concentration [58]. On the other hand, InAlAs offer isotropic etches and superior selectivity ( $>4,000$ ) compared to InP against InGaAsP [65]. The simulated experiment was carried out to understand the effect

on modal confinement using InP or InAlAs as an etch-stop layer in between the InGaAsP core and ridge waveguide. Figure 5.1 and Figure 5.2, plot the resulted data where the effective refractive index is plotted against the waveguide width( $w$ ) as the design of the ridge waveguide is tapered on one side for both the material and etch-stop layer simultaneously. There was a ~1% difference in the mode confinement factor for InP versus InAlAs. Thus, due to the advantage of high etching selectivity against InGaAsP and minimal mode confinement factor against InP, InAlAs was selected as an etch-stop layer.

The effective refractive index of the first two eigenmodes of a tapered ridge waveguide (etch stop layer- InP)		
Waveguide width( $w$ ) $\mu\text{m}$	$n_{\text{eff}}$ TE-like	$n_{\text{eff}}$ TM-like
0.75	3.181116	3.186878
0.85	3.196321	3.201151
0.95	3.209263	3.212905
1.05	3.222708	3.219524
1.15	3.231010	3.227465
1.25	3.237956	3.233713
1.35	3.243738	3.238780

Table 5.1 Etch-stop layer as InP

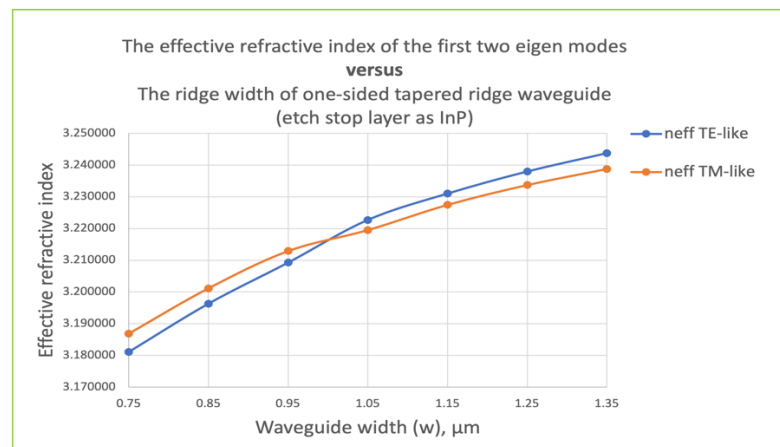


Figure 5.1 Influence of InP etch-stop

The effective refractive index of the first two eigenmodes of a tapered ridge waveguide (etch stop layer- InAlAs)		
Waveguide width( $w$ ) $\mu\text{m}$	$n_{\text{eff}}$ TE-like	$n_{\text{eff}}$ TM-like
0.75	3.184681	3.191124
0.85	3.200320	3.205670
0.95	3.213589	3.217455
1.05	3.227153	3.224149
1.15	3.235360	3.232303
1.25	3.242279	3.238651
1.35	3.248063	3.243764

Table 5.2 Etch-stop layer as InAlAs

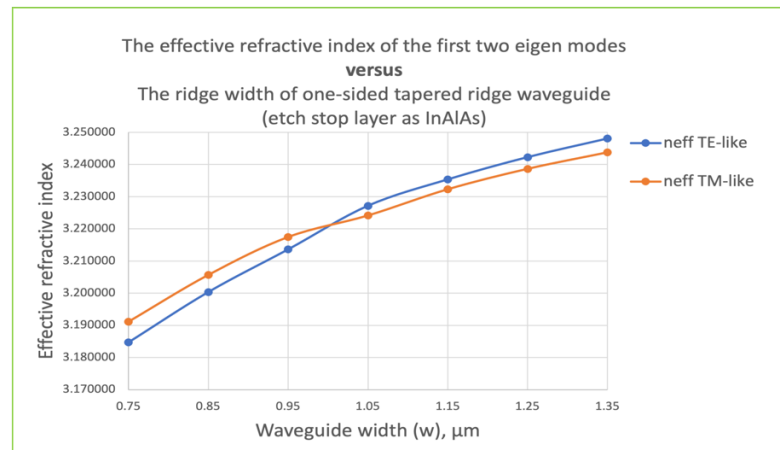


Figure 5.2 Influence of InAlAs etch-stop

## 5.2 Polarization conversion efficiency (PCE)

This study was conducted to analyze the conversion efficiency and to understand the optimization of the polarization converter length ( $L$ ). The results are cross-tested using the Eigen Mode Expansion solver to obtain confidence in extracted data.

### 5.2.1 Analyzing polarization conversion efficiency using a 3D-FDTD solver

As explained in section 4.2, this study aims to design a robust and compact structure against tolerance error.

Polarization conversion efficiency (PCE) versus Polarization converter length ( $L$ )			
Polarization converter Ridge Width ( $w_1, w_2$ ), $\mu\text{m}$	Simulation results Polarization Efficiency (PCE) $\text{TE}_0$ to $\text{TM}_0$ Normalized to 1		
	$L = 150\mu\text{m}$	$L = 200\mu\text{m}$	$L = 250\mu\text{m}$
$w_1=0.75\mu\text{m},$ $w_2=1.15\mu\text{m}$	0.67	0.80	0.42
$w_1=0.75\mu\text{m},$ $w_2=1.25\mu\text{m}$	0.80	0.90	0.66
$w_1=0.75\mu\text{m},$ $w_2=1.35\mu\text{m}$	0.60	0.91	0.84
$w_1=0.85\mu\text{m},$ $w_2=1.15\mu\text{m}$	0.70	0.97	0.73
$w_1=0.85\mu\text{m},$ $w_2=1.25\mu\text{m}$	0.65	0.96	0.86
$w_1=0.85\mu\text{m},$ $w_2=1.35\mu\text{m}$	0.54	0.86	0.87
$w_1=0.95\mu\text{m},$ $w_2=1.15\mu\text{m}$	0.63	0.98	0.85
$w_1=0.95\mu\text{m},$ $w_2=1.25\mu\text{m}$	0.53	0.84	0.77
$w_1=0.95\mu\text{m},$ $w_2=1.35\mu\text{m}$	0.44	0.68	0.67

Table 5.3 The study for analyzing Polarization Conversion Efficiency (PCE) against Polarization Converter ridge width ( $w_1, w_2$ ) and Polarization Converter Length ( $L$ )

Table 5.3 states various combinations of width ( $w_1$ ,  $w_2$ ) for the one-sided tapered ridge waveguide are studied against the combination of polarization converter length ( $L$ ). Note, that the dimensions for parameters such as  $R_{substrate}$ ,  $R_d$ ,  $R_{etch}$ ,  $R_t$ ,  $R_{clad}$ , and *deeper-etch* resulted from the literature review performed in Table 3.1. These dimensions are suggested at the fabrication level, proven, and are normally used at the foundries [58]. Here, we have  $R_{substrate}=0.7\mu\text{m}$ ,  $R_d=0.26\mu\text{m}$ ,  $R_{etch}=0.03\mu\text{m}$ ,  $R_t=0.21\mu\text{m}$ ,  $R_{clad}=0.85\mu\text{m}$ , *deeper-etch*= $0.5\mu\text{m}$ .

The idea here was to keep the ridge core thickness ( $R_d + R_{etch} + R_t$ ) constant at  $\sim 0.5\mu\text{m}$  [58]. Moreover, only a thin etch-stop layer ( $10\mu\text{m} \sim 30\mu\text{m}$ ) is required depending on the etching technique. Keeping at least one variable value constant helps this study to sweep other parameters such as ( $w_1$ ,  $w_2$ ,  $L$ , etc.). The thickness of the  $R_{clad}$  is selected to achieve low-loss vertical coupling and provides an option for future integration with any PIC components.

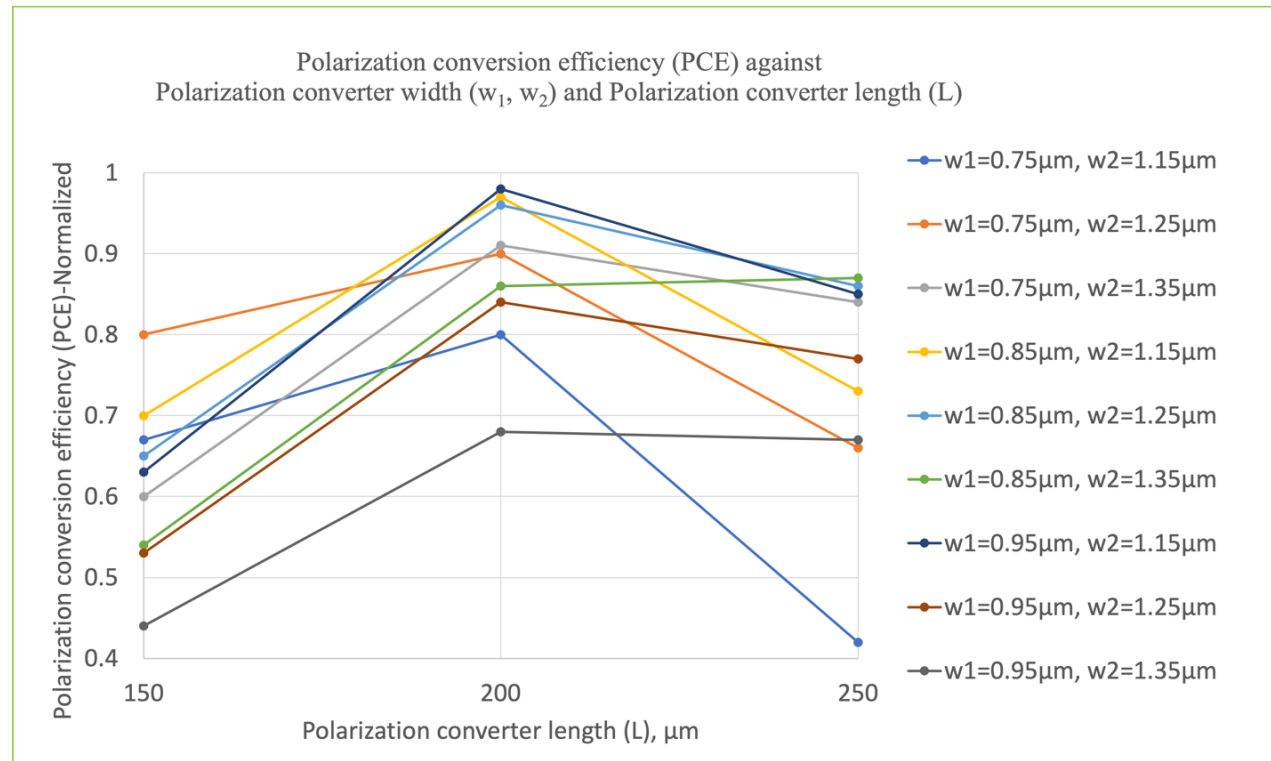


Figure 5.3 The study for analyzing Polarization Conversion Efficiency (PCE) against polarization converter ridge width ( $w_1$ ,  $w_2$ ) and polarization converter length ( $L$ )

It is observed in Table 5.3 and Figure 5.3 that after a certain polarization converter length ( $L$ ), there is a beat in conversion efficiency. In this setup when measuring the polarization conversion efficiency, the source at the input port is fundamental TE mode and the mode propagates along the forward x-axis. The asymmetry introduced (deeper-etch on the right side acting as a birefringent working on a mechanism of the half-wave plate with principal axis rotated by 45° and linear taper on the opposite side inducing adiabatic mode change) excites two eigenmodes which are hybrid modes neither pure  $TE_0$  nor  $TM_0$  as will be explained in section 5.2.3. These two eigenmodes recombine to vertically polarized,  $TM_0$  and vice versa. A detailed explanation of the hybridization and conversion of modes will be illustrated in Figure 5.11.

The expected outcome of this simulation study was to analyze and achieve higher polarization conversion efficiency at a specific converter length ( $L$ ) and the peak conversion was noticed close to  $L=200\mu\text{m}$  for nearly every width ( $w_1, w_2$ ). Here the study was limited to three data points for length ( $L$ ) and the reason was to limit the number of combinations (widths versus lengths) and manageable simulation time. Moreover, the peak values resulted around  $L=200\mu\text{m}$  and the decrease in the polarization conversion efficiency beyond  $L=200\mu\text{m}$  raised concerns about the performance of the device over length. The study to understand the same will be explained in section 5.2.4.

As we will select the dimensions for our main device structure simulation from this analysis, we confirm that dimensions ( $w_1=0.85\mu\text{m}, w_2=1.15\mu\text{m}, L=200\mu\text{m}$ ) are convincing to achieve better efficiency of the device and will provide a better tolerance value for any width variation during the fabrication process. Moreover, simulating longer device lengths is suggested to study the oscillation noticed in conversion efficiency after 200μm. Unfortunately, one of the limitations of the FDTD solver is to simulate large geometry requires huge memory requirements and simulation

time. In this case, the results can also be derived and cross-tested using the Eigen Mode Expansion (EME) solver which uses ports to inject light (mode of interest) and sweeps the entire length of the device to extract the S-parameter of the solver region. For purpose of this study, we suggest fabricating the polarization rotator with different converter lengths  $L$  (150 $\mu\text{m}$ , 200 $\mu\text{m}$ , 250 $\mu\text{m}$ , 500 $\mu\text{m}$ , 750 $\mu\text{m}$ , 1000 $\mu\text{m}$ , 1500 $\mu\text{m}$ ) to verify that the maximum efficiency length is at  $\sim 200\mu\text{m}$ .

### 5.2.2 Cross testing the results obtained using the EME solver

The design structure group with width ( $w_1=0.85\mu\text{m}$ ,  $w_2=1.15\mu\text{m}$ ,  $L=200\mu\text{m}$ ) is created in Eigen Mode Expansion (EME) solver.

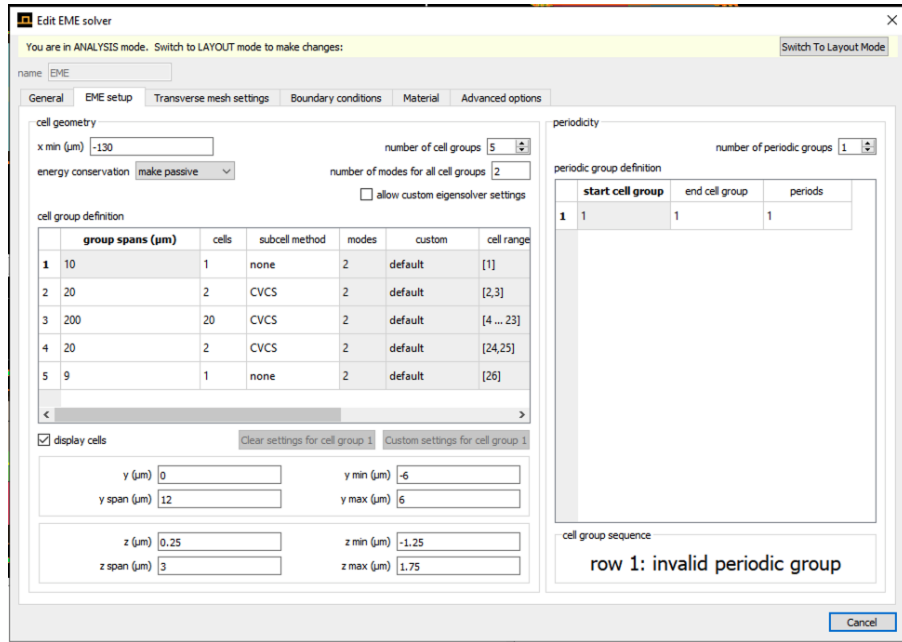


Figure 5.4 The EME solver setup window

The structure group is verified, and the solver region is set up to place cells throughout the entire geometry. The cells act as an individual block where the cell definition (number of cells placed) is made according to the group span ( $\mu\text{m}$ ) of the EME region. As this design is asymmetric, more cell placement is recommended. The reason behind placing more cells is to get many data points and helps in achieving accurate results where the structure is non-uniform for example a

taper waveguide structure. As seen in Figure 5.4, the group spans 2,3, and 4 include 2,20, and 2 cells respectively throughout its group span as it covers the taper and deeper-etch waveguide structure. The number of modes assigned to calculate is limited to two modes for each cell as shown in Figure 5.4. Note that port-1 is the input port and port-2 is the output port as shown in Figure 5.5. The port-2 is used to record the S-parameter using the EME-propagate function. The selected mode source opts as user-selected and the first mode (TE) of the input ridge waveguide is propagated in a forwarding X-axis direction.

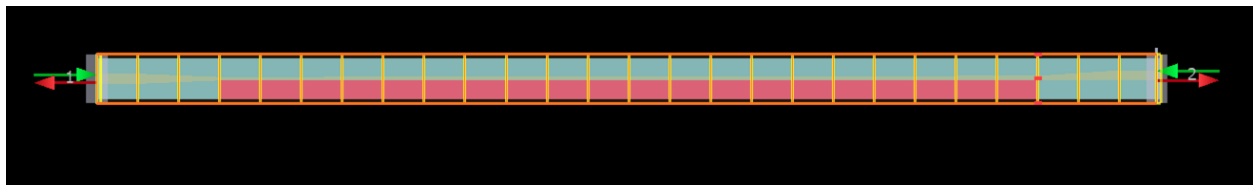


Figure 5.5 Input and output ports setup

The electric field profile of the input source is shown in Figure 5.6. After the simulation and the propagation sweep of the device, the following S-parameter (scattering parameter) matrix is obtained.

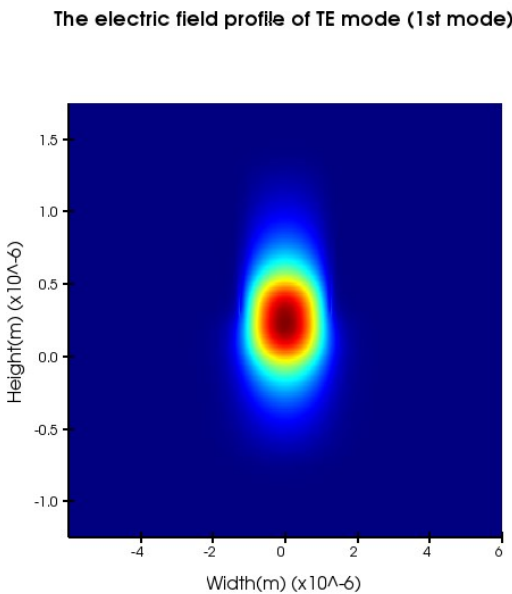


Figure 5.6 The electric field profile of the TE mode of the input ridge waveguide

S-matrix index mapping		
S-matrix index	Source mode	
1	port 1	mode 1
2	port 2	mode 1
3	port 2	mode 2

Figure 5.7 The S-parameter matrix index mapping from the EME solver

The S-parameter matrix index mapping table is shown in Figure 5.7. Here, the port-1 mode-1 is  $TE_0$ , port-2 mode-1 is  $TE_0$  and port-2 mode-2 is  $TM_0$ . Port-1 is the input port and port-2 is the output port. As the focus is to obtain the conversion efficiency from  $TE_0$  to  $TM_0$ , the only S-parameter to consider are  $S_{12}$ ,  $S_{21}$ , and  $S_{31}$ . The user S-matrix can be written as shown in Table 5.4.

User S-Matrix			
Input			
Output	1	2	3
	$S_{11}$	$S_{12}$	$S_{13}$
	$S_{21}$	$S_{22}$	$S_{23}$
	$S_{31}$	$S_{32}$	$S_{33}$

Table 5.4 The user S-parameter matrix

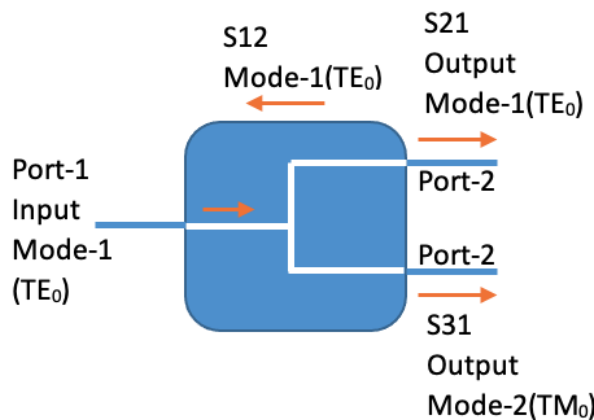
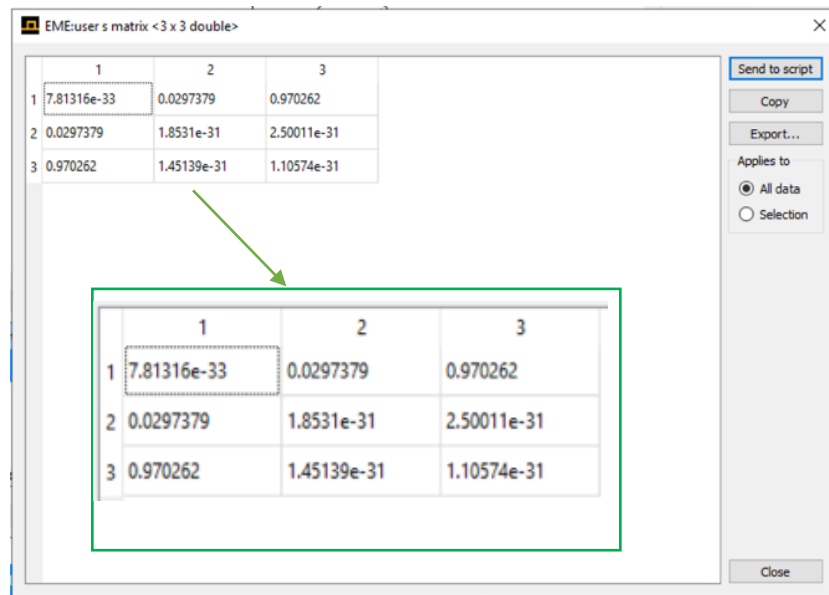


Figure 5.8 The block diagram explaining the S-parameter matrix.

Figure 5.8 is for a simplified explanation of the S-parameter matrix. The port-2 is a single output port, and the split is just to simplify the understanding. The annotation of the user S-parameter matrix is explained below:

- $S_{12}$ : Transmission coefficient for output port1, Mode1 from input port2, Mode1.
- $S_{21}$ : Transmission coefficient for output port2, Mode1 from input port1, Mode1.
- $S_{31}$ : Transmission coefficient for output port2, Mode2 from input port1, Mode1.

Here the input source is  $TE_0$  for the input port 1. The transmission coefficient for the output port-2 (mode-2,  $TM_0$ ) is extracted from the S-parameter matrix as shown in Figure 5.9. Column 1 row 3 is the normalized conversion efficiency value of  $TE_0$  to  $TM_0$ .



The screenshot shows a software window titled "EME:user s matrix <3 x 3 double>". It displays a 3x3 matrix of values:

	1	2	3
1	7.81316e-33	0.0297379	0.970262
2	0.0297379	1.8531e-31	2.50011e-31
3	0.970262	1.45139e-31	1.10574e-31

A green arrow points from the top matrix to the bottom matrix, highlighting the value 1.10574e-31 in the bottom matrix, which corresponds to the value 0.970262 in the top matrix.

Figure 5.9 The S-parameter matrix for polarization conversion efficiency from  $TE_0$  to  $TM_0$

Here we can conclude from Table 5.3 and Figure 5.9 that for the structure group with width ( $w_1=0.85\mu m$ ,  $w_2=1.15\mu m$ ,  $L=200\mu m$ ) the polarization conversion from  $TE_0$  to  $TM_0$  is 97% for both the solving method i.e., FDTD and EME solver.

The screenshot shows a MATLAB workspace window titled "EME:user s matrix <3 x 3 double>". The matrix contains the following values:

	1	2	3
1	1.80183e-32	0.970262	0.0297379
2	0.970262	1.43773e-31	4.09378e-32
3	0.0297379	1.78459e-32	8.28429e-32

A green arrow points from the original matrix to a submatrix highlighted with a green border. This submatrix is also a 3x3 matrix with the following values:

	1	2	3
1	1.80183e-32	0.970262	0.0297379
2	0.970262	1.43773e-31	4.09378e-32
3	0.0297379	1.78459e-32	8.28429e-32

Figure 5.10 The S-parameter matrix for  $\text{TM}_0$  to  $\text{TE}_0$

In Figure 5.10, the transmission coefficient for the output port-2 (mode-1,  $\text{TE}_0$ ) is extracted from the S-parameter matrix. Column 2 row 1 is the normalized conversion efficiency value of  $\text{TM}_0$  to  $\text{TE}_0$ , where the input source was  $\text{TM}_0$  (user select mode 2). The 97% conversion efficiency was noted for the same.

### 5.2.3 The State of polarization along the device length

The deeper-etch structure on the right side of the ridge waveguide creates an asymmetric waveguide geometry and operates as a birefringent medium with the principal axis rotated by  $45^\circ$  and is similar in principle to the half-wave plate. In addition, the linear taper on the opposite side creates adiabatic mode evolution which helps in retaining the flexibility tolerance of the device in terms of width ( $w_1, w_2$ ). Although the taper of the ridge waveguide is not symmetric on both sides there is still an effective refractive index change for the mode propagating from the narrow ridge waveguide ( $w_1$ ) towards the wide tapered ridge waveguide ( $w_2$ ) in the forward x-direction. The effective refractive index change is shown in Figure 5.2. Here, the core thickness  $Rd=0.26\mu\text{m}$  and the etch-stop layer thickness  $Retch=0.03\mu\text{m}$ .

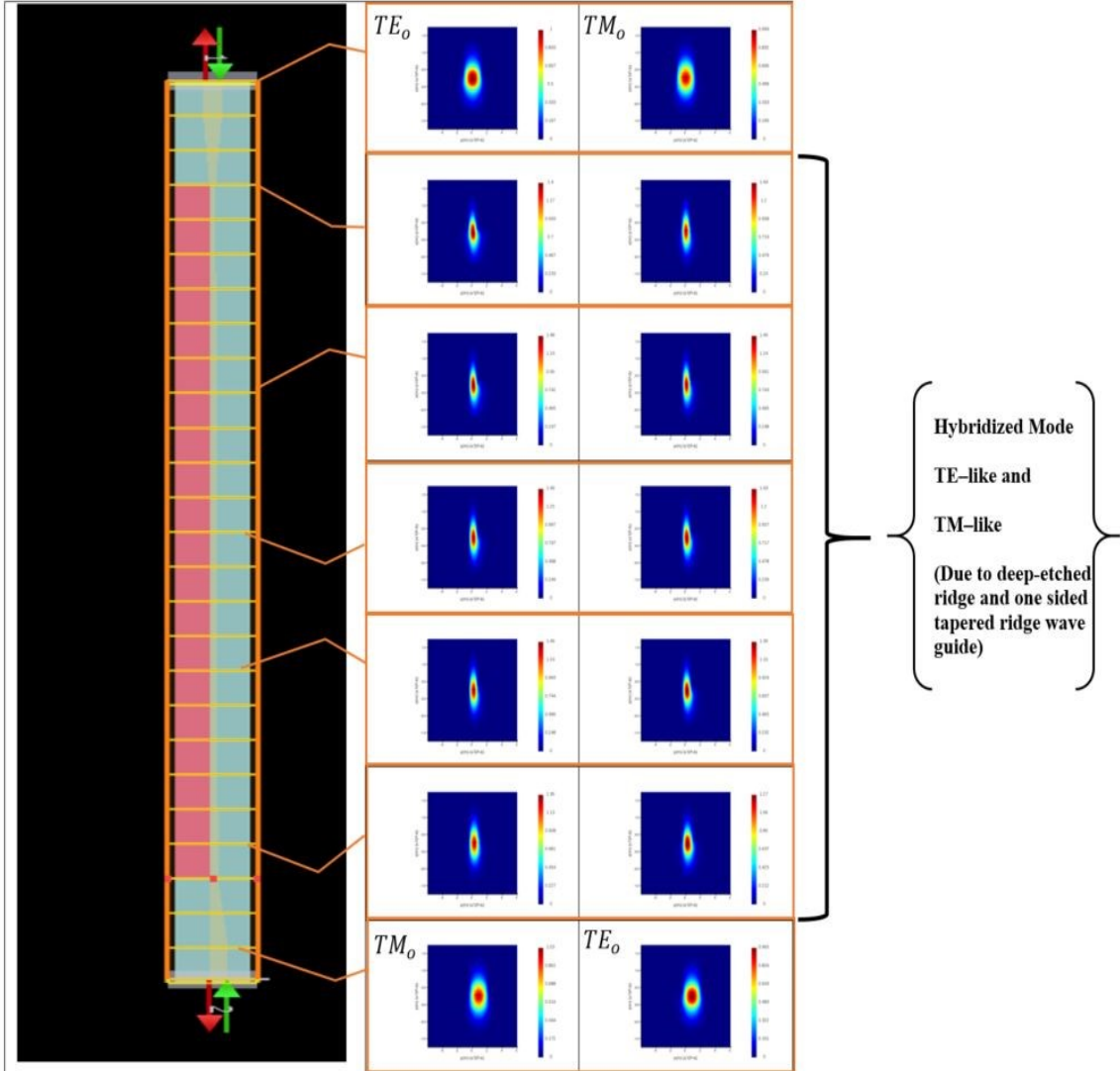
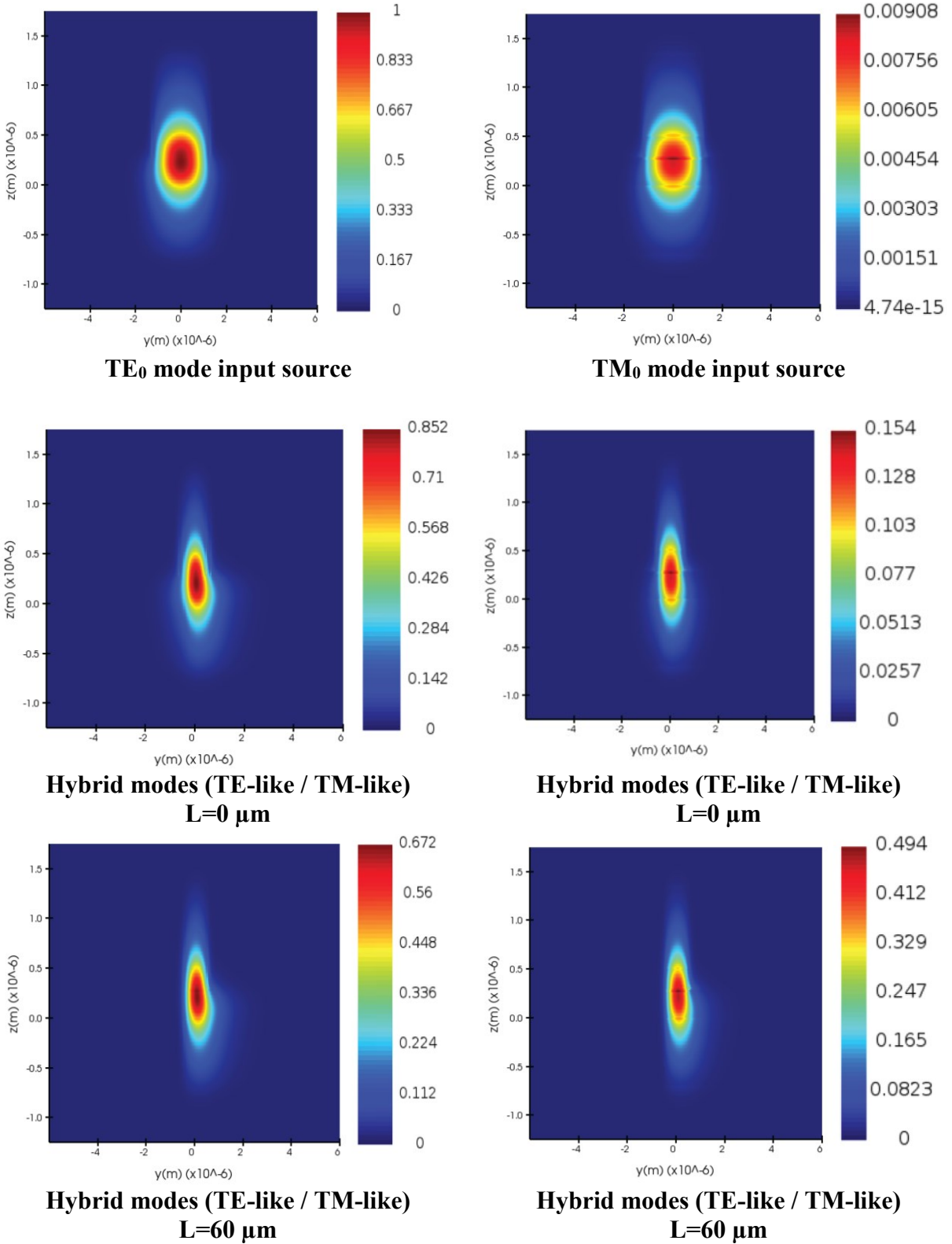


Figure 5.11 The polarization state of mode throughout the entire device length (see Figure 5.12)

The confirmation of the modal profile changing continuously from  $TE_0$  to  $TM_0$  and  $TM_0$  to  $TE_0$  is concluded over the entire length of the polarization converter length ( $L$ ) in Figure 5.11. As mentioned earlier, the one-sided tapered structure adds considerably larger tolerance to the device during fabrication compared to if the waveguide width was constant over the polarization converter length ( $L$ ). The ridge width variation affects the mode confinement factor and the study of this is stated in section 5.1. Please refer to Figure 5.12 for an enlarged version.



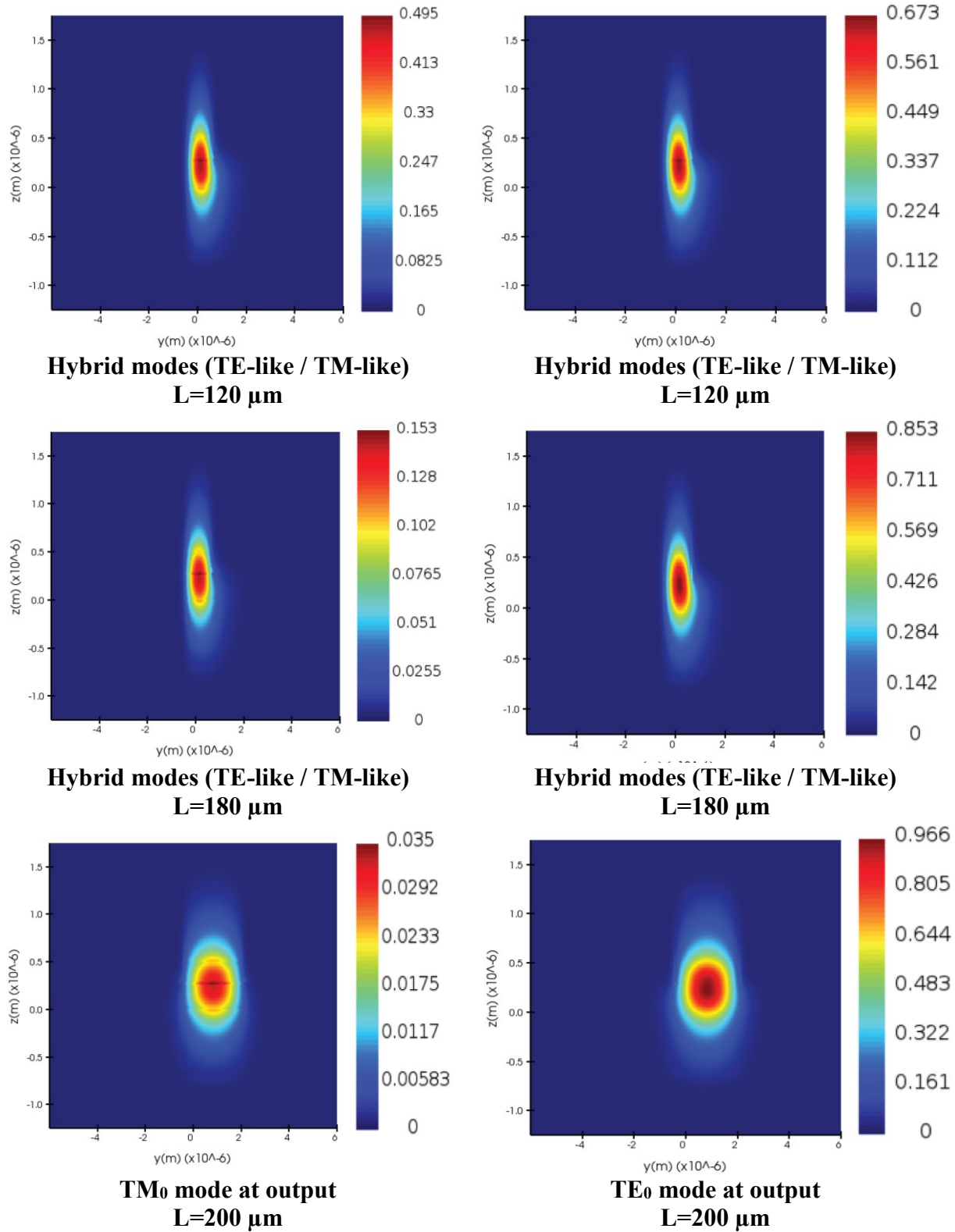


Figure 5.12 The polarization state of mode throughout the entire device length

The change in polarization state and its field profiles are extracted from the mode expansion monitors that are placed across the length of the polarization rotator. The placement pitch of  $10\mu\text{m}$  shown in Figure 4.13 helps acquire more data points over the length of the device. The characteristics such as  $n_{\text{eff}}$ , TE polarization fraction, the fraction of power transmission, and mode profiles can be obtained. The mode expansion monitors operate by expanding the supported mode field profile measured across the cross-section of the waveguide and are verified using the EME solver.

**The Z-normal view of the field profile**

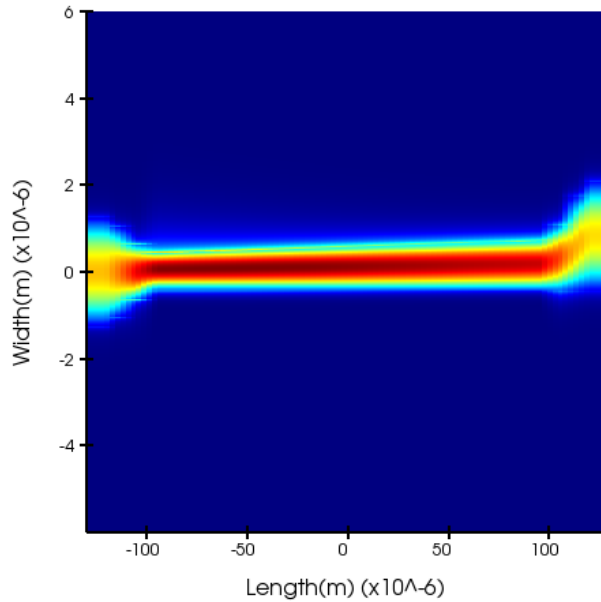


Figure 5.13 The electric field intensity profile of the polarization rotator- 2D Z-normal view

Figure 5.13 shows the field intensity when  $\text{TE}_0$  mode was propagating in forwarding x-direction. The mode field profile monitor was placed in the middle of the core thickness along the z-normal axis. Here the length (- $100\mu\text{m}$  to  $100\mu\text{m}$ ) is the entire converter length where the tilt of  $45^\circ$  and mode hybridization due to the deeper-etch tapered structure are noticed.

### 5.2.4 Variational study of polarization rotator over the length

It is important to understand the output repeatability of any device to achieve the highest efficiency when used in the field. We have noticed in section 5.2.1 that the conversion efficiency of the device decreases to a certain value after the converter length increased to  $L>200\mu\text{m}$ . We can evaluate the device over length by physically testing different device lengths on a test bench as mentioned in section 5.2.1 or simulate the device over length. Here we have created a propagation sweep over the converter length of the polarization rotator at a center wavelength of 1550nm.

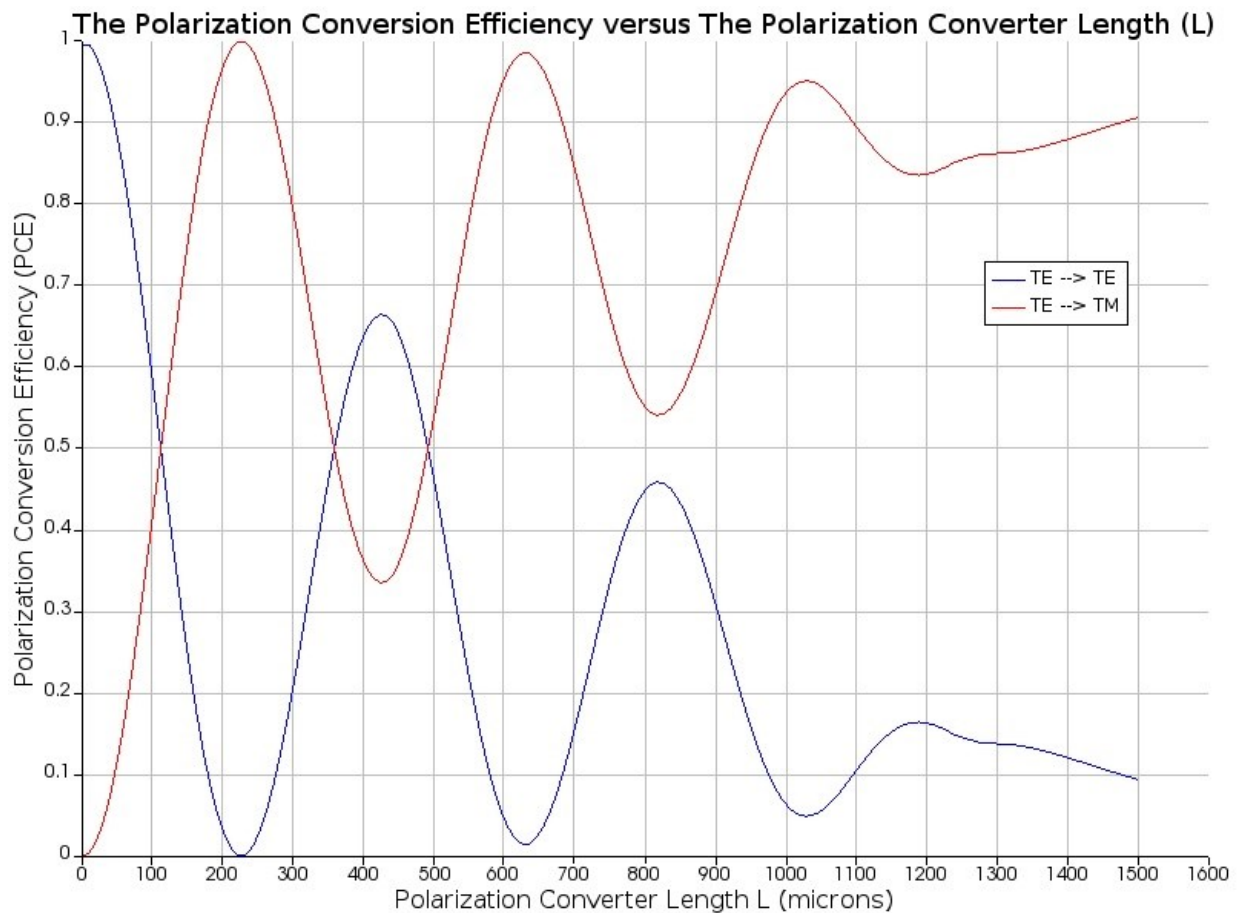


Figure 5.14 The Propagation EME Sweep versus Polarization Converter Length

Note that the 3D-FDTD simulations are very time-consuming when larger devices (such as the device of interest in this study) are to be simulated. Therefore, we have instead decided to use the

EME propagate function available in the EME solver. This helps us to reduce the time for simulations and create data points of more than 200 points for a converter length from  $0\mu\text{m}$  to  $1600\mu\text{m}$ . This simulation technique is the fastest when it comes to conducting length sweep studies. Figure 5.14 shows the resulting outcome of the polarization rotator device with width ( $w_1=0.85\mu\text{m}$ ,  $w_2=1.15\mu\text{m}$ ) and helps to illustrate the stability of the device over length. The oscillations in conversion efficiency are reduced and start to stabilize after  $1200\mu\text{m}$ . The device length is studied over polarization conversion efficiency. It is recommended to study the polarization conversion efficiency over time for different lengths of the device since the temperature of the device is at room temperature and is constant throughout the converter length sweep. If the temperature of the device is increased to about  $\sim 43^\circ\text{C}$  to  $45^\circ\text{C}$  (as an illustration value of temperature used at package level) there is the probability of observing the beats in conversion efficiency. This work can be continued and concluded in future studies.

### **5.2.5 The Polarization extinction ratio (PER)**

As stated in equations (2.22) and (2.23), the PER is simply the ratio of power held on the wanted axis of the polarization state over the power held on the unwanted axis of the polarization state (orthogonal polarization state). In this study, the ratio of power converted from TE to TM polarization state and vice versa gives us the value of PER of the device and is measured in decibels (dB). As shown below is the equation used to calculate the PER of the device and the fraction of power from TE  $\rightarrow$  TM is considered.

$$PER_{TE-TM} = 10 \log_{10} \frac{P_{TM}}{P_{TE}} \quad (5.1)$$

Here,  $P_{TM}$  is the fraction of power measured at the output port as TM polarization in the instance when the source was set to TE polarization and,  $P_{TE}$  is the fraction of power measured at the output

port measured as TE polarization (non-converted polarization power). The values of  $P_{TM}$  and  $P_{TE}$  are selected from Table 5.5 and verified in Table 5.3. Note that the values obtained in Table 5.3 are rounded to two decimal points compared to the values of Table 5.5 for simplicity. The polarization conversion efficiency for the device over C-band is shown in Figure 5.15.

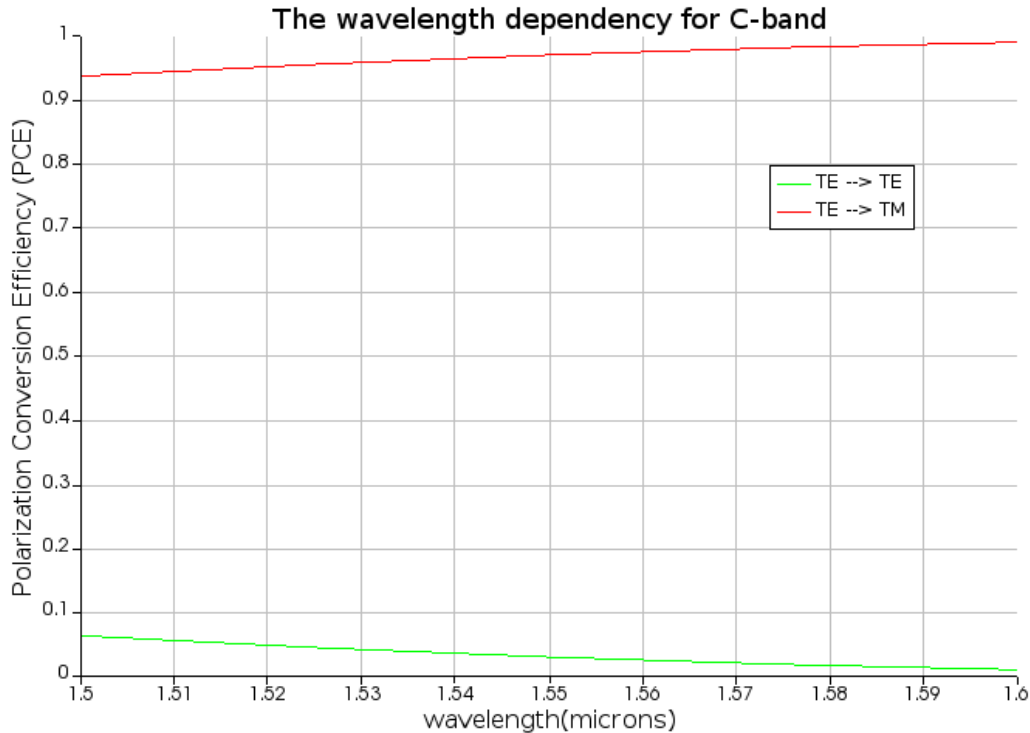


Figure 5.15 The Wavelength Dependency versus Polarization Conversion Efficiency for the entire C-band (1530nm to 1570nm)

Wavelength 1 ( $\mu\text{m}$ )	TE --> TM	TE --> TE	PER (dB)
1.500	0.937003	0.0629968	11.7
1.525	0.955437	0.0445632	13.3
1.550	0.970262	0.0297379	15.1
1.575	0.981721	0.0182785	17.3
1.600	0.990061	0.00993881	20

Table 5.5 The Polarization Extinction Ratio for wavelength 1550nm-1600nm

The device structure is same that resulted better polarization conversion efficiency compared to different lengths in section 5.2.1 and the parameters are  $R_{substrate}=0.7\mu\text{m}$ ,  $R_d=0.26\mu\text{m}$ ,

$R_{etch}=0.03\mu m$ ,  $R_t=0.21\mu m$ ,  $R_{clad}=0.85\mu m$ ,  $deeper-etch=0.5\mu m$ ,  $w_1=0.85\mu m$ ,  $w_2=1.15\mu m$ ,  $L=200\mu m$ . To calculate on-chip loss, coupling loss, insertion loss, polarization-dependent loss induced due to the characteristics like surface roughness, fabrication error, alignment error, material defects, residual slopes, etc., can be derived after placing the device under test. Moreover, the simulation design has a precise dimension with the material losses being zero, so the above characteristic is limited for the study. Since few of the research in similar interest but with a different design structure has stated the propagation loss to be 4.2 dB/mm [66]. The closest design with a half ridge waveguide structure with a ridge width of  $1.1\mu m$  and length of  $150\mu m$  has claimed the propagation loss to be  $0.57dB/mm$  [67]. Unfortunately, in this study the device design is asymmetric. It has a one-sided taper structure with an inserted etch-stop layer that may play a role in higher propagation loss. In addition, the input and output port of the device is designed for a smooth transition of fundamental mode into the polarization rotator. The dimension of these ports can be optimized after the test on a fabricated device. This possibly can be one of the ways to help reduce optical losses.

## Chapter 6 Fabrication Overview

The fabrication of the photonic-integrated-chip (PIC) can be done using various methods available in the industry for example dry etching, wet etching, etc. As device geometries are mostly at the microscopic or nanoscopic level it is hard to achieve the exact desired dimensions of the designed/simulated components. This affects the yield of the device in terms of operation and output results. Understanding the tolerance capability of the device plays a major role in achieving a high yield during fabrication. The fabrication yield also depends on the number of devices that can be fabricated on one single wafer where the dimension of the device plays a major role. According to knowledge gathered from professionals in the field of fabrication yield, it is acknowledged that process variation plays a huge factor in deciding the efficiency of the device. In this study, the device is passive and does not require any additional P-N metal layers but there are instances where the variation in metallization is observed at a different location on the same wafer with other elements fabricated at once.

Keeping that in focus, this study addresses some of the tolerance concerns that affect the device's performance. One of the major areas of focus is the polarization converter width ( $w_1, w_2$ ). The device performance is strongly based on the width of the ridge waveguide and to support that we have designed a one-sided tapered waveguide. The one-sided-tapered structure adds robustness to device performance in case of width variation and it is explained in section 5.2.3. Controlling the thickness of the core ( $R_d$ ) is also a challenge and to add robustness we have studied two different materials for the etch-stop layer which is explained in section 5.1. The etch-stop layer maintains the accuracy of the core ( $R_d$ ) during fabrication while performing the ridge definition.

As this thesis study is mainly focused on simulation modeling and results, the device can be fabricated to continue future work. In this section, a possible schematic of the fabrication process

is explained at a high level and available fabrication technologies which are suitable candidates to fabricate this device are briefly explained.

## 6.1 Overview of the fabrication process

The block diagram in Figure 6.1 illustrates the high-level visual context of the projected fabrication process. The process flow is divided into nine different steps [from (a)-(i)] which may vary according to the availability and selection of the fabrication method for the future work.

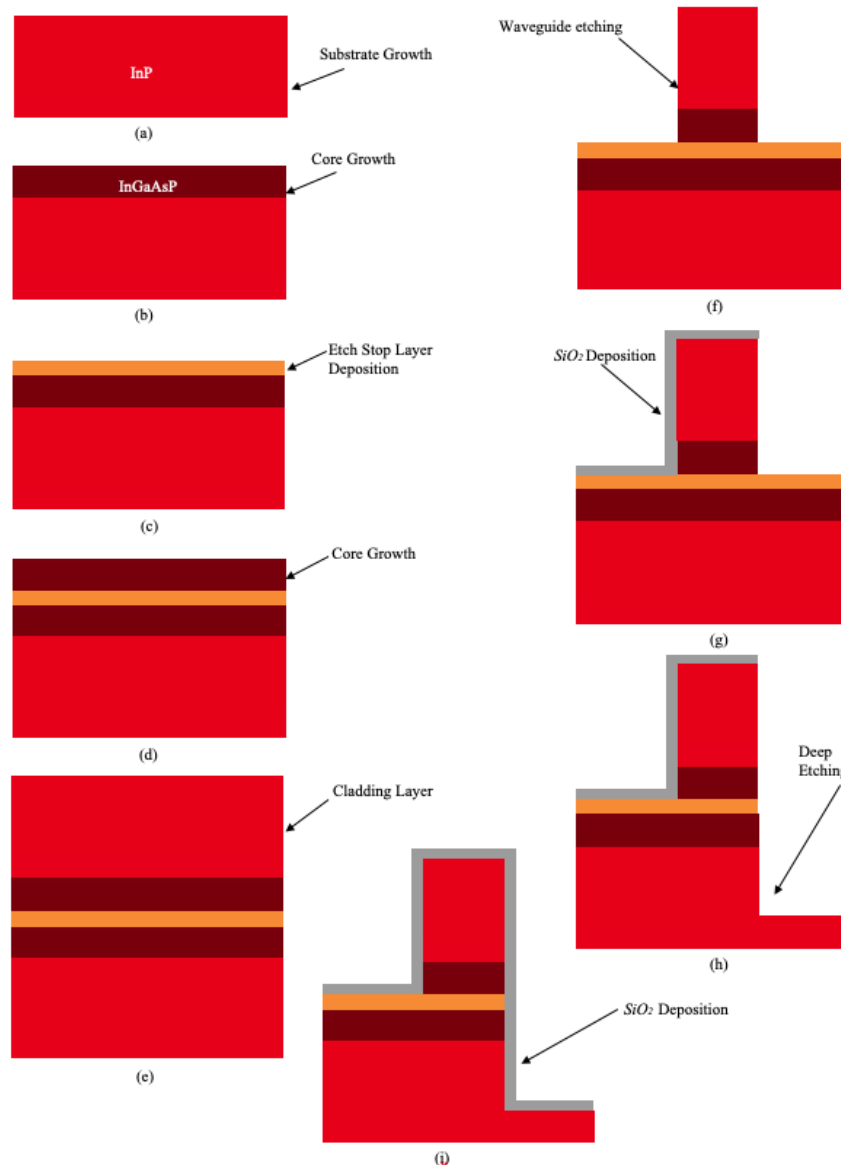


Figure 6.1 The block diagram for the fabrication process

The lattice-matched crystalline growth of one semiconductor over another is called epitaxy. To grow high-quality epitaxial layers, we need the correct solution composition for lattice matching. The possible composition of the quaternary alloys layer for this design on a substrate of InP (100)-oriented, Core =  $\text{In}_{0.66}\text{Ga}_{0.34}\text{As}_{0.9}\text{P}$ , Etch-stop layer =  $\text{In}_{0.52}\text{Al}_{0.48}\text{As}$  with refractive indices 3.167, 3.4, and 3.25 respectively at a center wavelength of  $1.55\mu\text{m}$  [68] [69].

- In block (a), the InP substrate growth is carried with the thickness  $R_{substrate} = 0.7\mu\text{m}$  followed by the next step.
- In block (b), the deposition of the core material (InGaAsP) is processed with the thickness of  $R_d = 0.26\mu\text{m}$ .
- The block (c) is the etch-stop layer  $R_{etch}$  introduced to achieve the desired stop when performing the ridge definition so that the thickness of the core remains under tight tolerance. Here the  $R_{etch}$  material is InAlAs, and it is selected because of its large selectivity over InGaAsP and to some extent the curiosity of using different etch-stop materials other than the conventional InP layer. The layer thickness for  $R_{etch}$  is kept at  $0.03\mu\text{m}$ .
- In block (d), the deposition of the core material (InGaAsP) is again processed with the thickness of  $R_t = 0.21\mu\text{m}$ . This layer is etched later for defining the ridge waveguide structure.
- The entire device is deposited with a thick layer of InP as upper cladding  $R_{clad}$  as shown in block (e) to achieve low loss and high vertical modal confinement. Here we have selected  $0.85\mu\text{m}$  as the thickness but  $0.5\mu\text{m}$  should be able to help achieve optimum vertical confinement.

- As shown in block (f), the etching of the ridge structure is carried out. In the definition of the one-side taper, the input and output ports are defined. Due to the introduction of the etch-stop layer, it is projected to achieve the nearest precise etch-stop as possible.
- In block (g), the  $\text{SiO}_2$  is deposited from an angle to cover one side of the ridge structure only. The other side of the ridge structure is not deposited with the  $\text{SiO}_2$  layer because of the etching needed for the deeper-etch section (converter length  $L$ ).
- The block (h) explains the deeper etch carried out on the opposite side from the deposited  $\text{SiO}_2$  layer. Here the depth of the etching is  $0.5\mu\text{m}$  it may vary according to the availability of precise etching technology at foundries.
- Finally, in block (i), the side of the deeper etch section is coated with the  $\text{SiO}_2$  layer for passivation only (to protect the surface from the surrounding environment). The dimension for the entire length of the device is based on the selection of the interest length. The other parameters are similar as explained in section 5.2.1.

# **Chapter 7 Conclusions and Future work**

In this chapter, the current thesis work and projected advances for future work have been summarized.

## **7.1 Conclusions**

The innovations in optical components have been increasing to adapt to the growth of the telecommunication industry. There have been many advances in terms of integrating the optical component to replace the bulk optics platform. The fiber optic networks required for communication use the most advanced coherent modulators where the expansion of the channels is very challenging. Even though at the package level the use of bulk optics components solves the issues related to polarization rotation that involves many different processes such as die-attach, and active alignment of lens/crystals. The incurred coupling loss is one of the factors where the integration of the polarization rotator can enhance the output of a PIC. Looking at the recent increase in the use of the online platform, advances that can help to enable the transport of more data across the optics channel would help to achieve a more affordable and faster communication path.

The polarization rotators based on silicon material have been promising but the integration with the InP-based PIC is still a challenge. In this thesis, the primary objective was to study the rotation of the polarization state from  $TE_0$  to  $TM_0$  and vice-versa in group III-V material (InP/InGaAsP). This is the most important material in the active photonic industry because of its superior electrical and thermal properties. Many advances in PICs have been achieved and the integration of the studied polarization rotator with devices such as SOAs and coherent modulators will be very useful. Unfortunately, the device in this thesis work could not be fabricated and tested at the test bench level but was simulated using the reliable simulation platform provided by

Ansys/Lumerical. Learning different Lumerical simulation software solvers to achieve this thesis work has added enormous experience for designing and simulating photonic devices such as the studied polarization rotator. Various solvers have been used here such as Eigenmode Expansion (EME), Finite Difference Eigenmode (FDE), and Finite Difference Time Domain (FDTD) according to simulation time and system memory requirements to obtain simulation results.

The study of the polarization rotator with the combination of various widths, lengths, different etch-stop materials, and core thickness, has been carried out. The polarization conversion efficiency for the various dimension of the device has resulted in the range of 45% to 98%. The final chosen device with the dimension definition was  $R_{substrate}=0.7\mu\text{m}$ ,  $R_d=0.26\mu\text{m}$ ,  $R_{etch}=0.03\mu\text{m}$ ,  $R_t=0.21\mu\text{m}$ ,  $R_{clad}=0.85\mu\text{m}$ ,  $deeper-etch=0.5\mu\text{m}$ ,  $w_1=0.85\mu\text{m}$ ,  $w_2=1.15\mu\text{m}$ ,  $L=200\mu\text{m}$  with the polarization conversion efficiency of 97%. The study of the oscillations observed at the output of the polarization rotator beyond the converter length  $L=200\mu\text{m}$  was carried out where the arbitrary length sweep for the converter section was performed and the converter length  $L$  was selected to be  $1700\mu\text{m}$ .

The maximum conversion efficiency was again cross-checked with the results obtained. The S-parameter approach was also used to relate the results obtained from the 3D-FDTD solver and the extracted outcome was verified. The selected polarization rotator was also simulated for the C-band wavelength (1530nm-1570nm) where the *PER* obtained was in the range of 11.7dB to 20dB respectively. Also, the polarization state of the source mode while propagating throughout the device is captured using the mode expansion monitors to understand the conversion from TE<sub>0</sub>/TM<sub>0</sub> to hybrid modes and then converted to TM<sub>0</sub>/TE<sub>0</sub>. Finally, the improvement of the fabrication tolerance was still limited in the previously published designs [51] [56]. The taper-etched waveguide structure in this work enhances the fabrication tolerance significantly. The study of the

width tolerance is explained in Table 5.3. If the width ( $w_1, w_2$ ) obtained after the fabrication is not precise the conversion efficiency of the device would still be acceptable, as the conversion of the polarization state will still take place but at a different position on the rotator length. This adds robustness to the design compared to the straight ridge waveguide. The polarization conversion efficiency values obtained are stated in Table 5.3. The broad range of width ( $0.75\mu\text{m} \sim 1.35\mu\text{m}$ ), single waveguide structure with foundry compatible dimensions, and the inserted etch-stop layer to control the thickness of the ridge waveguide make this design robust against the fabrication errors.

The integration of this device with other PIC elements using the InP platform could be possible due to the widely used similar material stack and ridge waveguide structure. This design has no bi-level slopes or taper as seen in the literature review which makes it comparably easy to fabricate. This one-waveguide design is compact and simple with a thick cladding layer that also opens the door for integration with another PIC element such as SOA, MZ, etc. The one-sided taper waveguide structure makes this device robust against any width variations during the fabrication process. The optical loss is difficult to calculate on the simulation platform as the surface roughness and the material losses are chosen to be null. Moreover, surface roughness is an important parameter to consider during the fabrication process. This affects the cut-off frequency values of the mode propagating inside the waveguide and the bandwidth. The mode in a waveguide propagates above a certain frequency called a cut-off frequency. The more the roughness of the waveguide surface, the less will be the bandwidth. For a single mode operation, it induces mode loss degrading the optical signal. This induces losses and affects the conversion efficiency of the device. Although, the accurate optical loss is projected to be measured on an optical test bench

using a polarization analyzer aligned at an output port of a possibly fabricated device (suggested future work).

The high-level fabrication block diagram is illustrated in Figure 6.1 and is useful to understand and select the process required to achieve maximum conversion efficiency. All these concepts discovered and demonstrated using the simulation techniques will benefit in working towards future efforts exploring the same or similar devices which will help in the advancement of optical communication platforms.

## 7.2 Future work

The primary goal for future work is to fabricate and test the polarization rotator under real conditions. The study of the polarization conversion efficiency will be premeditated over different work temperatures, repeatability over time, and can be verified against the simulation results. The coupling and transmission loss calculations would be ideal parameters to get measured using a tunable laser to input the light source at desired polarization state and wavelength. A polarization analyzer would be aligned at the output to extract the experimental data. The feedback from the results obtained through conducting the test under real conditions would help in the optimization of device geometry.

Finally, as the device structure is based on a single ridge waveguide, the research in terms of the active control of the polarization state on the same device will open new doors of innovation using PIN junction configuration.

## References

- [1] Internet World Stats, "Internet growth statistics," Miniwatts Marketing group, 03 July 2021. [Online]. Available: <https://www.internetworldstats.com/emarketing.htm>. [Accessed 01 December 2021].
- [2] Brian Lavallée, "The 2021 network seascape," Ciena Corporation, 14 January 2021. [Online]. Available: <https://www.ciena.com/insights/articles/the-2021-network-seascape.html>. [Accessed 30 January 2021].
- [3] E. Totolo and H. Baijal, "How a pandemic-induced boom in e-commerce can reshape financial services," World Bank Development, 22 December 2020. [Online]. Available: <https://blogs.worldbank.org/psd/how-pandemic-induced-boom-e-commerce-can-reshape-financial-services>. [Accessed 31 January 2021].
- [4] J. Clement, "Year-on-year change in online traffic worldwide as of May 2021," Statista, 15 June 2021. [Online]. Available: <https://www.statista.com/statistics/1105495/coronavirus-traffic-impact/>. [Accessed 30 June 2021].
- [5] B. Mukherjee, I. Tomkos, M. Tornatore, P. Winzer and Y. Zhao, Handbook of Optical Networks, Springer, 2020.
- [6] K. A. Ogudo, M. H. Mthethwa and D. M. Jean Nestor, "Comparative Analysis of Fibre Optic and Copper Cables for High-Speed Communication: South African Context," in *IEEE*, Winterton, South Africa, 2019.

- [7] E. Y. Wirawan, R. Jayadi and G. Ardhyogi, "Effectiveness of Microducts as Alternative to Deploying Optical Cables to Support Smart Infrastructure," in *IEEE*, Bandung, Indonesia, 2021.
- [8] H. Venghaus and G. Norbert, *Fibre Optic Communication*, Springer, 2017.
- [9] Chris Bayly, "Submarine networking," Ciena Corporation, 01 January 2020. [Online]. Available: <https://www.ciena.com/insights/submarine>. [Accessed 31 January 2020].
- [10] S. Lourdudoss, R. T. Chen and J. Chennupati, "Silicon Photonics," in *Semiconductors and Semimetals*, vol. 99, Science Direct, 2018, pp. 2-228.
- [11] S. Yurchuk, O. Rabinovinch and S. Didenko, *Optoelectronics - Advanced Device Structures*, InTech Open, 2017.
- [12] B. Jalali and S. Fathpour, "Silicon Photonics," *Journal of Lightwave Technology*, vol. 24, no. 12, pp. 4600-4613, 2006.
- [13] B. Jalali, V. Raghunathan, R. Shori, S. Fathpour, D. Dimitropoulos and O. Stafsudd, "Prospects for Silicon Mid-IR Raman Lasers," *Selected Topics in Quantum Electronics*, vol. 12, no. 6, pp. 1618-1627, 2006.
- [14] M. J. Heck, J. F. Bauters, D. L. Michael, J. K. Doylend, S. Jain, G. Kurczveil, S. Sudharsanan, Y. Tang and J. E. Bowers, "Hybrid Silicon Photonic Integrated Circuit Technology," *SELECTED TOPICS IN QUANTUM ELECTRONICS*, vol. 19, no. 4, 2013.
- [15] Y. Painchaud, F. Pelletier, C. Latrasse, J. F. Gagne, S. Savard, G. Robidoux, M. J. Picard, C. A. Davidson, M. Pelletier, m. Cyr, C. Paquet, M. Guy, M. M. Osman, M.

Chagnon and D. V. Plant, "Silicon-based products and solutions," *Integrated Optics: Devices, Materials, and Technologies*, vol. 18, 2014.

- [16] Infinera Corp, The Advantages of Indium Phosphide Photonic Integration in High-performance Coherent Optics, Ottawa: Infinera, 2009.
- [17] Infinera, Photonic Integrated Circuits, Ottawa: White House, 2015.
- [18] W. Ye, "Introduction to Silicon Photonics," Carleton University, Ottawa, 2020.
- [19] M. Cooke, "Silicon photonics and III-V integration," *Compounds and Advanced Silicon*, vol. 11, no. 7, pp. 80-84, 2016.
- [20] J. E. Bowers and A. Y. Liu, "A Comparison of Four Approaches to Photonic Integration," California, 2017.
- [21] K. Okamoto, Fundamentals of Optical Waveguides (Optics & Photonics Series), Tokyo: ACademic Press, 2010.
- [22] J. A. Stratton, Electromagnetic theory, New York: McGraw-Hill Book Company, Inc., , 1941.
- [23] K. Y. You, Emerging Waveguide Technology, Malaysia: InTech Open, 2018.
- [24] E. Collett, Field Guide to Polarization, Bellingham: SPIE Press, 2005.
- [25] Data Ray, "M<sup>2</sup> and High-order Modes," 27 April 2016. [Online]. Available: <https://dataray.com/blogs/dataray-blog/m-sup2-and-high-order-modes>. [Accessed 20 March 2022].
- [26] Agilent Technologies, "Polarization Dependent Loss Measurement of Passive Optical Components," Agilent Technologies, 2002.
- [27] E. Collett, Field Guide to Polarization, Bellingham: SPIE Press, 2005.

- [28] General Photonics, "Polarization in Fiber Optics," Newpoert Corporation, 2022.
- [29] Angewandte Chemie, "A Flexible Organic Single Crystal with Plastic-Twisting and Elastic- Bending Capabilities and Polarization-Rotation Function," *Organic Crystals*, vol. 12, no. 4, 2020.
- [30] Yesongyu Choi et al, "Broadband tunable polarization rotator based on the waveguiding effect of liquid crystals," *Applied Physics* , vol. 12, 2021.
- [31] Avner Safrani and I Abdulhalim, "Liquid-crystal polarization rotator and a tunable polarizer," *Optic Letters*, vol. 34, no. 12, 2009.
- [32] Ahmed El-Sayed Abd-Elkader, Mohamed Farhat O. Hameed, Nihal F. F. Areed, Hossam El-Din Mostafa, Salah S. A. Obayya, "Highly tunable compact polarization rotator based on silicon on insulator platform," *Optical and Quantum Electronics*, vol. 51, no. 149, 2019.
- [33] Qiang Xu, Li Chen, Michael G. Wood, Peng Sun & Ronald M. Reano, Electrically tunable optical polarization rotation on a silicon chip using Berry's phase, Ohio: Macmillian Publishers Limited, 2014.
- [34] Hiroshi Fukuda, Koji Yamada, Tai Tsuchizawa, Toshifumi Watanabe, Hiroyuki Shinohima, and Sei-ichi Itabashi, "Polarization rotator based on silicon wire waveguides," *Optic Express*, vol. 16, no. 4, pp. 2612-2635, 2008.
- [35] Zhechao Wang and Daoxin Dai, "Ultrasmall Si-nanowire-based polarization rotator," *Journal of the Optical Society of America B*, vol. 25, no. 5, pp. 747-753, 2008.

- [36] Wangqing Yuan, Keisuke Kojima, Bingnan Wang, Toshiaki Koike-Akino, Kieran Parsons, Satoshi Nishikawa, and Eiji Yagyu, "Mode-evolution-based polarization rotator- splitter design via simple fabrication process," *Optical Society of America*, 2012.
- [37] Daoxin Dai, Liu Liu, Shiming Gao, Dan-Xia Xu, and Sailing He, "Polarization management for silicon photonic integrated circuits," *Laser Photonics*, vol. 7, no. 3, pp. 303-328, 2013.
- [38] Anbang Xie, Linjie Zhou, Jianping Chen, and Xinwan Li, "Efficient silicon polarization rotator based on mode-hybridization in a double-stair waveguide," *Optical Society of America*, vol. 23, no. 4, 2015.
- [39] Velko P. Tzolov, Marie Fontaine, "A passive polarization converter free of longitudinally-periodic," *Optics Communications*, no. 127, pp. 7-13, 1996.
- [40] J. Z. Huang, R. Scarmozzino, G. Nagy, M. J. Steel, and R. M. Osgood, Jr., "Realization of a Compact and Single-Mode Optical Passive Polarization Converter," *Photonics Technology Letters*, vol. 12, no. 3, pp. 317-319, 2000.
- [41] B. M. A. Rahman, S. S. A. Obayya, N. Somasiri, M. Rajarajan, K. T. V. Grattan, and H. A. El-Mikathi, "Design and Characterization of Compact Single-Section Passive Polarization Rotator," *Lightwave Technology*, vol. 19, no. 4, pp. 512-519, 2001.
- [42] "Full vectorial finite element modeling of novel polarization rotators," *Optical and Quantum Electronics*, vol. 35, pp. 297-312, 2003.
- [43] N. Somasiri, B. M. A. Rahman and S. S. A. Obayya, "Fabrication Tolerance Study of a Compact Passive Polarization Rotator," *Lightwave Technology*, vol. 20, no. 4, pp. 751-757, 2002.

- [44] Hatem El-Refaei and David Yevick, "An Optimized InGaAsP/InP Polarization Converter Employing Asymmetric Rib Waveguides," *Lightwave Technology*, vol. 21, no. 6, pp. 1544-1548, 2003.
- [45] M Nikoufard and M Hatami, "Ultra-short novel transverse magnetic to transverse electric polarization rotator in hybrid integration of InGaAsP/silicon-on-insulator technologies," *International Journal of Physics*, vol. 90, no. 2, pp. 211-217, 2015.
- [46] Maria V Kotlyar, Lorenzo Bolla, Michele Midrio, Liam O'Faolain and Thomas F Krauss, "Compact polarization converter in InP-based material," *Optical Design and Fabrication*, vol. 13, no. 13, 2005.
- [47] L. M. Augustin, J. J. G. M. van der Tol, E. J. Geluk, and M. K. Smit, "Short Polarization Converter Optimized for Active–Passive Integration in InGaAsP–InP," *Photonics Technology Letters*, vol. 19, no. 20, pp. 1673-1675, 2007.
- [48] Zhechao Wang and Daoxin Dai, "Ultrasmall Si-nanowire-based polarization rotator," *Optical Society of America*, vol. 25, no. 5, pp. 747-753, 2008.
- [49] Hiroshi Fukuda, Koji Yamada, Tai Tsuchizawa, Toshifumi Watanabe, Hiroyuki Shinojima and Sei-ichi Itabashi, "Silicon photonic circuit with polarization diversity," *Optical Society of America*, vol. 16, no. 7, 2008.
- [50] C. Alonso-Ramos, S. Romero-García, A. Ortega-Moñux, I. Molina-Fernández, R. Zhang, H. G. Bach, and M. Schell, "Polarization rotator for InP rib waveguide," *Optics Letters*, vol. 37, no. 3, pp. 335-337, 2012.

- [51] Masaru Zaitsu, Takuo Tanemura, Akio Higo, and Yoshiaki Nakano, "Experimental demonstration of self-aligned InP/InGaAsP polarization converter for polarization multiplexed photonic integrated circuits," *Optics Express*, vol. 21, no. 6, 2013.
- [52] Yule Xiong, Dan-Xia Xu, Jens H. Schmid, Pavel Cheben, Siegfried Janz and Winnie N. Ye, "Fabrication tolerant and broadband polarization splitter and rotator based on a taper-etched directional coupler," *Optics Express*, vol. 22, no. 14, 2014.
- [53] Chyong-Hua Chen and Kuei Ho Chen, "Novel Polarization Rotators for Silicon Photonic Integrated Circuits," *Open Access*, no. 3, pp. 107-113, 2017.
- [54] Zheng-Yong Song, Qiong-Qiong Chu, Xiao-Peng Shen, Qing Huo Liu, "Wideband high-efficient linear polarization rotators," *Frontier Physics*, vol. 13, no. 5, 2017.
- [55] Zhi-Shan Hou, Xiao Xiong, Jia-Ji Cao, Qi-Dai Chen, Zhen-Nan Tian,Xi-Feng Ren, and Hong-Bo Sun, "On-Chip Polarization Rotators," *Advanced Optic Matter*, vol. 7, 2019.
- [56] Abdulaziz E. Elfigi, Ryoma Kobayashi, Ryota Tanomura, Takuo Tanemura, and Yoshiaki Nakano, "Fabrication-Tolerant Half-Ridge InP/InGaAsP Polarization Rotator With Etching-Stop Layer," *Photonics Technology Letters*, vol. 32, no. 11, pp. 663-666, 2020.
- [57] Gary S. May Ph.D. Costas J. Spanos Ph.D, Fundamentals of Semiconductor Manufacturing and Process Control, John Wiley & Sons, Inc., 2006.
- [58] D.G.Rabus, "Integrated Ring Resonators," in *III-V Materials*, New York, Springer, 2007, pp. 40-70.

- [59] Bulent Cakmak, "Fabrication and characterization of dry and wet etched InGaAs/InGaAsP/InP long wavelength semiconductor lasers," *Optics Express*, vol. 10, no. 13, 2002.
- [60] Michael Huff, "Recent Advances in Reactive Ion Etching and Applications of High-Aspect-Ratio Microfabrication," *Micro Machines*, vol. 12, no. 991, pp. 3-24, 2021.
- [61] Sergey Ishutkin, Vadim Arykov, Igor Yunusov, Mikhail Stepanenko, Vyacheslav Smirnov, Pavel Troyan and Yury Zhidik , "The Method of Low-Temperature ICP Etching of InP/InGaAsP Heterostructures in Cl<sub>2</sub>-Based Plasma for Integrated Optics Applications," *Micro Machines*, vol. 12, no. 1535, 2021.
- [62] Abdulaziz E. Elfiqi, Ryota Tanomura , Dawei Yu, Warakorn Yanwachirakul , Haifeng Shao, Yuto Suzuki, Takuo Tanemura, and Yoshiaki Nakano, "Robust InP/InGaAsP Polarization Rotator Based on Mode Evolution," *Photonics Technology Letters*, vol. 34, no. 2, pp. 109-112, 2022.
- [63] M. Polyanskiy, "Refractive Index," Refractive Index, 2008. [Online]. Available: <https://refractiveindex.info>. [Accessed 2022].
- [64] n. k. Dutta, Semiconductor Optical Amplifiers, Singapore: World Scientific, 2012.
- [65] J. O'CALLAGHAN, R. LOI, E. E. MURA, B. ROYCROFT, A. J. TRINDADE, K. THOMAS, A. GOCALINSKA, E. PELUCCHI, J. ZHANG, G. ROELKENS, C. A. BOWER, AND B. CORBETT, "Comparison of InGaAs and InAlAs sacrificial layers for release of InP-based devices," *Optics material Express*, vol. 7, no. 12, 2017.

- [66] S. Dupont, A. Beaurain, P. Miska, M. Zegaoui, J.-P. Vilcot, H. Li, M. Constant, D. Decoster and J. Chazelas, "Low-loss InGaAsP/InP submicron optical waveguides fabricated by ICP etching," *ELECTRONICS LETTERS*, vol. 40, no. 14, 2004.
- [67] M. Zaitsu, T. Tanemura, A. Higo and Y. Nakano, "Experimental demonstration of self-aligned InP/InGaAsP polarization converter for polarization multiplexed photonic integrated circuits," *Optics Express*, vol. 21, no. 6, 2013.
- [68] W. d. Carvalho Jr, S. A. Bernussi, M. T. Furtado, A. L. Gobi and M. A. Cotta, "Strained In<sub>1-x</sub>GaxAsyP<sub>1-y</sub>/InP Quantum Well Heterostructures Grown by Low-Pressure Metalorganic Vapor Phase Epitaxy," *Material Research*, vol. 2, no. 2, pp. 49-54, 1999.
- [69] M. S. Leite, R. L. Woo, W. D. Hong, D. C. Law and H. A. Atwater, "InAlAs EPITAXIAL GROWTH FOR WIDE BAND GAP SOLAR CELLS," *IEEE*, vol. 6, no. 11, pp. 000780-000783, 2011.
- [70] Long Chen, Christopher R. Doerr, and Young-Kai Chen , "Compact polarization rotator on silicon for polarization-diversified circuits," *Optics Letters*, vol. 36, no. 4, pp. 469-471, 2011.
- [71] Diedrik Vermeulen, Shankar Selvaraja, Peter Verheyen, Philippe Absil, Wim Bogaerts, Dries Van Thourhout, and Gunther Roelkens, "Silicon-on-Insulator Polarization Rotator Based on a Symmetry Breaking Silicon Overlay," *IEEE Photonics Technology Letters* , vol. 24, no. 6, pp. 482-484, 2012.
- [72] Huijuan Zhang, Suchandrima Das, Ying Huang, Chao Li, Shiyi Chen, Haifeng Zhou, Mingbin Yu, Patrick Guo-Qiang Lo, and John T. L. Thong, "Efficient and broadband

- polarization rotator using horizontal slot waveguide for silicon photonics," *Applied Physics Letters*, vol. 34, no. 13, pp. 3181-3187, 2012.
- [73] Yule Xiong, Dan-Xia Xu, Jens H. Schmid, Pavel Cheben, Siegfried Janz and Winnie N. Ye, "Robust Silicon Waveguide Polarization Rotator With an Amorphous Silicon Overlayer," *IEEE Photonics Journal*, vol. 6, no. 2, 2014.
- [74] Hatem El-Refaei, David Yevick, and Trevor Jones, "Slanted-Rib Waveguide InGaAsP-InP Polarization Converters," *Lightwave Technology*, vol. 22, no. 5, pp. 1352-1357, 2004.
- [75] M. ZAITSU, T. TANEMURA and Y. NAKANO, "Numerical Study on Fabrication Tolerance of Half-Ridge InP Polarization Converters," *IEICE TRANS. ELECTRON*, vol. VOL.E97-C, no. NO.7, 2014.

Notes: